Karlsruhe Institute of Technology

Magnetic Characterization Studies of a Superconducting Transverse Gradient Undulator for a Compact LWFA-based Free-Electron Laser

Doctoral Thesis of

M. Sc. Kantaphon Damminsek

at the Department of Physics
Laboratory for Applications of Synchrotron Radiation (LAS)

Reviewer:	Prof. Dr. Anke-Susanne Müller
Second reviewer:	Prof. Dr. Bernhard Holzapfel
Advisor:	Dr. Axel Bernhard
Second advisor:	Dr. Hyuk Jin Cha

February 1, 2018 – October 31, 2022

Karlsruher Institut für Technologie
Laboratorium für Applikationen der Synchrotronstrahlung (LAS)
Kaiserstrasse 12
D-76131 Karlsruhe

Karlsruhe Institute of Technology

Untersuchungen zur magnetischen Charakterisierung eines supraleitenden Transversalgradient-Undulators für einen kompakten, Laser-Wakefield-Beschleuniger-getriebenen Freie-Elektronen-Laser

zur Erlangung des akademischen Grades eines

DOKTORS DER NATURWISSENSCHAFTEN (Dr. rer. nat.)

von der KIT-Fakultät für Physik des
Karlsruher Instituts für Technologie (KIT)

angenommene

DISSERTATION

von

M. Sc. Kantaphon Damminsek

Tag der mündlichen Prüfung:	28.10.2022
Referent:	Prof. Dr. Anke-Susanne Müller
Korreferent:	Prof. Dr. Bernhard Holzapfel
Betreuer:	Dr. Axel Bernhard
Zweiter Betreuer:	Dr. Hyuk Jin Cha

Karlsruher Institut für Technologie
Laboratorium für Applikationen der Synchrotronstrahlung (LAS)
Kaiserstrasse 12
D-76131 Karlsruhe

I declare that I have developed and written the enclosed thesis completely by myself, and have not used sources or means without declaration in the text.

PLACE, DATE

. . . . . .

(M. Sc. Kantaphon Damminsek)

Abstract

A conventional planar undulator which has a uniform and periodic magnetic field in the undulator gap requires low energy-spread electron beams for radiation with coherent characteristics. In general, such electron beams are achieved in large-scale facilities such as linear accelerators and storage rings.

A laser-plasma electron accelerator based on the laser wakefield acceleration (LWFA) mechanism can produce electron beams with an energy of several hundred MeV in a very short acceleration medium of a few millimeters to centimeters in length. However, the electron beam properties are much worse than those of conventional electron accelerators due to the plasma instability in the medium. Especially, the increased energy spread, beam divergence and pointing instability lead to incoherent radiation in the planar undulator.

The transverse gradient undulator (TGU) having nonuniform magnetic fields in the transverse plane perpendicular to the beam axis is an alternative to overcome the disadvantage of the LWFA electron beams with the high energy spread. A TGU based on modern superconducting technologies for extremely strong magnetic fields was developed at Karlsruhe Institute of Technology (KIT) to experimentally prove that the TGU scheme is a viable option for the free-electron laser (FEL) amplification with LWFA-generated electron bunches.

This thesis describes the magnetic characterization of the superconducting TGU designed for a compact FEL driven by a laser-plasma accelerator. Magnetic powering tests and quench studies with the TGU in a vacuum cryostat were performed at a temperature of 4.3 K to 4.4 K. The TGU coils were successfully powered up to 850 A and reached the superconducting state. The perpendicular components of the magnetic field in the median plane of the TGU were mapped using a Hall probe system with seven equidistant sensors parallel to the median plane at temperatures of 5 K to 6 K and therefore at applied currents limited to 10 A to 50 A. Nevertheless, the magnetic fields in nominal operation conditions (750 A) could be estimated due to their linear dependence on the applied current.

Moreover, the measured magnetic field maps were used to evaluate the expected radiation properties by simulations with the code WAVE [1]. The narrow bandwidth of the undulator radiation was confirmed and the spectral dispersion of the electron beam required to match the transverse field gradient of the TGU was determined. The results of the WAVE simulations and the effect of field errors observed in the measurements on the radiation will be discussed in this thesis.

Zusammenfassung

Die Erzeugung kohärenter Strahlung in einem herkömmlichen planaren Undulator mit einem transversal homogenen und longitudinal periodischen Magnetfeld erfordert Elektronenstrahlen mit geringer Energieverteilungsbreite. Im Allgemeinen werden solche Elektronenstrahlen in Großanlagen wie Linearbeschleunigern und Speicherringen generiert.

Ein Laser-Plasma-Elektronenbeschleuniger, der auf dem Mechanismus der Laser-Wakefield-Beschleunigung (LWFA) basiert, kann Elektronenstrahlen auf eine Energie von mehreren hundert MeV in einem sehr kurzen Beschleunigungsmedium von einigen Millimetern bis Zentimetern Länge beschleunigen. Allerdings sind die Elektronenstrahleigenschaften aufgrund der Plasmainstabilität im Medium deutlich schlechter als bei konventionellen Elektronenbeschleunigern. Insbesondere die erhöhte Energieeverteilungsbreite, Strahldivergenz und Richtungsinstabilität führen zu inkohärenter Strahlung in einem planaren Undulator.

Der Transversalgradient-Undulator (TGU) mit transversal abnehmender Magnetfeldamplitude ist eine Alternative, um den Nachteil der LWFA-Elektronenstrahlen mit der großen Energieverteilungsbreite zu überwinden. Ein TGU, der auf modernen supraleitenden Technologien für extrem starke Magnetfelder basiert, wurde am am Karlsruher Institut für Technologie (KIT) entwickelt, um experimentell zu zeigen, dass das TGU-Schema ein gangbarer Weg ist, mit LWFA-erzeugten Elektronenpaketen auch Freie-Elektronen-Laser (FEL) -Verstärkung zu erreichen.

Die vorliegende Arbeit beschreibt die magnetische Charakterisierung des supraleitenden TGU, dessen Design für einen kompakten LWFA-getriebenen FEL entwickelt wurde. Magnetische Leistungstests und Quenchstudien mit dem TGU wurden bei einer Temperatur von 4.3 K bis 4.4 K in dessen eigenem Kryostaten durchgeführt. Die TGU-Spulen erreichten den supraleitenden Zustand und wurden erfolgreich mit bis zu 850 A betrieben. Die senkrechte Komponente des Magnetfelds in der Mittelebene des TGU wurden mit einem System sieben äquidistanter Hall-Sensoren bei Temperaturen von 5 K bis 6 K und daher bei relativ kleinen Stromstärken von 10 A bis 50 A erfasst. Die Magnetfelder unter nominalen Betriebsbedingungen (750 A) konnten jedoch aufgrund ihrer proportionalen Abhängigkeit vom Strom ermittelt werden.

Darüber hinaus wurden die gemessenen Magnetfeldkarten verwendet, um die erwarteten Strahlungseigenschaften durch Simulationen mit dem Code WAVE [1] zu bewerten. Die schmale Bandbreite der Undulatorstrahlung wurde bestätigt und die spektrale Dispersion des Elektronenstrahls, die zur Anpassung an den transversalen Feldgradienten des TGU erforderlich ist, wurde bestimmt. Die Ergebnisse der WAVE-Simulationen und die Auswirkungen der bei den Messungen beobachteten Feldfehler auf die Strahlung werden in dieser Arbeit diskutiert.

Acknowledgements

The researches in this doctoral thesis have been carried out under supervisions of Dr. Axel Bernhard, Dr. Hyuk Jin Cha and Prof. Dr. Anke-Susanne Müller at the Laboratory for Applications of Synchrotron Radiation (LAS), Institute for Beam Physics and Technology (IBPT), Karlsruhe Institute of Technology (KIT), Karlsruhe, Germany. The financial supports for living and studying in Germany were provided by the Development and Promotion of Science and Technology Talents Project (DPST), the Royal Thai Government Scholarship and Karlsruhe Institute of Technology.

I would like to acknowledge the supports from many people and organizations. These studies could never be accomplished without introductions and encouragements from various ways. I would like to employ this opportunity to thank those people and organizations who have performed all objectives possible and complete.

First, I would like to express my gratitude to Dr. Axel Bernhard, the supervisor and group leader of the superconducting transverse gradient undulator (TGU) project who always introduces and supports everything in my doctoral study. I would like to thank Dr. Hyuk Jin Cha for supporting the experiments and thesis writing. I would like to thank Prof. Dr. Anke-Susanne Müller for supervising the overall of my doctoral study and being the first reviewer of my thesis. I would like to thank Prof. Dr. Bernhard Holzapfel for being the second reviewer of my thesis.

Second, I would like to thank Mr. Steffen Schott, Miss Nicole Glamann, Mr. Stefan Uhlemann, Mr. Daniel Ritz, Mr. Ralf Lang, Dr. Andreas Will, Miss Maisui Ning and Miss Falastine Abusaif for supporting the experimental preparations. Third, I would like to Dr. Andreas Grau, Dr. Julian Gethmann, Mr. Yimin Tong and Mr. Sebastian Richter for supporting the TGU experiments. I also would like to thank Mrs. Claudia Lieber who always supports the administration works regarding to the TGU project. I experienced a lot due to performing the experiments and living in Karlsruhe.

I would like to express my gratitude to the DPST scholarship for all financial support since the bachelor study, starting in the academic year 2009, at Chiang Mai University. The DPST scholarship and Kyoto University provided me the supports to achieve the master research program at Kyoto University, which was the great contribution to my experimental skills and knowledge toward to my doctoral study at Karlsruhe Institute of Technology. The great opportunities in my education life could never be achieved without the supports from the DPST scholarship and all Thai taxpayers.

Kantaphon Damminsek
Karlsruhe Institute of Technology
December 1, 2022

Contents

Abstract i

Zusammenfassung iii

Acknowledgements v

1. Introduction 1

2. Physical Background 5
2.1. Undulator Radiation . . . 5
2.1.1. Radiation Field of Relativistic Charged Particles . . . 5
2.1.2. Magnetic Field of Planar Undulator . . . 7
2.1.3. Electron Motion in the Planar Undulator . . . 9
2.1.4. Radiation of the Planar Undulator . . . 10
2.2. Free Electron Laser . . . 16
2.2.1. One-Dimensional Theory of the High-Gain FEL . . . 17
2.3. Transverse Gradient Undulator . . . 21
2.3.1. Basic Principle of Radiation and FEL Amplification in a TGU . . . 22
2.3.2. The Superconducting TGU demonstrator built at KIT . . . 23
2.3.3. Cryostat Configuration . . . 23

3. Operation and Characterization of Superconducting TGU 27
3.1. TGU Installation . . . 27
3.2. LTS Wiring of the Magnet in the Cryostat . . . 32
3.2.1. SC Wire Support Structures . . . 32
3.2.2. Conduct-cooled Cylinder . . . 34
3.2.3. SC Wire Soldering Method . . . 35
3.3. TGU Cool-down Procedure . . . 37
3.4. TGU powering tests . . . 45
3.4.1. Current supply and quench protection equipment . . . 45
3.4.2. Eddy current heating . . . 48
3.4.3. Powering tests using a single TGU coil . . . 50
3.4.4. Powering tests using two TGU coils in series . . . 52

4. Magnetic Field Measurements of the TGU 59
4.1. Methodology . . . 59
4.1.1. Hall Effect . . . 59
4.1.2. Calibration of the Hall Probe . . . 60
4.1.3. Error Analysis of the Magnetic Field Measurement . . . 61

4.2. Experimental Setup 63
4.2.1. Magnetic Field Measurement System 63
4.2.2. Misalignment of Hall probe array 65
4.2.3. Refurbishment of the Magnetic Field Measurement System 68
4.3. Magnetic Field Measurement of the TGU Coil 71
4.3.1. Heat Load Introduced by the Measurement System 71
4.3.2. Measured Field of the TGU and Time Constant 72
4.3.3. Transverse Magnetic Flux Density of the TGU 73
4.4. Magnetic Field Measurements of the Correction Coils 77
4.4.1. Measured Fields and Time Constants of the Correction Coils . . . 77
4.4.2. Transverse Magnetic Flux Densities of the Correction Coils . . . 78

5. Evaluation of the TGU radiation **81**
5.1. Construction of the 3-D Magnetic Field maps for Evaluation 81
5.2. Electron Trajectory in the Magnetic Field 84
5.3. Evaluation of the Radiation Properties 86

6. Conclusions **91**

Bibliography **93**

A. Appendix **99**
A.1. Evaluation of the TGU radiation 99

List of Figures

1.1. Comparison of the peak brightness of the radiations from selected free-electron laser (FEL) and synchrotron facilities [2]. 1
1.2. Schematic layout of a superconducting TGU-based radiation source [12]. 2

2.1. Diagram explaining the planar undulator scheme. 7
2.2. Diagram illustrates a traveling path of electrons inside the undulator magnet and the emission of the undulator radiation. Magnetic fields point in x-axis and a sinusoidal trajectory of the electron is on yz-plane. 11
2.3. FEL amplification with (a) an optical resonator and (b) SASE mechanism. 16
2.4. Diagrams showing (a) a planar undulator and (b) a cylindrical TGU. . . . 21
2.5. A photograph of the SC TGU with its support structures [12]. 24
2.6. Sectional view of the cryostat assembly in different temperature regions. The TGU is placed in vacuum and conduction-cooled condition [33]. . . 25
2.7. Photographs of (a) multi-stage roots pump, (b) turbopump, (c) full-range pressure gauge and (d) controlling device of the turbopump and pressure monitor. 26

3.1. (a) The TGU and heat exchanger plates placed on the main support structure of the cryostat, (b) a front and (c) a side view photographs explaining the additional indium sheets and the inserted polyimide sheets. 28
3.2. Diagram explaining the 4-terminal sensing method for measuring the voltage of the temperature sensors. 29
3.3. Voltage of the DT-670 series silicon diode sensor as a function of its temperature at a constant current [35]. 30
3.4. Absolute value of the sensitivity of the DT-670 series silicon diode sensor as a function of temperature [35]. 30
3.5. Dependency of resistance of the PT-100 sensor on temperature below 300 K [36]. 31
3.6. Sensitivity of the PT-100 sensor dependent on its temperature [36]. . . . 32
3.7. A diagram explaining the guided SC wires and their own support structure [39]. 33
3.8. A photograph of the cryostat current feedthroughs and their SC wires which will be connected to those coming out from the TGU. 33
3.9. Photograph showing the SC wires guided along their support structures to the connecting point. 34
3.10. Schematic diagrams of the SC wiring between terminals of the TGU and HTS leads when both coils were connected in (a) a parallel- and (b) series-circuits. 35

3.11. (a) Conduct-cooled cylinder and (b) small indium sheets attached to the contact surface to increase the capability of the heat transfer. 35
3.12. (a) Original and (b) improved soldering methods for connecting the LTS wires. 36
3.13. Temperatures of the TGU and a bottom of LHe reservoir, which is a cold reservoir, during cool-down procedure using the liquid nitrogen. 41
3.14. Temperatures of the TGU and a bottom of LHe reservoir, which is a cold reservoir, during cool-down procedure using the liquid helium. 42
3.15. Temperatures of the TGU, the bottom of LHe reservoir and conduct-cooled plates at a final step of the cool-down procedure using the LHe. 43
3.16. TGU temperature during the entire cool-down procedure. 44
3.17. Schematic diagrams show positions of the voltage taps (Q1 to Q4) for quench detection in powering tests of (a) a single coil and (b) two coils. . 46
3.18. Voltage drop across a complete LTS parts of a single TGU coil as a function of the current ramp rate. 47
3.19. Photograph of 2-period TGU explaining the SC coils, two cylindrical coil former and rectangular support structures [12]. 48
3.20. Diagram explaining electrical connections of the TGU coils when each coil is powered separately [39]. 50
3.21. Thermal behaviour of the TGU during powering test of a single coil using a current ramp rate of 0.5 A s^{-1} when the applied current was normally increased [39]. 51
3.22. Thermal behaviour of the TGU during powering test of a single coil using a current ramp rate of 2.0 A s^{-1} when the applied current was immediately suspended [39]. 52
3.23. Diagram explaining the electrical connections of the TGU coils when both coils are connected in series and powered together. 53
3.24. Powering test of two TGU coils using a current ramp rate of 0.5 A s^{-1} when (a) the current was normally increased and (b) quench after the same ramp. 54
3.25. Thermal behaviour of the two TGU coils while the applied current increases in several steps using a current ramp rate of 1.0 A s^{-1}. 55
3.26. The TGU temperature during a single-step ramping to operating current of 750 A using a ramp rate of 0.2 A s^{-1}. 56
3.27. Powering test of two TGU coils (a) reaching 850 A using a current ramp rate 0.2 A s^{-1} and (b) when the quench immediately occurs. 57
3.28. Quench dependency on the current ramp rate of the applied current of the TGU. 58
3.29. Quench numbers with respect to the applied current of the TGU. 58

4.1. Diagram explaining the working principle of the Hall probe which consists of a thin semiconductor plate with length l, width w and thickness t [12]. 60
4.2. Diagram of the magnetic field measurement system with the TGU [50]. . 63
4.3. 2-D cross-sectional view in the transverse plane showing a position of the slide with 7-Hall probe array [50]. 63
4.4. Dimensions of the 7-Hall probe array (M7-TH5) in a unit of mm [12, 51]. 64

4.5. Diagram of the linear translation unit coupled with the TGU cryostat. . . 64
4.6. Angles of the central vertical axis of the Hall probe array with respect to the xy-plane in the TGU coordinate system. 65
4.7. Angles of the central vertical axis of the Hall probe array with respect to the xz-plane in the TGU coordinate system. 65
4.8. Angles of the central vertical axis of the Hall probe array with respect to the yz-plane in the TGU coordinate system. 66
4.9. Photograph of the sliding system with the Hall probe dummy attached to the slide. 67
4.10. Photograph of the 7-Hall probe array attached to the MACOR® ceramic piece for electrical isolation from the TGU and the measurement system. 68
4.11. Photographs of (a) a circuit board and (b) Hall probe cables and a movable multi-channel cable connected to the circuit board. 68
4.12. Photograph of the completed sliding system with the Hall probe array attached to the TGU. 69
4.13. Photograph of the PEEK groove used to limit a movement degree of freedom of the movable multi-channel cable. 69
4.14. Photograph of the PEEK coupling used for the sliding systems. 70
4.15. Photograph of the linear translation unit attached to the cryostat recipient shield. 70
4.16. Mean values of the offset voltage of each Hall probe during the measurements over consecutive days. 72
4.17. Offset-corrected measured voltages of the seven Hall probes as a function of time at a TGU current of 40 A 73
4.18. Magnetic flux density amplitudes, including the error bars, measured by seven Hall probes as a function of time at the TGU current of 40 A. . . . 73
4.19. Magnetic distribution along parallel longitudinal axes at the transverse direction of Hall probe 1, 4 and 7 at a TGU operating current of 30 A. . . 74
4.20. Magnetic flux density as a function of the TGU coil current for the probe numbers of 1, 4, and 7. 75
4.21. Perpendicular magnetic fields measured from 7-Hall probe array and the fields calculated from the ideal position of the Hall probes dependent on a distance from the TGU center at a TGU operating current of 30 A. 76
4.22. (a) Photograph of correction coils inserted into the TGU coil former and (b) diagram explaining the wiring of the correction coil in a parallel circuit. 77
4.23. Offset-corrected measured voltages of the seven Hall probes as a function of time at a correction coil current of 5 A. 77
4.24. Magnetic flux densities measured by the seven Hall probes as a function of time at a correction coil current of 5 A. 78
4.25. Magnetic flux densities along longitudinal axes at the transverse positions of seven Hall probes at a correcting coil current of 5 A. 79
4.26. Magnetic flux density as a function of the correction coil current. 79
4.27. Magnetic flux density as a function of the transverse position at correction coil current of 5 A. 80

5.1. Construction of the 2-D field map in the dispersion plane of the TGU, $y = 0$. 82
5.2. Construction of the 3-D field distribution for the dispersion region of the TGU. 82
5.3. Average offset magnetic field of each hall probe dependence of distance in x-axis. 84
5.4. Trajectories of the electron with an energy of 112 MeV (a) traveling through the entire magnetic field and (b) initiated at $z = 9.775$ mm traveling through the rest part of magnetic field. 85
5.5. Photon flux density vs. photon energy at the field amplitude of 0.903 T. . 88
5.6. Photon flux density vs. photon energy of 8.26 eV. 89
5.7. Electron energy corresponding to the photon energy of 8.26 eV as a function of transverse position. 90

A.1. Photon flux density vs. photon energy at the field amplitude of 0.497 T. . 99
A.2. Photon flux density vs. photon energy at the field amplitude of 0.596 T. . 99
A.3. Photon flux density vs. photon energy at the field amplitude of 0.708 T. . 100
A.4. Photon flux density vs. photon energy at the field amplitude of 0.823 T. . 100
A.5. Photon flux density vs. photon energy at the field amplitude of 1.085 T. . 101
A.6. Photon flux density vs. photon energy at the field amplitude of 1.218 T. . 101

List of Tables

2.1. Specifications of the Nb-Ti SC wire used for the TGU. 23
2.2. Design parameters of the SC TGU developed at KIT. 24
2.3. Specifications of the cryostat for the TGU. 26

3.1. Specifications of the diode-based temperature sensors used in the TGU experiments [35]. 29
3.2. Specifications of the PT-100 sensors used in the TGU experiments [36]. . 31
3.3. Properties of LN_2 and LHe [40, 41] at atmospheric pressure. 37
3.4. Specifications of the current supply used for the TGU powering tests and operations. 45
3.5. Parameters used for the simplistic estimation of heat generated by the eddy current from the short SC coil. 49

4.1. Sensitivity of the Hall probe array (M7-TH5) at 77 K with the nominal control current of 10 mA and estimated errors. 61
4.2. Thermal conductivities of brass at several temperatures [56]. 71
4.3. Perpendicular magnetic fields of maximum flux densities averaged over the 32 measured periods and the ideal fields at a TGU operating current of 30 A. 75

5.1. Average offset magnetic field of each hall probe. 83
5.2. Comparison between the initial and final x-positions of the electron trajectories when electrons were initiated at $z = 0$ mm in all cases. 86
5.3. Parameters used in the WAVE simulations. 87
5.4. Details of the pinhole for evaluating the photon flux densities 88
5.5. Comparison of electron energies for the photon energy of 8.26 eV in the undulator equation and the WAVE simulation and the relative spectral width. 90

1. Introduction

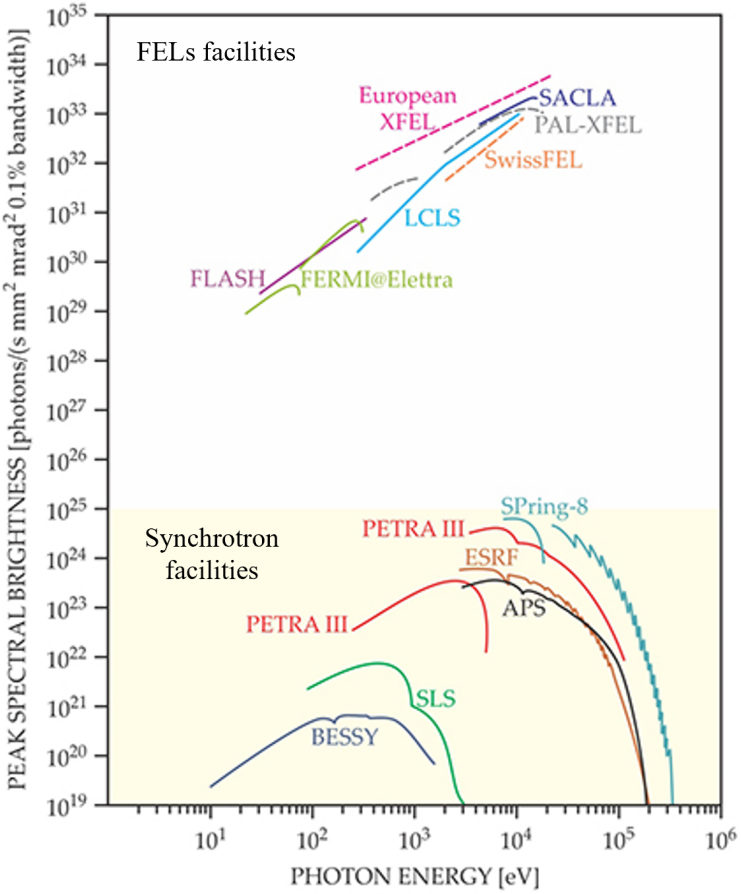


Figure 1.1.: Comparison of the peak brightness of the radiations from selected free-electron laser (FEL) and synchrotron facilities [2].

Acquiring extremely powerful ultraviolet (UV) and X-ray sources in a laboratory scale would increase the ability to discover novel scientific knowledge in such fields as physics, materials science, chemistry and biology. Synchrotron light facilities and free-electron lasers (FELs) are the most powerful radiation sources based on particle accelerators, especially for the UV and X-ray radiation [3]. In general, the synchrotron light sources and FEL facilities are based on large-scale electron accelerators with radiofrequency (RF) technologies, for which reason a few of those facilities exist worldwide [4].

Synchrotron radiation sources have been developed and optimized over many years. One of the most important development was the introduction of undulators, which are also the key component of FEL.

An undulator consists of a periodic array of alternating bending magnets. It was developed for radiation with more coherence and higher brightness than that from bending magnets. An electron travels through a conventional planar undulator with N_u periods and generates a wave train with N_u oscillation. As a result, the undulator radiation has coherent characteristics (intensity, $I \propto N_u^2$) with a narrow energy spectrum.

In case of an FEL, due to the so-called microbunching effect, all electrons in a single bunch radiate coherently. Thus, the intensity of the radiation grows quadratically with the number of electrons N_e per bunch ($I \propto N_e^2$). The brightness of the FEL can therefore be a million times higher than that from the synchrotron facilities. Figure 1.1 shows a comparison between the peak brightnesses achieved at selected FEL and synchrotron facilities.

The accelerating gradients in normal conducting RF cavities are limited to an order of 10^2 MV/m due to the electrical breakdown [5]. In cases of the superconducting cavities, the accelerating gradients can be achieved up to around 50 MV/m, which are restricted by quench and field emission [6, 7]. As an example from the limitations, the total length of the accelerating sections for an X-ray FEL facility reaches a kilometer scale [8].

In contrast, it was reported that the laser wakefield acceleration (LWFA) could produce the accelerating gradients of 10-100 GV/m using TW-laser pulses focused into a very short plasma medium [9, 10]. Therefore, it is obvious that the LWFA mechanism could make it possible to replace the existing large-scale accelerators with compactness and cost efficiency [11].

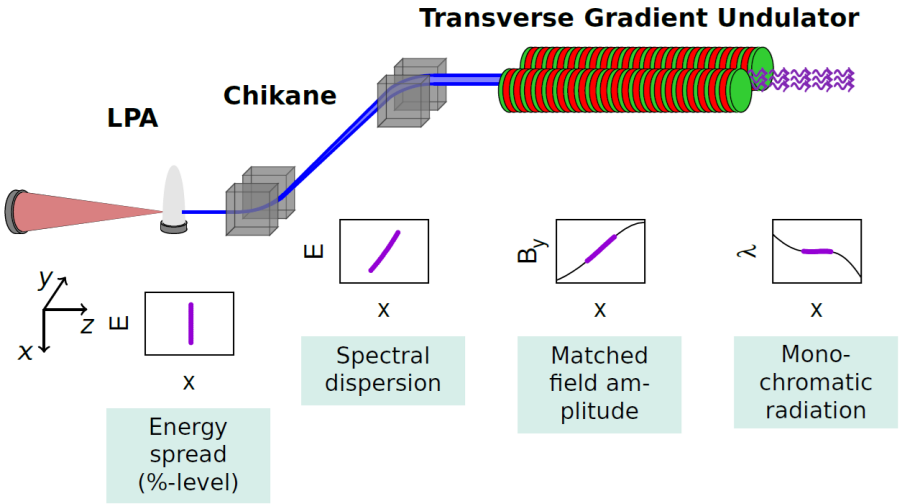


Figure 1.2.: Schematic layout of a superconducting TGU-based radiation source [12].

However, the electron beams generated by the LWFA have worse beam characteristics due to unstable conditions in plasma. The LWFA electrons experience nonuniform and unprecedentedly strong electric fields in the unstable plasma medium [13]. Thus, their beam quality is much worse than that from conventional electron accelerators, especially in terms of the energy spread and beam divergence. It was reported that in case of 1-GeV electron beam by 40 TW laser pulses, the energy spread was 2.5 % rms and the beam

divergence was 1.6 mrad rms obtained at the Berkeley Lab Laser Accelerator (BELLA) Center [10]. If the LWFA electrons are accelerated in a planar undulator, it would result in the unwanted incoherent radiation. For this reason, the more efficient undulators optimized for the LWFA electron beams are required for the radiation source. With a transverse gradient undulator (TGU), it is possible to compensate for the large energy spread from the LWFA beams for coherent radiation [14].

Figure 1.2 shows a concept of a radiation source with the LWFA electron beams accelerated in a TGU. A 40-period superconducting TGU has been developed at Karlsruhe Institute of Technology (KIT) [12]. The cylindrical pole shape was chosen for transverse field gradients higher than those in the tilted rectangular one.

The motivation of this thesis is to test the superconducting TGU and to experimentally prove that the TGU scheme is a viable option for the FEL amplification with compensation for a relatively larger energy spread from the LWFA electron beams. With a view to this goal, the thesis will describe the first transverse magnetic flux density measurement along the longitudinal axes of the TGU in its own cryostat and the estimation of the radiation properties from the measured magnetic fields.

The second chapter of this thesis describes a physical background about the undulator radiation toward FEL and the TGU. The third chapter is related to characterization of the TGU such as cool-down procedure and magnetic powering tests. The fourth chapter explains the magnetic field measurement. The last chapter is evaluations of TGU radiation.

2. Physical Background

2.1. Undulator Radiation

2.1.1. Radiation Field of Relativistic Charged Particles

The accelerated charges emit an electromagnetic radiation. In case of relativistic charged particles, this radiation is called synchrotron radiation, which exhibits particular properties as high brightness, a broad energy spectrum and a high degree of collimation.

The radiation field is a field transporting energy from the source to space. The radiation field travels with the finite speed of light. The properties of the radiation field depend on the point on the trajectory of the radiating charge some time earlier, at the retarded time, when the radiation was emitted. The retarded time, which is given by

$$t_r = t - \frac{1}{c} R(t_r). \tag{2.1}$$

To correlate the properties of the radiation field at the observation point with the trajectory of the radiating charges, the consideration starts at the Lorenz transformation and Maxwell's equations for moving charged particles in vacuum where $\epsilon_r = \mu_r = 1$.

At a bunch of co-moving charges represented by a charge density distribution ρ, the electric and magnetic potential are inserted into the homogeneous Maxwell equations. The results are wave equations for the magnetic vector potential and the scalar electric potential described by [15]

$$\begin{aligned} \nabla^2 \vec{A} - \frac{1}{c^2} \frac{\partial^2 \vec{A}}{\partial t^2} &= \frac{1}{\epsilon_0} \rho \vec{\beta} \\ \nabla^2 \varphi - \frac{1}{c^2} \frac{\partial^2 \varphi}{\partial t^2} &= \frac{1}{\epsilon_0} \rho, \end{aligned} \tag{2.2}$$

where ϵ_0 is the permittivity of free space, and $\vec{\beta} = \vec{v}/c$. Solutions of these wave equations can be obtained by

$$\begin{aligned} \vec{A}(t) &= \frac{\mu_0}{4\pi} \int \left. \frac{\vec{v}\rho(x,y,z)}{R} \right|_{t_r} dxdydz \\ \varphi(t) &= \frac{1}{4\pi\epsilon_0} \int \left. \frac{\rho(x,y,z)}{R} \right|_{t_r} dxdydz. \end{aligned} \tag{2.3}$$

In Equation 2.3, the quantities under the integral must be evaluated at the retarded time t_r due to the finite velocity of light. μ_0 is the permeability of free space, R is a distance between the observation point $P(x, y, z)$ and the position of the charge element $\rho(x_r, y_r, z_r)dx_r dy_r dz_r$. The vector of distance is

$$\vec{R} = (x_r - x, y_r - y, z_r - z). \tag{2.4}$$

The radiation observed at point P and at time t is the summation of all radiation fields simultaneously arriving at point P. The elements of that radiation field were possibly emitted by different charge elements at different times and positions.

In case of a single electric charge traveling with velocity $\vec{v}$, the assumption that the electrical charge is a point can be applied to achieve the retarded potential of a moving point charge q at time t and observation point P by

$$\begin{aligned} \vec{A}(P,t) &= \left.\frac{q\vec{\beta}}{4\pi c\epsilon_0 R\left(1+\vec{n}\cdot\vec{\beta}\right)}\right|_{t_r} \\ \varphi(P,t) &= \left.\frac{q}{4\pi\epsilon_0 R\left(1+\vec{n}\cdot\vec{\beta}\right)}\right|_{t_r}. \end{aligned} \tag{2.5}$$

These equations are known as the Liénard–Wiechert potentials, which express the magnetic and electric potential of the moving charge as a function of charge parameters at the retarded time, t_r, and $\vec{n} = \vec{R}/R$ is the unit vector of the direction from the observer to the radiating charge.

Using the potential definition (2.2), the electric field of a moving charge can be derived from the Liénard–Wiechert potentials. Then, the equation for the electric field of a charge, q, moving with velocity, v, becomes [15]

$$4\pi\epsilon_0\frac{\vec{E}}{q} = \frac{1-\beta}{r^3}\left(\vec{R}+R\vec{\beta}\right)_r + \frac{1}{cr^3}\left\{\vec{R}\times\left[\left(\vec{R}+R\vec{\beta}\right)_r\times\frac{d\vec{\beta}}{dt_r}\right]\right\}\Bigg|_r, \tag{2.6}$$

In Equation 2.6, the first term is called the velocity field. This part is inversely proportional to a square of the distance between radiation source and observation point. For a charge at rest ($\beta = 0$) this term is reduced to the Coulomb field of a point charge q. For highly relativistic particles, it is noted that the Coulomb field becomes very small.

The second term is called the radiation field. Therefore, in the following we will concentrate on the radiation (second term) from moving charges. The electrical field in the radiation regime becomes

$$4\pi\epsilon_0\left.\frac{\vec{E}}{q}\right|_{rad} = \frac{1}{cr^3}\left\{\vec{R}\times\left[\left(\vec{R}+R\vec{\beta}\right)_r\times\frac{d\vec{\beta}}{dt_r}\right]\right\}\Bigg|_r, \tag{2.7}$$

The magnetic radiation field can be obtained by [15]

$$4\pi c\epsilon_0 \frac{\vec{B}(t)}{q}\bigg|_{rad} = -\frac{R}{cr^2}\left[\frac{d\vec{\beta}}{dt}\times\hat{n}\right]_r + \frac{R}{cr^3}\left\{\frac{d\vec{\beta}}{dt}\cdot\vec{R}\right\}\left[\vec{\beta}\times\hat{n}\right]_r. \tag{2.8}$$

Regarding to the Equation 2.8, the magnetic field can be obtained from the electric field, and vice versa, by;

$$\vec{B} = \frac{1}{c}\left[\vec{E}\times\hat{n}\right]_r. \tag{2.9}$$

In Equation 2.9, the electric and magnetic fields are orthogonal to each other and they are also orthogonal to the direction of observation $\hat{n}$. The electric and magnetic fields of the radiated electromagnetic wave give rise to an energy transport to space. The energy per unit time, per unit area, transported by the field is described by the Poynting vector [16]:

$$\vec{S} = \frac{1}{c\mu_0}\left[\vec{E}\times\vec{B}\right]_r = \epsilon_0 c\left[\vec{E}\times\left(\vec{E}\times\hat{n}\right)\right]_r. \tag{2.10}$$

The Equation 2.6 and Equation 2.10 contain the significant information about the radiation field in terms of angular, spectral and temporal distribution. The equations have to be evaluated for the particular case under consideration.

For a particle moving along a circular trajectory, they lead to the radiation fields of normal synchrotron radiation. For a sinusoidal trajectory to those undulator radiation which will be treated in the following subsections.

2.1.2. Magnetic Field of Planar Undulator

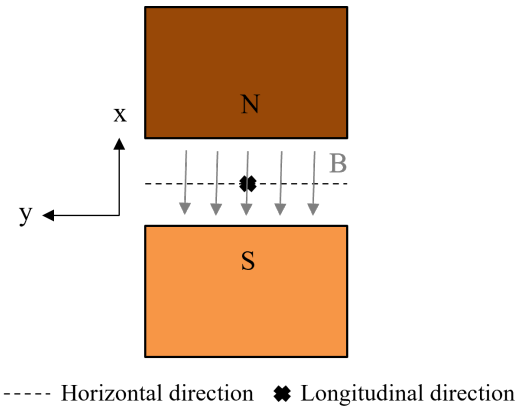


Figure 2.1.: Diagram explaining the planar undulator scheme.

Figure 2.1 shows a diagram explaining a conventional planar undulator, which has uniform magnetic fields in the horizontal direction. The undulator axis is located in the center of the undulator gap along the z-direction where the electron beam is inserted. The magnetic fields are vertically directed in the xy-plane. An electron motion in the planar undulator will be described in detail in the following subsection.

The magnet arrangement in the undulator has a period length of λ_u. For simplicity, if the horizontal width of each magnetic pole is assumed to be much larger than λ_u, the position dependence of the field in x-direction can be neglected.

The curl of the magnetic field is zero inside the vacuum chamber of the electron beam. Therefore, the field can be written in term of a gradient of a scalar magnetic potential by the Laplace equation:

$$\vec{B} = -\nabla\Phi_{mag}, \quad \nabla^2\Phi_{mag} = 0. \tag{2.11}$$

The position dependence of the field is neglected, therefore, the Laplace equation of the magnetic potential depends on x and y coordinates by

$$\frac{\partial^2\Phi_{mag}}{\partial y^2} + \frac{\partial^2\Phi_{mag}}{\partial z^2} = 0. \tag{2.12}$$

The solution of Equation 2.12 can be obtained by the method of separation of variables. The field on axis is harmonic, therefore, the solution of the magnetic potential is assumed by

$$\Phi_{mag}(y,z) = f(y)\sin(k_u z), \tag{2.13}$$

where $k_u = 2\pi/\lambda_u$ and $f(y)$ is a function of positions in y-direction, which corresponds to the wave equation by

$$\frac{d^2 f}{dy^2} - k_u^2 f = 0. \tag{2.14}$$

The general solution of Equation 2.14 can be obtained by

$$f(y) = c_1\sinh(k_u y) + c_2\cosh(k_u y). \tag{2.15}$$

Combining Equation 2.13 and Equation 2.15, the vertical field becomes

$$B_y(y,z) = -\frac{\partial\Phi_{mag}}{\partial y} = -k_u[c_1\cosh(k_u y) + c_2\sinh(k_u y)]\sin(k_u z). \tag{2.16}$$

On the plane $y = 0$, B_y should be symmetrical. The term $c_2\sinh(k_u y)$ should be also equal to 0, which means $c_1 = 0$. The term $k_u c_1$ is set to be B_0, and therefore, $B_y(0,z)$ becomes

$$B_y(0,z) = -B_0\sin(k_u z).$$

A general form the vertical field $B_y(y,z)$ is obtained by

$$B_y(y,z) = -B_0\cosh(k_u y)\sin(k_u z). \tag{2.17}$$

The magnetic potential is obtained from the integration of the vertical field over position in y-direction, which is represented as

$$\Phi_{mag}(x,y,z) = -\int B_y(y,z)dy = \frac{B_0}{k_u}\sinh(k_u y)\sin(k_u z). \tag{2.18}$$

For planes $y \neq 0$, the magnetic field possesses a small longitudinal component B_z:

$$\begin{aligned} B_x &= -\frac{\partial \Phi_{mag}}{\partial x} = 0, \\ B_y &= -\frac{\partial \Phi_{mag}}{\partial y} = -B_0\cosh(k_u y)\sin(k_u z), \\ B_z &= -\frac{\partial \Phi_{mag}}{\partial z} = -B_0\sinh(k_u y)\cos(k_u z). \end{aligned} \tag{2.19}$$

If only the field in the symmetry plane $y = 0$ is considered, the periodic magnetic fields in the planar undulator becomes

$$\vec{B} = -B_0\sin(k_u z)\hat{y}, \tag{2.20}$$

where B_0 is peak magnetic field on the undulator axis and $\hat{y}$ is the unit vector in y-direction.

2.1.3. Electron Motion in the Planar Undulator

Trajectory in first order

Periodic magnetic fields in the planar undulator lead the electrons to oscillate and radiate. The transverse acceleration of an electron by the Lorentz force is

$$\gamma m_e \dot{\vec{v}} = -e(\vec{v} \times \vec{B}), \tag{2.21}$$

where γ is the Lorentz factor, m_e is the electron mass, e is the electron charge and $\vec{v}$ is the electron velocity. The results of Equation 2.21 for the magnetic field in the symmetry plane of the planar undulator, Equation 2.20 are two coupled equations of motion;

$$\ddot{x} = \frac{eB_y}{\gamma m_e}\dot{z}, \quad \ddot{z} = -\frac{eB_y}{\gamma m_e}\dot{x}. \tag{2.22}$$

The first order solutions of these equations can be obtained by the approximation of

$$v_z = \dot{z} \approx v = \beta c = const, \quad v_x << v_z.$$

Thus, $\ddot{z} \approx 0$ and the first order solutions of $x(t)$ and $z(t)$ are [17]

$$x(t) \approx \frac{eB_0}{\gamma m_e c\beta k_u^2}\sin(k_u \beta c t), \quad z(t) \approx \beta c t. \tag{2.23}$$

If the initial conditions for $x(t)$ and $z(t)$ are chosen to be

$$x(0) = 0, \quad \dot{x}(0) = \frac{eB_0}{\gamma m_e k_u},$$

the sinusoidal trajectory of the electron and the transverse velocity become [17]

$$\begin{aligned} x(z) &= \frac{K}{\gamma\beta k_u}\sin(k_u z), \\ v_x(z) &= \frac{Kc}{\gamma}\cos(k_u z), \end{aligned} \tag{2.24}$$

where K is an undulator parameter, represented as

$$K = \frac{eB_0}{m_e c k_u}.$$

Trajectory in second order

The longitudinal component of the velocity is not constant due to the sinusoidal trajectory of the electron. The following equation results for the conservation of energy (v^2 = const);

$$\begin{aligned} v_z &= \sqrt{v^2 - v_x^2} = \sqrt{c^2\left(1 - 1/\gamma^2\right) - v_x^2} \\ &\approx c\left(1 - \frac{1}{2\gamma^2}\left(1 + \gamma^2 v_x^2/c^2\right)\right). \end{aligned} \tag{2.25}$$

By applying $v_x = \dot{x}(t)$ from Equation 2.23 and the trigonometric identity of $\cos^2\theta = (1 + \cos(2\theta)/2)$ to the Equation 2.25, the longitudinal velocity becomes [17]

$$v_z(t) = \left(1 - \frac{1}{2\gamma^2}\left(1 + \frac{K^2}{2}\right)\right)c - \frac{cK^2}{4\gamma^2}\cos(2\omega_u t). \tag{2.26}$$

The average longitudinal velocity is

$$\overline{v_z} = \left(1 - \frac{1}{2\gamma^2}\left(1 + \frac{K^2}{2}\right)\right)c \equiv \overline{\beta}c, \tag{2.27}$$

with a condition of $\omega_u = \overline{\beta}ck_u \approx ck_u$. The trajectories of the particle in second order are described by these equations, as follows [17],

$$x(t) = \frac{K}{\gamma k_u}\sin(\omega_u t), \quad z(t) = \overline{v}_z t - \frac{K^2}{8\gamma^2 k_u}\sin(2\omega_u t) \tag{2.28}$$

2.1.4. Radiation of the Planar Undulator

Figure 2.2 shows the traveling path of the electrons inside the undulator and the emission of the undulator radiation. When the relativistic electrons travel in magnetic field, they emit radiations which are concentrated in a narrow cone with opening angle θ of [18]

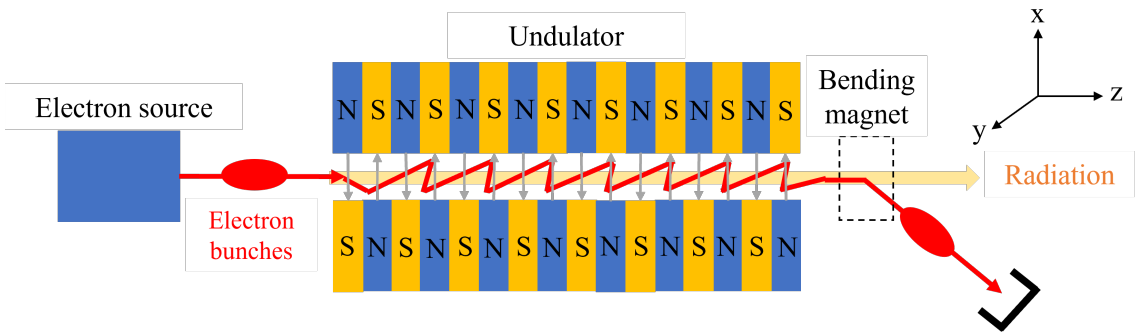


Figure 2.2.: Diagram illustrates a traveling path of electrons inside the undulator magnet and the emission of the undulator radiation. Magnetic fields point in x-axis and a sinusoidal trajectory of the electron is on yz-plane.

$$\theta \approx \pm\frac{1}{\gamma}. \tag{2.29}$$

The center of the radiation cone is on the tangent with respect to the electron trajectory and the direction of the cone varies along the sinusoidal orbit in the undulator. The maximum angle with respect to the undulator axis is

$$\theta_{max} \approx \left|\frac{dz}{dx}\right|_{max} = \frac{K}{\beta\gamma} \approx \frac{K}{\gamma}. \tag{2.30}$$

When the directional variation of the radiation is a little bit smaller than $1/\gamma$, the radiation field obtains contributions from various regions of the electron trajectory. Then, the radiation field can form constructive interference for certain wavelengths. Consequently, the radiation spectrum in forward direction is closely monochromatic.

Radiation in the Moving Coordinate System

A coordinate system (x', y', z') is moving with the average longitudinal velocity of the electrons:

$$\overline{v}_z \equiv \overline{\beta}c, \quad \overline{\gamma} = \frac{1}{\sqrt{1-\overline{\beta}^2}} \approx \frac{\gamma}{\sqrt{1+K^2/2}}. \tag{2.31}$$

The Lorentz transformation from the moving system to the laboratory system are

$$\begin{aligned} t' &= \overline{\gamma}\left(t - \overline{\beta}z/c\right) \approx \overline{\gamma}t\left(1-\overline{\beta}^2\right), \\ x' &= x = \frac{K}{\gamma k_u}\sin\left(\omega_u t\right), \\ z' &= \overline{\gamma}\left(z - \overline{\beta}ct\right). \end{aligned} \tag{2.32}$$

Then, electron orbits in the moving coordinate system are described by

$$x'(t') = a\ \sin(\omega' t'),$$
$$z'(t') = -a\frac{K}{8\sqrt{1+K^2/2}}\sin(2\omega' t'), \tag{2.33}$$

where a is an amplitude of the electron orbit, represented as $a = K/(\gamma k_u)$ and ω' is the frequency of the electron oscillation,

$$\omega' = \overline{\gamma}\omega_u = \overline{\gamma}ck_u \ \approx\ \frac{\gamma ck_u}{\sqrt{1+K^2/2}}. \tag{2.34}$$

If the longitudinal oscillation is ignorable, the electron will emit dipole radiation in the moving system with the frequency of $\omega' = \overline{\gamma}\omega_u$ and the wavelength of $\lambda'_u = \lambda_u/\overline{\gamma}$.

The radiation power from the relativistic charge is given by the Larmor formula [19]:

$$P = \frac{e^2}{6\pi\epsilon_0 c^3}\dot{v}^2, \tag{2.35}$$

where $\dot{v}$ is the proper acceleration and $\dot{v}^2$ must be averaged over one period of the electron oscillation.

In this consideration, there is the acceleration in x-direction only. From Equation 2.32, the acceleration in x-direction is

$$\dot{v}'_x = \frac{d^2x'}{dt'^2} = -\frac{K\gamma c^2 k_u}{1+K^2/2}\sin(\omega' t'). \tag{2.36}$$

Combining the radiation power in Equation 2.35 and the acceleration in x-direction in Equation 2.36, the total radiation power in the moving coordinate system is given by [17]

$$P' = \frac{e^2 c\gamma^2 K^2 k_u^2}{12\pi\epsilon_0\left(1+K^2/2\right)^2} \tag{2.37}$$

For the complex motion of the electrons in the moving frame, it has contributions of the fundamental oscillation and its higher harmonics. As a result, higher harmonics also occur in the radiation field.

Transformation of Radiation into Laboratory System

The light wavelength in the laboratory system as a function of the emission angle, with respect to the beam axis, can be evaluated by using the Lorentz transformation. The photon energy in the moving system ($\hbar\omega'$) can be expressed in terms of the photon energy in laboratory ($\hbar\omega_l$) by

$$\hbar\omega' = \overline{\gamma}\left(E_{ph} - \overline{\beta}cp_{ph}\cos\theta\right) = \overline{\gamma}\hbar\omega_l\left(1 - \overline{\beta}\cos\theta\right), \tag{2.38}$$

where the photon energy (E_{ph}) and the photon momentum (p_{ph}) in the laboratory system are represented as $\hbar\omega_l$ and $\hbar\omega_l/c$, respectively. Then, light frequency in the laboratory system (ω_l) is obtained by

$$\omega_l = \frac{\omega'}{\overline{\gamma}\left(1 - \overline{\beta}\cos\theta\right)}. \tag{2.39}$$

Then, the wavelength in the laboratory (λ_l) is approximated as

$$\lambda_l = \frac{2\pi c}{\omega_l} \approx \lambda_u\left(1 - \overline{\beta}\cos\theta\right). \tag{2.40}$$

By applying $\overline{\beta} = 1 - \left(1 + K^2/2\right)/\left(2\gamma^2\right)$ and $\cos\theta \approx 1 - \theta^2/2$ in Equation 2.40, the wavelength of the undulator radiation when the observation angle (θ) is close to zero can be approximated as [20]

$$\lambda_l = \frac{\lambda_u}{2\gamma^2}(1 + \frac{K^2}{2} + \theta^2\gamma^2), \tag{2.41}$$

The undulator parameter K is proportional to the magnetic field intensity (B_0) and the period length as follows,

$$K = \frac{eB_0\lambda_u}{2\pi m_e c} = 93.36B_0[\mathrm{T}]\lambda_u[\mathrm{m}]. \tag{2.42}$$

The wavelength of the undulator radiation in Equation 2.41 is practically tunable by varying the K parameter because the λ_u and γ are fixed by design. The coherence effects leading to the characteristics of undulator radiation originate from the radiation of single electrons. The contributions (radiation fields) of the electrons in a bunch still add up incoherently, thus, N electrons generate N times the radiation power of a single electron.

For the next step, the radiation power in the laboratory system is evaluated. In the moving system, the longitudinal oscillation of the electron is ignored. Thus, the longitudinal momentum of electron equals zero,

$$z' = 0, \quad P'_z = 0.$$

The Lorentz transformation of the time and total electron energy are given by

$$t = \overline{\gamma}t', \quad E_{tot} = \overline{\gamma}E'_{tot}.$$

Thus, the radiation power in the laboratory system becomes

$$P = -\frac{dE_{tot}}{dt} = -\frac{dE'_{tot}}{dt'} = P'.$$

The total power of undulator radiation, which is accumulated over all harmonics and all observation angles, is given by [17]

$$P_{rad} = \frac{e^4\gamma^2 B_0^2}{12\pi\epsilon_0 c m_e^2} = \frac{e^2 c\gamma^2 K^2 k_u^2}{12\pi\epsilon_0}, \tag{2.43}$$

Spectral Energy of Undulator Radiation

In Equation 2.41, the λ_l emitted by the undulator is so-called the fundamental wavelength. However, the undulator also emits other wavelengths beside the λ_l. The fundamental radiation can be associated by the higher harmonic radiations, whose wavelengths are integer fraction of the fundamental one [21].

$$\text{higher harmonic wavelengths} = \frac{\lambda_l}{n}, \quad \text{where } n = 1, 2, 3, 4... \tag{2.44}$$

From the characteristic feature of the undulator radiation with a narrow spectrum, an evaluation of a width of the emission line for the fundamental harmonic in forward direction is considered in this section. It is assumed that an electron passes through an undulator with N_u periods and produces a wave train with N_u oscillations in a time of $T = N_u\lambda_1/c$. The electric field of the light wave is defined by [17]

$$\begin{aligned} &E_l(t) = E_0 \exp(-i\omega_l t) \quad (-T/2 < t < T/2), \\ &E_l(t) = 0 \quad (\text{otherwise}). \end{aligned} \tag{2.45}$$

This wave train is not monochromatic due to its finite length. It can be replaced by a frequency spectrum which is a result of the Fourier transformation of the step function in time,

$$\begin{aligned} A(\omega) &= \int_{-\infty}^{+\infty} E_l(t) e^{i\omega t} dt = E_0 \int_{-T/2}^{+T/2} e^{-i(\omega_l - \omega)t} dt \\ &= 2E_0 \cdot \frac{\sin((\omega_l - \omega)T/2)}{\omega_l - \omega}. \end{aligned} \tag{2.46}$$

The spectral intensity is proportional to the absolute value of the result of the Fourier transformation, $A(\omega)$, by [20]

$$I(\omega) \propto \left|A(\omega)\right|^2 \propto \left(\frac{\sin\xi}{\xi}\right)^2, \tag{2.47}$$

where

$$\xi = \frac{(\omega_l - \omega)T}{2} = \pi N_u \frac{\omega_l - \omega}{\omega_l}.$$

The spectral purity or line width is determined by the shape of the $(\sin\xi/\xi)$-function. The line width is defined by the frequency at which $\sin\xi/\xi = 0$ or where $\pi N_u \Delta\omega/\omega_l = \pi$ [20]:

$$\frac{\Delta\omega}{\omega_l} = \pm\frac{1}{N_u}. \tag{2.48}$$

The spectral width of the undulator radiation decreases when the period number increases. For the first harmonic around $\theta = 0$, the photon spectrum is determined by the $(\sin\xi/\xi)$-function. The resonant condition for the photon spectrum can be defined by

$$\frac{\omega_l(\theta)}{\omega_l(0)} = \frac{1 + K^2/2}{1 + K^2/2 + \gamma^2\theta^2}. \tag{2.49}$$

Assuming the undulator when $N_u \gg 1$, the rms opening angle of the undulator radiation is defined by [20]

$$\sigma_\theta \approx \frac{1}{\gamma} \cdot \sqrt{\frac{1 + K^2/2}{2N_u}} \approx \frac{1}{\gamma} \cdot \frac{1}{\sqrt{N_u}}, \quad (K \approx 1). \tag{2.50}$$

The undulator radiation is emitted into a solid angle defined by this small opening angle

$$\Delta\Omega = \pi\sigma_\theta^2. \tag{2.51}$$

Equation 2.51 is referred to as the radiation cone in the forward direction. The opening angle of the undulator radiation becomes narrower (collimated) as the N_u increases.

Photon Beam Brightness

The spectral brightness describes an intensity of the radiation source by taking its spectral line width and opening angle of the radiation cone into account, given by [22]

$$B = \frac{\Phi}{4\pi^2\Sigma_x\Sigma_{\theta x}\Sigma_y\Sigma_{\theta y}}, \tag{2.52}$$

where Φ is the spectral photon flux density defined by the numbers of emitted photon per second within a relative spectral bandwidth of $\Delta\omega_l/\omega_l$. The photon flux density is evaluated by a quantisation of the radiation power. The brightness can determine how much the monochromatic radiation can be focused into a small spot on the target.

Quantities Σ_x, $\Sigma_{\theta x}$, Σ_y, and $\Sigma_{\theta y}$ are evaluated from the transverse rms sizes and angular divergence of the photon and the electron beam in x and y-directions, respectively, as follows,

$$\Sigma_x = \sqrt{\sigma_{x,ph}^2 + \sigma_{x,e}^2}, \quad \Sigma_{\theta x} = \sqrt{\sigma_{\theta x,ph}^2 + \sigma_{\theta x,e}^2} \tag{2.53}$$

and

$$\Sigma_y = \sqrt{\sigma_{y,ph}^2 + \sigma_{y,e}^2}, \quad \Sigma_{\theta y} = \sqrt{\sigma_{\theta y,ph}^2 + \sigma_{\theta y,e}^2}. \tag{2.54}$$

Quantities $\sigma_{x,ph}$ and $\sigma_{x,e}$ are transverse rms sizes of the photon and the electron beam in x-direction, respectively. Quantities $\sigma_{\theta x,ph}$ and $\sigma_{\theta x,e}$ are the angular divergence of the photon and the electron beam in x-direction, respectively. Then, quantities $\sigma_{y,ph}$, $\sigma_{y,e}$, $\sigma_{\theta y,ph}$ and $\sigma_{\theta y,e}$ are in the similar definitions for y-direction.

The spectral photon flux of the FEL is referred to as a total number of photons per unit time, $\dot{N} = P_{FEL}/(\hbar\omega_l)$, divided by a relativistic FEL bandwidth [22]:

$$\Phi = \frac{P_{FEL}}{\hbar\omega_l}\left(\frac{\Delta\omega_l}{\omega_l}\right)^{-1}, \tag{2.55}$$

with a relation of $\Delta\omega_l = \sqrt{2\pi}\sigma_{\omega_l}$. Therefore, the spectral photon beam brightness becomes [22]

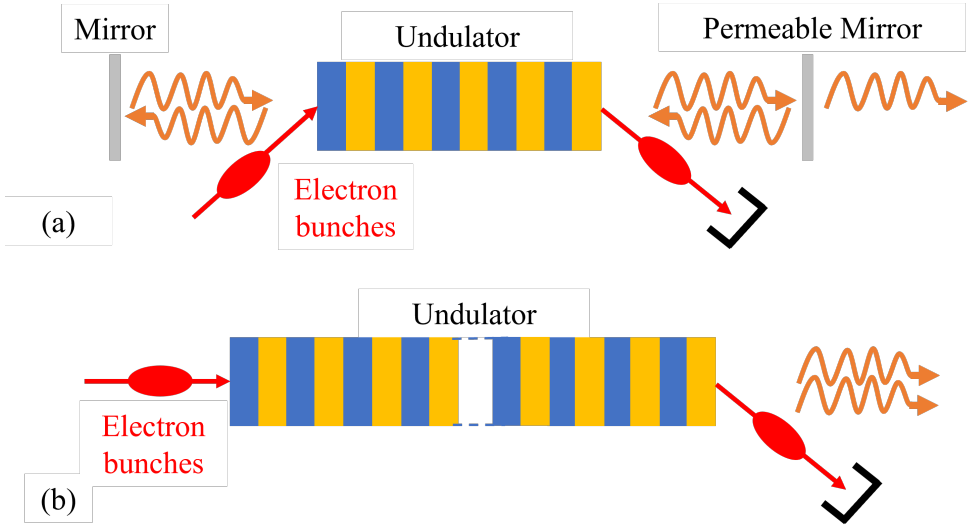


Figure 2.3.: FEL amplification with (a) an optical resonator and (b) SASE mechanism.

$$B_{FEL} = \frac{\sqrt{2}}{\pi^{3/2}\hbar c} \frac{P_{FEL}}{\lambda_l} \frac{\omega_l}{\sigma_{\omega_l}}. \tag{2.56}$$

2.2. Free Electron Laser

The advantages of FEL compared to undulator radiation are much higher intensity, full transverse coherence and short pulse lengths. This is because a large number of electrons radiate coherently. The intensity of the radiation field increases quadratically with the number of coherently radiating particles ($I = N^2 I_1$).

The high peak brightness is a result of the high flux per pulse and the short pulse length. Thus, the FEL has a high peak brightness, which is more than eight orders of magnitude higher than the synchrotron light. In general, the brightness of the FEL is inversely proportional to the square of the photon wavelength [22]

$$B_{FEL} = \frac{4\Phi}{\lambda_l^2}. \tag{2.57}$$

For radiation with relatively long wavelengths like infrared (IR) and visible light, optical resonators are used for amplification, as shown in Figure 2.3 (a). However, optical resonators are no longer possible for the extreme-ultraviolet (EUV) and X-ray radiation when the wavelengths are shorter than 100 nm because the reflectivities of metals and other coating materials for mirrors drop quickly to zero at normal incidence [23].

In Figure 2.3 (a), the bunches of the emitted light travel many turns through the undulator in a forward and backward direction. During each passage an intensity of the emitted light increases by only a few percent.

For this reason, the FEL gain for EUV and X-rays must be achieved from a single passage of the electron bunch through a very long undulator as shown in Figure 2.3 (b). In this

case, the FEL amplification can be achieved by the so-called self-amplified spontaneous emission (SASE) effect described in more detail below [24, 25].

2.2.1. One-Dimensional Theory of the High-Gain FEL

In the 1-D FEL theory of the FEL described in this chapter the initiated bunches are assumed to be very long. Then the longitudinal electric field can be neglected while the charge distribution in the bunch still remains homogeneous.

Energy transferring

Let us assume that a radiation wave with wavelength λ_l is already presented by a spontaneous emission or an external seeding source. The relativistic electron beam and the electromagnetic wave propagate together. In free space, the velocity of electron is perpendicular to the external electric field, therefore, there is no energy transfer ($\Delta E = \vec{v} \cdot \vec{E}_x = 0$).

In the undulator, however a periodic transverse velocity, $\vec{v}_x$, is generated. In this case, the energy transferred between the relativistic electron and the electromagnetic wave is effected by the electric field term of the Lorentz force equation. The amount of transferred energy is

$$\Delta E_x = e \int \vec{v}_x \cdot \vec{E}_x \, dt, \tag{2.58}$$

where v_x is a transverse velocity through the periodic oscillation in the undulator and E_x is the transverse electric field of the light wave which can be expressed by

$$E_x(z,t) = E_{0,l} \cos\left(k_l z - \omega_l t + \psi_0\right), \tag{2.59}$$

with $k_l = \omega_l / c = 2\pi/\lambda_l$ and the transverse velocity of the electron (v_x) is

$$v_x(t) = \frac{cK}{\gamma} \cos\left(k_u z\right). \tag{2.60}$$

The energy transfer per unit time from the electron to the light wave is described by [26]

$$\frac{dE}{dt} = -e v_x(t) E_x(t) = -\frac{ecKE_0}{2\gamma} \Big[\cos\left((k_l + k_u)z - \omega_l t + \psi_0\right) + \cos\left((k_l - k_u)z - \omega_l t + \psi_0\right) \Big]. \tag{2.61}$$

In Equation 2.61, the argument (ψ) of the first cosine function is introduced as a ponderomotive phase. This parameter is a function of position z of electron, which is a function of t. Therefore, the ponderomotive phase can be written as a function of time by

$$\psi = (k_l + k_u)z - \omega_l t + \psi_0. \tag{2.62}$$

This resonance condition is derived by demanding a constant ponderomotive phase ($d\psi/dt = 0$). A fundamental wavelength of undulator radiation corresponds to a continuous energy transferred from the relativistic electrons to the electromagnetic wave or stimulation of radiation emission by an external field is given by [27]

$$\lambda_l = \frac{\lambda_u}{2\gamma^2}\Big(1 + K^2/2\Big). \tag{2.63}$$

The Equation 2.63 is identical to the definition of the fundamental undulator radiation wavelength. According to this reason, it is convenient to apply the spontaneous undulator radiation as the external light to initiate the FEL amplification.

Equation of Motion

A consideration is treated as a light amplification. Assuming that the lasing process in the undulator is initiated by an incident monochromatic light wave with the electric field amplitude of E_0 and wavelength of λ_l. A resonance electron energy

$$E_r = \gamma_r m_e c^2$$

is defined by

$$\gamma_l = \frac{\lambda_u}{2\gamma_r^2}\left(1 + \frac{K^2}{2}\right). \tag{2.64}$$

It is expected that electrons with the energy of E_r must emit the undulator radiation with the wavelength, which is identical to the seed wavelength λ_l. Here, a parameter of the relative energy deviation η is defined by

$$\eta = \frac{E - E_r}{E_r} = \frac{\gamma - \gamma_r}{\gamma_r}, \quad \big|\eta\big| << 1. \tag{2.65}$$

A time derivative of the ponderomotive phase

$$\frac{d\psi}{dt} = (k_l + k_u)\overline{v}_z - \omega_l \approx k_u c - \frac{k_l c}{2\gamma^2}\left(1 + \frac{K^2}{2}\right), \tag{2.66}$$

$$\frac{d\psi}{dt} = \frac{k_l c}{2}\left(1 + \frac{K^2}{2}\right)\left(\frac{1}{\gamma_r^2} - \frac{1}{\gamma^2}\right) \tag{2.67}$$

At Equation 2.67, it can be approximated by using the Equation 2.65 and the result becomes

$$\frac{d\psi}{dt} = 2k_u c\eta. \tag{2.68}$$

A time derivative of the relative energy deviation η is

$$\frac{d\psi}{dt} = -\frac{eE_0 K}{2m_e c\gamma_r^2}\cos\psi. \tag{2.69}$$

The Equation 2.68 and Equation 2.69 are called a pendulum equation.

Microbunching

The lasing process is initiated by a spontaneous emission or an external seeding source with the wavelength λ_l and the electron beam energy is chosen to obey the resonance condition. At the beginning, charge density is distributed almost uniformly along the bunch of N_e particle.

During the passage through the undulator, the interaction with the periodic light wave will gradually produce a periodic density modulation. The process of microbunching is based on principle: electrons lose energy to the light wave traveling on sinusoidal with a larger amplitude than electrons gain the energy from the light wave.

Result is modulation of longitudinal velocities of electrons. This result finally leads the electron bunch to reshape to a series of shorter microbunches, which are shorter than the light wavelength γ_l. Those microbunches are close to the positions where the maximum energy transfer to the light wave can happen. The electric field of the light wave in the undulator is given by [28, 29]

$$\tilde{E}_x(z,t) = \tilde{E}_x(z)\exp\left(i(k_l z - \omega_l t)\right), \tag{2.70}$$

where $\tilde{E}_x(z)$ is a function of z, which is the solution of the 3rd order FEL differential equation, as mentioned above.

FEL Gain

The interaction between the relativistic electron and the light wave depends on the relative energy deviation $\eta = (\gamma - \gamma_r)/\gamma_r$. This section considers a quantitative description about the energy gain, the energy transfer between the electron and light wave. The FEL gain function can be defined by a relative growth of the light intensity during a single passage of the undulator.

$$G = \frac{\Delta I_l}{I_l}, \quad I_l = c\frac{\epsilon_0}{2}E_0^2.$$

The gain function, named as the Madey theorem, can be expressed by [30]

$$G(\omega) = -\frac{\pi e^2 \widehat{K}^2 N_u^3 \lambda_u^2 n_e}{4\epsilon_0 m_e c^2 \gamma_r^3} \cdot \frac{d}{d\xi}\left(\frac{\sin^2\xi}{\xi}\right), \quad \xi = \xi(\omega) = \pi N_u \frac{\omega_l - \omega}{\omega_l}. \tag{2.71}$$

Where n_e is the number of electrons per unit volume, N_u is the number of undulator period, $\widehat{K}$ is the modified undulator parameter. Equation 2.71 states that the FEL gain curve is proportional to the negative derivative of the lineshape curve $(\sin^2\xi/\xi)$ of the undulator radiation.

The FEL gain curve is considered as a function of the energy offset. Then, the quantity ξ is written as a function of γ, which is approximated as

$$\xi = \pi N_u \frac{\omega_l - \omega}{\omega_l} = -2\pi N_u \frac{\gamma_r - \gamma}{\gamma_r}.$$

The FEL gain as a function of the relative energy deviation η becomes [26]

$$G(\eta) = -\frac{\pi e^2 \widehat{K}^2 N_u^3 \lambda_u^2 n_e}{4\epsilon_0 m_e c^2 \gamma_r^3} \cdot \frac{d}{d\xi}\left(\frac{\sin^2 \xi}{\xi}\right), \quad \xi = \xi(\eta) = 2\pi N_u \eta. \tag{2.72}$$

By the Equation 2.72, electrons with positive η enhance the intensity of the interacted light wave while those with negative η reduce the intensity.

In order to obtain an appreciable gain in the FEL driven by the seed radiation, the electrons must fulfill these following conditions. The electron energy E must be close to the resonance energy E_r to enable continuous energy transfer from the relativistic electron beam to the light wave along the undulator. At this condition, the relative energy deviation $\eta = (E - E_r)/E_r$ must stay within the the bandwidth ($\Delta\omega/\omega_l$) of the lineshape curve of the undulator radiation.

FEL parameter

Theoretical considerations also require that the beam energy spread should be less than the FEL-parameter. Thus, a general requirement of the relative rms energy spread (σ_δ) of the electron beam in a high gain FEL is [31]

$$\sigma_\delta = \frac{\sigma_\gamma}{\gamma_0} \ll \rho, \tag{2.73}$$

where ρ is the FEL parameter, σ_γ and γ_0 are the rms energy spread and the Lorenz factor related to the electron energy E_0, respectively. The FEL parameter is given by [29]

$$\rho = \frac{1}{4\pi\sqrt{3}} \frac{\lambda_u}{L_{G0}}, \tag{2.74}$$

where L_{G0} is an idealized gain length of FEL in the one-dimensional theory.

Power Gain Length

The power gain length is defined by [29]

$$L_{G0} = \frac{1}{\sqrt{3}\,\Gamma} = \frac{1}{\sqrt{3}} \left[\frac{4\gamma_r^3 m_e}{\mu_0 \widehat{K}^2 e^2 k_u n_e}\right]^{1/3}, \tag{2.75}$$

where Γ is called the gain parameter. An index zero in the Equation 2.75 indicates that L_{G0} is an ideal gain length of the one-dimension theory which assumes the electron beam is monochromatic and a space charge force is neglected.

An increasing of the photon intensity along the undulator is exponential because the bunching depends on the photon intensity itself, which is given by

$$I \propto I_0 \exp\left(\frac{z}{L_G 0}\right). \tag{2.76}$$

Finally, the saturation is reached and the intensity of photon does not grow anymore. The peak photon pulse at a saturation condition is given by

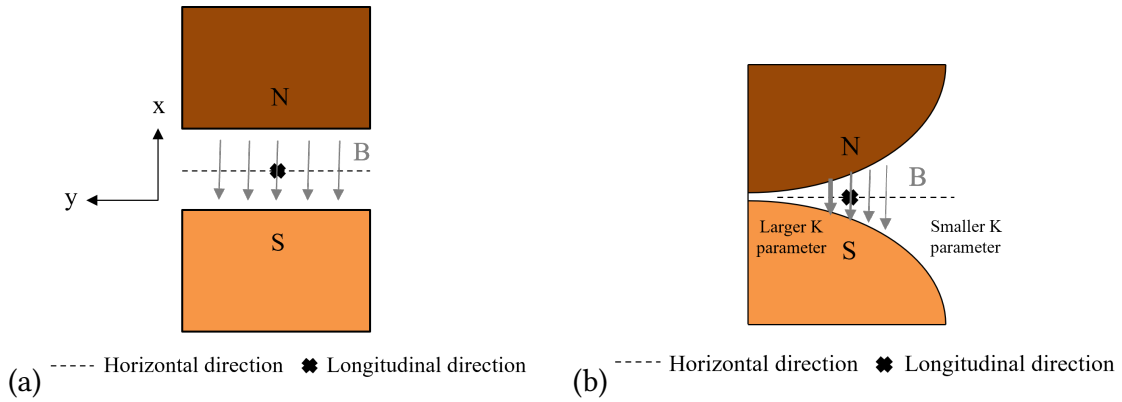


Figure 2.4.: Diagrams showing (a) a planar undulator and (b) a cylindrical TGU.

$$P_{\text{peak}} = \frac{\rho_T N_e E}{\sqrt{2\pi}} \cdot \frac{1}{\tau_{b,rms}} = \rho_T I_{\text{peak}} \frac{E}{e}, \tag{2.77}$$

where ρ_T is an effective FEL parameter, $\tau_{b,rms}$ is a pulse duration of the beam, E is an electron energy and I_{peak} is a peak current of the electron beam.

2.3. Transverse Gradient Undulator

The electron beam generated by a LWFA has extreme initial conditions because the electrons experience non-uniform and unprecedentedly strong electric fields generated by the plasma wave inside the electron source. The TGU was developed for generating radiation with a narrow energy spectrum with LWFA electron beams having a high energy spread [14].

Figure 2.4 shows a comparison of the planar undulator with the TGU scheme with cylindrical pole shape. Magnetic fields point in x-axis and a sinusoidal trajectory of the electron is on the yz-plane.

In a conventional planar undulator, which has uniform magnetic fields in the transverse (horizontal) positions, a low energy-spread electron beam is used in general, which travels along the center beam axis in the undulator. As a result, the radiation from the undulator has coherent characteristics with a narrow energy spectrum.

In contrast, the TGU is used for electron beams with a higher energy spread such as the LWFA ones. Electrons with different energies travel at different transverse positions inside the TGU. The vertical flux density amplitude depends on transverse position, i.e. the undulator field exhibits a transverse gradient.

Electrons with different energies experience different undulator parameter values and emit radiation at similar wavelengths [14, 31]. Therefore, the resultant radiation can have a narrow energy spectrum by compensation of the energy spread of the electron beam.

2.3.1. Basic Principle of Radiation and FEL Amplification in a TGU

The dispersion plane of the TGU corresponds to the horizontal plane in the Figure 2.4(b). The vertical magnetic flux density B_y and the undulator parameter K are dependent on the transverse position:

$$B_y(x) = B_0(x)\cos\left(\frac{2\pi z}{\lambda_u}\right)\hat{y} \quad , \quad K(x) = \frac{eB_0(x)\lambda_u}{2\pi m_e c}, \tag{2.78}$$

where $B_0(x)$ is the magnetic field amplitude dependent on the transverse position. The relative transverse gradient is given by

$$\alpha = \frac{1}{K_0}\frac{\partial K(x)}{\partial x}, \tag{2.79}$$

where K_0 is the undulator parameter at the position with the central electron energy of E_0 and $\partial K(x)/\partial x$ is the transverse K-gradient.

It has been suggested by the publication [31], that the TGU scheme can also be applied to enable FEL amplification with LWFA electrons although they do not satisfy the $\sigma_\delta << \rho_{\mathrm{FEL}}$ condition.

For the TGU, electron beam is dispersed in the horizontal plane. This dispersion reduces the density of the beam and the coupling relation to the radiation via the FEL parameter. To account for this effect, a modified FEL parameter ρ_T for the TGU is defined by

$$\rho_T = \rho\left(1 + \frac{\eta^2\sigma_\delta^2}{\sigma_x^2}\right)^{-\frac{1}{6}}, \tag{2.80}$$

where σ_x is the average rms transverse beam size (without dispersion) when the electron beam travels through the TGU and η is the horizontal dispersion function, which fulfils the matching condition to the TGU gradient

$$\eta = \frac{2 + K_0^2}{\alpha K_0^2}. \tag{2.81}$$

The intrinsic horizontal beam size will present an effective energy spread inside a TGU by [31]

$$\sigma_\delta{}^{\mathrm{eff}} = \frac{K_0^2}{2 + K_0^2}\frac{\sigma_K}{K_0} = \frac{K_0^2}{2 + K_0^2}\alpha\sigma_x. \tag{2.82}$$

If a relatively short undulator of length L_u is considered, the intrinsic beam size can be assumed to be determined by the horizontal emittance (ε_x) and the beta function (β), and it is reasonable to assume that

$$\sigma_x = \sqrt{\varepsilon_x L_u/2}, \quad \beta \approx L_u/2.$$

Based on these assumptions, the modified 1-D FEL gain length for the TGU (equivalent to the gain length L_{G0}) can be approximated by [31]

Table 2.1.: Specifications of the Nb-Ti SC wire used for the TGU.

Parameter	Value	Unit
SC wire dimension (bare)	1.00×0.60	mm^2
SC wire dimension	1.08×0.68	mm^2
Shape	Rectangular	
Cu:SC ratio	1.35:1	
Number of filament	54	
Critical temperature [32]	9.4	K
Operating Temperature	4.2	K
Critical current at 4.2 K and 6 T	443	A

$$L_G^T = \frac{\lambda_u}{4\pi\sqrt{3}\rho_T}\left(1 + \left(\frac{K_0^2}{2+K_0^2}\right)^2 \frac{\alpha^2 \varepsilon_x L_u}{2\rho_T^2}\right). \tag{2.83}$$

It is expected that the TGU could significantly reduce the gain length when $\sigma_\delta > \rho$ and the FEL radiation could be obtained.

2.3.2. The Superconducting TGU demonstrator built at KIT

For the LWFA-based FEL in UV to X-ray wavelength regime, a superconducting (SC) cylindrical TGU is beneficial due to short periods, high fields and large transverse gradients. The cylindrical pole shape also provides the maximum transverse gradient larger than that in the tilted rectangular coil [14].

The SC material used for the TGU is a Niobium-Titanium (Nb-Ti) multifilament wire. A SC wire with rectangular cross section was selected because it could provide a better performance of wiring in the groove of the copper coil former [12] than a wire with circular cross section. The specifications of the Nb-Ti SC wire are listed in Table 2.1.

The TGU consists of two cylindrical yokes made of oxygen-free high conductivity copper (OFHC), the SC coils, and the rectangular OFHC support structures [33]. A photograph of the TGU designed and fabricated at KIT is shown in Figure 2.5. The design parameters of the TGU and the operation requirements are also summarized in Table 2.2.

2.3.3. Cryostat Configuration

For the experiments described in this thesis, the TGU has been operated and tested in vacuum inside its own cryostat, which was designed and manufactured by CRYOVAC GmbH, Germany. A sectional view of the cryostat and its temperature regions is shown in Figure 2.6. The specifications of the cryostat are also summarized in Table 2.3.

The cryostat is equipped with thermal shields at temperature levels of 4 , 40 and 77 K cooled by liquid helium (LHe), helium vapor and liquid nitrogen (LN_2), respectively. The TGU is placed between the LHe tank bottom and two LHe-cooled heat exchanger plates inside the 4 K thermal shield. For the liquid nitrogen system, the cylindrical container

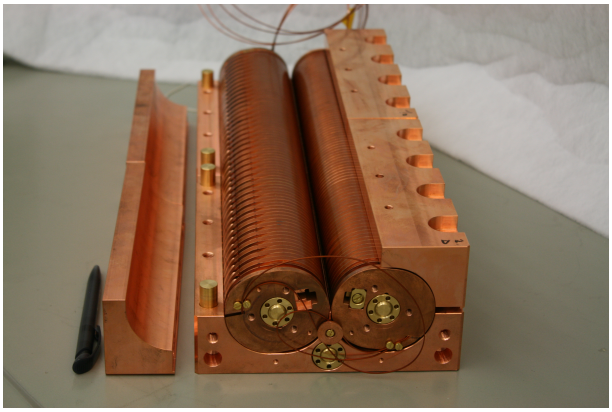


Figure 2.5.: A photograph of the SC TGU with its support structures [12].

Table 2.2.: Design parameters of the SC TGU developed at KIT.

Parameter	**Value**	**Unit**
Central energy of electron beam (E_0)	120	MeV
Relative energy acceptance ($\Delta E/E_0$)	±10	%
Period number (N_u)	40	
Period length (λ_u)	10.50	mm
Gap width at E_0	2.40	mm
Radius of the copper coil former	30	mm
Peak field on axis	1.1	T
Undulator parameter at E_0	1.10	
SC wire material	Nb-Ti	
Number of SC wire layer	6	layer
Number of SC wire turn per layer	4	turn

is placed on top of the cryostat and has a capacity of 173 L. In case of the liquid helium system, the half-cylinder container is placed inside the 4 K thermal shield, which is the green structure in Figure 2.6.

The cryostat has four current-feedthroughs for both TGU coils, which consist of normal conducting parts present in air and vacuum, respectively, and high temperature superconducting (HTS) parts on vacuum side. The vacuum-side normal conducting parts are located between the vacuum feedthroughs and the 77 K-connection point of the HTS leads. The HTS leads connect the 77 K and 4 K level. At 4 K level, all further connections are low temperature superconducting (LTS) wires.

Heat from the TGU can be transferred to both the bottom of the LHe reservoir and the LHe-cooled heat exchanger plates. This condition allows the cryostat to cool the TGU. A cool-down procedure using the cryogenic liquids will be described in the following section.

A multi-stage roots pump and a turbopump were used for generating the vacuum in the recipient. In the first step, the multi-stage roots pump was used to reduce a pressure inside the cryostat to an order of 10 Pa. In the second step, the turbopump was used to reduce

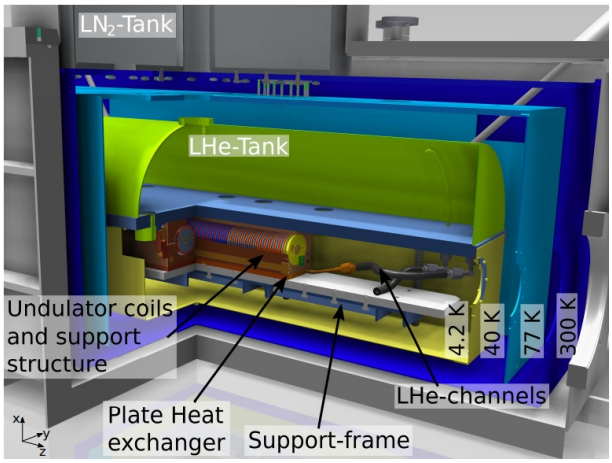


Figure 2.6.: Sectional view of the cryostat assembly in different temperature regions. The TGU is placed in vacuum and conduction-cooled condition [33].

the pressure to an appropriate pressure to start the TGU cool-down procedure, which was in an order of 10^{-3} Pa at room temperature. The TGU operating pressure was in an order of 10^{-6} Pa while the TGU temperature was around 4.3 K. Photographs of vacuum components assembled to the cryostat in the experiments are shown in Figure 2.7.

Table 2.3.: Specifications of the cryostat for the TGU.

Parameter	Value	Unit
Recipient shield		
Operating temperature	> 280	K
Operating pressure	0-120	kPa
Internal volume	≈ 500	L
Medium	Vacuum	
Liquid nitrogen system		
Operating temperature	77	K
Operating pressure	0-145	kPa
Liquid containing volume	173	L
Liquid helium system		
Operating temperature	4.2	K
Operating pressure	0-145	kPa
Liquid containing volume	50	L

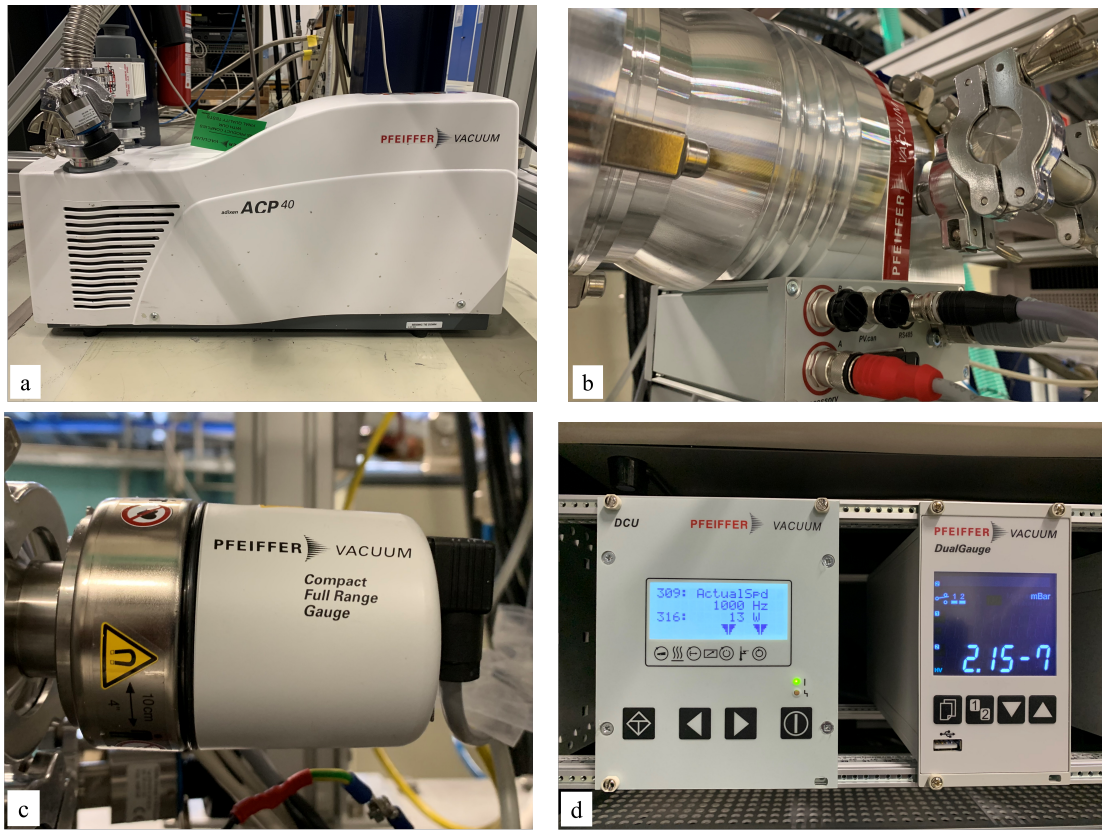


Figure 2.7.: Photographs of (a) multi-stage roots pump, (b) turbopump, (c) full-range pressure gauge and (d) controlling device of the turbopump and pressure monitor.

3. Operation and Characterization of Superconducting TGU

The TGU under investigation in this thesis is a superconducting magnet. Its operation requires a refrigeration of the magnet to liquid helium (LHe) temperature at 4.2 K. The installation of the TGU and the temperature sensors attached on the TGU will be described in section 3.1. The LTS wiring of the magnet in the cryostat will be described in section 3.2. The cool-down procedure together with several required optimization steps to reach full magnetic performance and the magnetic powering tests will be described in section 3.3 and section 3.4, respectively.

3.1. TGU Installation

Figure 3.1 shows the installation of the TGU. The outermost shield at room temperature and the thermal shields at 77 K, 40 K, and 4 K were removed. The LHe-cooled heat exchanger plates were placed on the main support structure and the TGU was placed on the heat exchanger plates, consequently. Then, they were lifted together in the vertical direction to place and to adjust the position of the TGU below the bottom of LHe reservoir.

Polyimide sheets were inserted between the bottom of the LHe reservoir and TGU and between the TGU and the heat exchanger plates to avoid a short circuit between the TGU coils and the cryostat. In order to maximize the heat transfer between the TGU and the bottom of the LHe tank, additional indium sheets were inserted below the polyimide sheets.

After the position of the TGU was finalized, each heat exchanger plate was connected to LHe transferring tubes. The temperature sensors were attached on the flat surface of the heat exchanger plates, TGU support structures and coil yokes. Properties and types of the temperature sensors will be described in this section.

Temperature Sensor attached to the TGU

There are two types of temperature sensors employed in the TGU experiments in order to monitor the temperature at different points and levels inside the cryostat. The temperature sensors are silicon diode-based temperature sensor (DT-670A-CU) and resistance-based temperature sensor (PT-100 series) employed for the temperature ranges 4 K to 20 K and 20 K to 293 K, respectively. Both types of sensors were manufactured by Lake Shore Cryotronics.

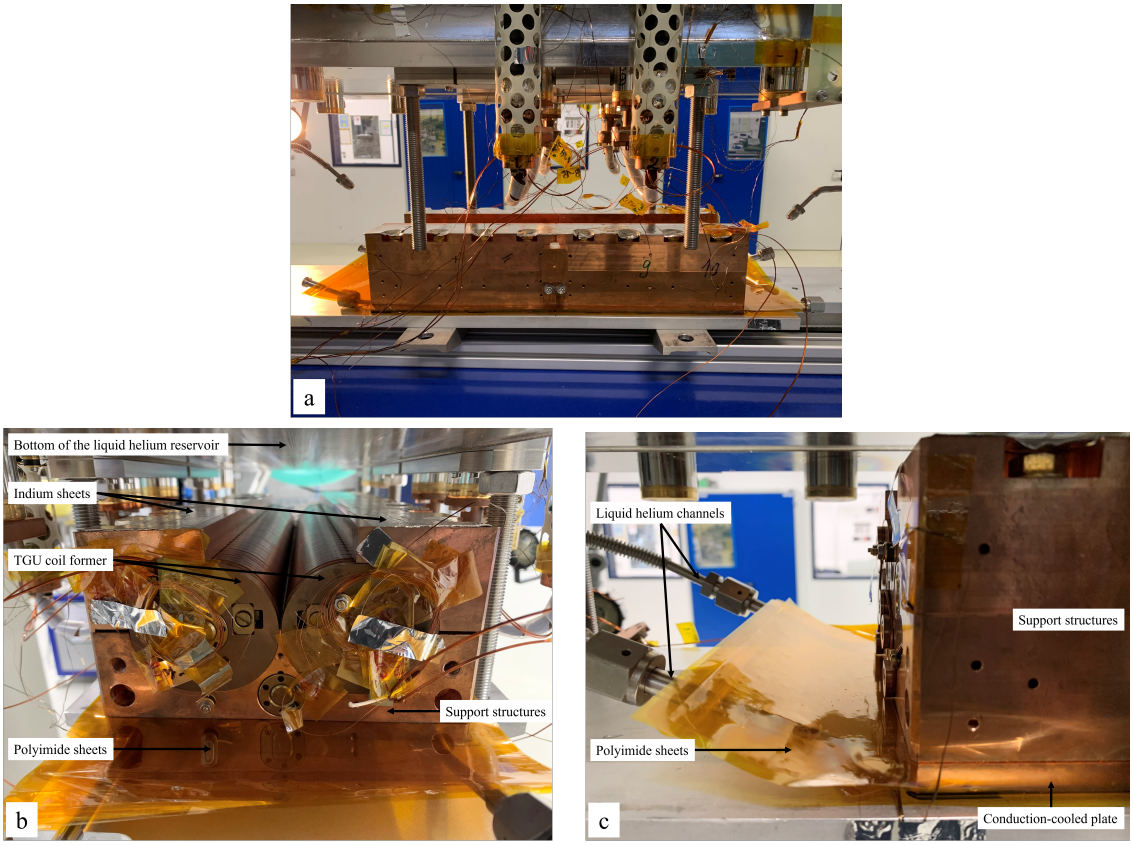


Figure 3.1.: (a) The TGU and heat exchanger plates placed on the main support structure of the cryostat, (b) a front and (c) a side view photographs explaining the additional indium sheets and the inserted polyimide sheets.

Diode-based temperature sensor

The sensor thermometry is based on the measurement of the voltage of the diode as a function of its temperature at a constant applied current. For the TGU measurements, silicon diode sensor (DT-670A-CU) were used with an applied current of 10 µA.

This sensor is appropriate for the TGU operating temperature at 4.3 K to 4.4 K and sufficient for a wide temperature range during the cool-down procedure. General specifications of the DT-670 temperature sensor are summarized in Table 3.1.

Phosphor bronze wires with a diameter of 0.203 mm manufactured by Lake Shore Cryotronic [34] were used for connecting the temperature sensors. Those phosphor bronze wires are cryogenic wires which have a small thermal conductivity to minimize an external heat flowing through the wires into the cryostat.

Table 3.1.: Specifications of the diode-based temperature sensors used in the TGU experiments [35].

Parameter	Value	Unit
Diode-based sensor (DT-670A-CU)		
Minimum temperature limit	1.4	K
Maximum temperature limit	420	K
Sensitivity (at 10 µA and 4.4 K)	−32.9	$mV\,K^{-1}$
Tolerance (2 K to 100 K)	±0.25	K
Tolerance (100 K to 305 K)	±0.5	K

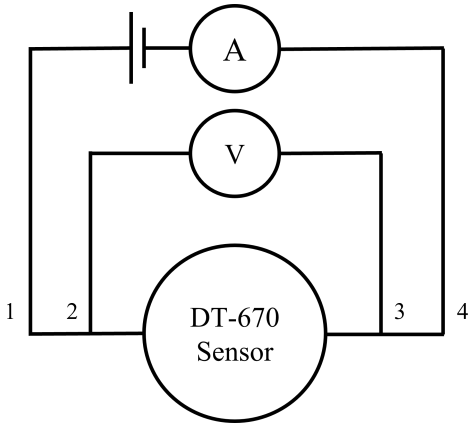


Figure 3.2.: Diagram explaining the 4-terminal sensing method for measuring the voltage of the temperature sensors.

The voltage of the sensor was measured using 4-terminal sensing method which uses two wires for applying the current to the sensor and two different wires for measuring the voltage, as schematically shown in Figure 3.2.

The lead and contact resistance are eliminated from the measurement due to the separation of the current and measured voltage wires. The advantages of the 4-terminal sensing method is that the measured voltage values are independent of intrinsic properties of the wires.

A standard calibration curve of the DT-670 sensor is shown in Figure 3.3. The sensitivity of the sensor is a critical parameter, which is defined by the derivative of the voltage drop as a function of temperature of the sensor. The dependency of the sensitivity on temperature is shown in Figure 3.4.

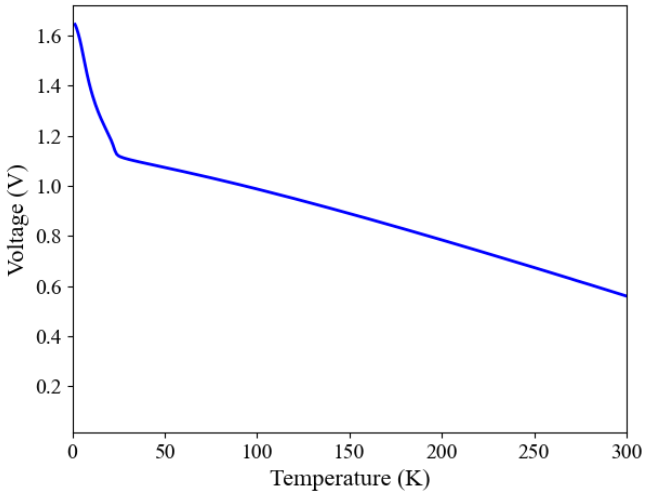


Figure 3.3.: Voltage of the DT-670 series silicon diode sensor as a function of its temperature at a constant current [35].

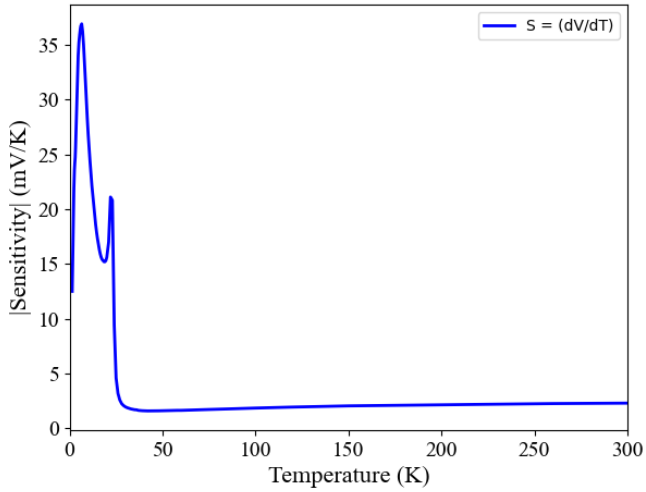


Figure 3.4.: Absolute value of the sensitivity of the DT-670 series silicon diode sensor as a function of temperature [35].

As shown in Figure 3.4, the DT-670A-CU silicon diode sensor has a high sensitivity in the temperature range between the operating and critical temperature of the TGU, which are 4.3 K to 4.4 K and 9.4 K, respectively. For this reason, the silicon diode sensors were utilized for the TGU coil, support structures, heat exchanger plates, 4 K-current leads and 4 K-thermal shield.

Table 3.2.: Specifications of the PT-100 sensors used in the TGU experiments [36].

Parameter	Value	Unit
Resistance-based sensor (PT-102-AL)		
Minimum temperature limit	14	K
Maximum temperature limit	500	K
Sensitivity (at 77 K)	0.423	$\Omega\,K^{-1}$
Sensitivity (at 200 K)	0.400	$\Omega\,K^{-1}$

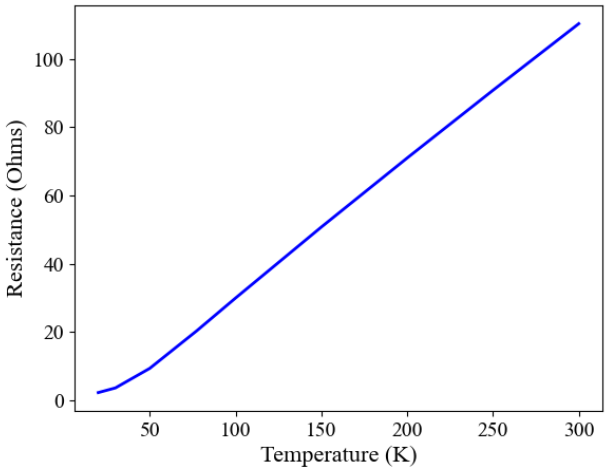


Figure 3.5.: Dependency of resistance of the PT-100 sensor on temperature below 300 K [36].

Resistance-based temperature sensor

The electrical resistance of various metals such as platinum, copper and nickle almost linearly increases with the absolute temperature. Such an intrinsic property makes the metals usable as temperature sensors.

The resistance-based temperature sensors used in the TGU experiment are platinum sensors (PT-100 series), which are sufficient for cryogenic temperatures down to 20 K. The advantages of the platinum sensors are an excellent long term stability, a high accuracy and suitability for a wide temperature range. Specifications of the PT-100 temperature sensor are summarized in Table 3.2. A standard calibration curve for PT-100 sensors for temperatures below 300 K is shown in Figure 3.5.

The calibration curve can be approximated by a linear relation in different temperature regions. For example, the resistance dependence on the temperature between 77 K and 300 K can be approximated by

$$R = (4.042 \times 10^{-1}) \times T - 10.3496, \tag{3.1}$$

where R is the resistance in Ohm and T is the temperature in Kelvin.

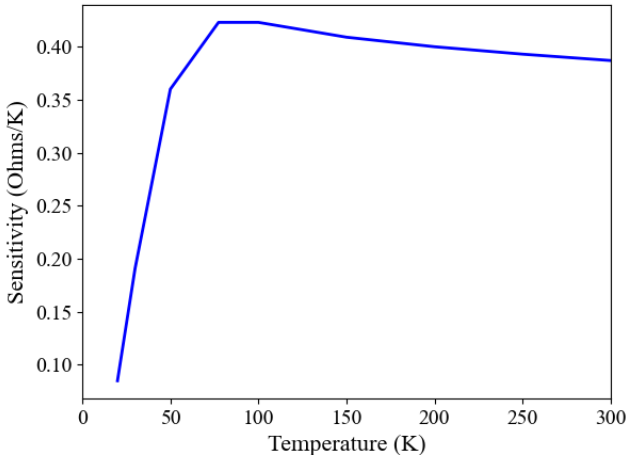


Figure 3.6.: Sensitivity of the PT-100 sensor dependent on its temperature [36].

Similarly to the diode-based sensor, the sensitivity of the platinum sensor is defined as the derivative of the calibration curve. The sensitivity of the platinum sensor dependent on its temperature is shown in Figure 3.6.

Figure 3.6 shows that the sensitivities of the platinum sensor are relatively larger at temperatures higher than 50 K. On the other hand, the sensor loses its sensitivity at temperatures lower than 14 K because its resistance approaches a constant value as temperature approaches zero. For this reason, the platinum sensors were utilized for relatively higher temperature regions of the thermal shields at 40 and 77 K and also the 77 K-current leads.

3.2. LTS Wiring of the Magnet in the Cryostat

The TGU includes two coils and each coil consists of the superconducting (SC) wires and a copper yoke [37]. The terminals of the TGU are low temperature SC (LTS) wires connected to the low temperature terminals of the HTS leads (2 terminals per coil). Soldered connections between the terminals and the LTS connecting cables are required.

In this section, the SC wiring and wire's support structures will be described in subsection 3.2.1. The cooling concepts employed conduct-cooled cylinders for transferring the heat from the soldering points of the SC wires to the LHe reservoir. These will be described in subsection 3.2.2. The connection methods of the SC wires will be described in subsection 3.2.3.

3.2.1. SC Wire Support Structures

The SC wires with an applied current induce a magnetic field, which can perturb the magnetic field of the TGU. In the first experiment, powering tests of a single TGU coil were performed, but the applied current could not be increased above 400 A due to

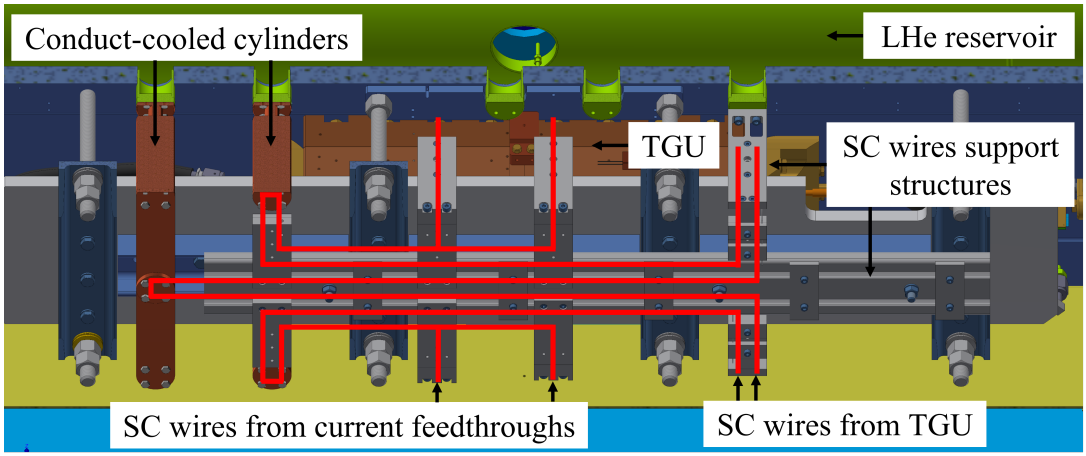


Figure 3.7.: A diagram explaining the guided SC wires and their own support structure [39].

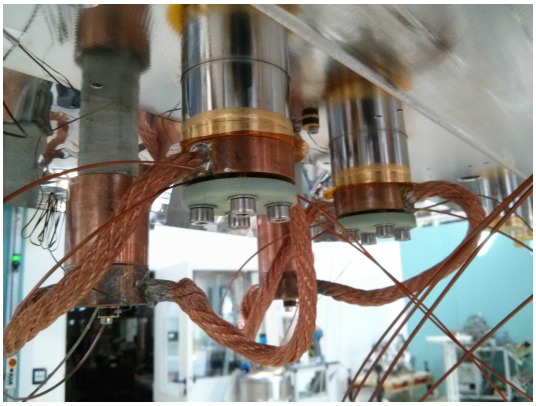


Figure 3.8.: A photograph of the cryostat current feedthroughs and their SC wires which will be connected to those coming out from the TGU.

premature quenches. Premature quenches can be attributed either to a degradation of the superconductor or to a mechanical instability of the SC wires, e.g. if parts of them are moved due to the Lorentz's force resulting in an energy release. [38].

In order to mitigate possible mechanical instabilities, a method to clamp and support the SC wires on their support structures was developed to minimize the magnetic perturbation and reach the operating current of 750 A.

In Figure 3.7, the SC wires from two coils are connected to the current feedthroughs in a series-circuit. They were clamped with flat aluminium structures and guided along the plane below the TGU to minimize the magnetic perturbation. Current flow directions of the SC wiring in this configuration is described in Figure 3.10 (b).

Figure 3.8 shows a photograph of the low temperature terminals of the HTS leads of the cryostat current feedthroughs. These terminals were connected to the terminals of the TGU.

In Figure 3.9, the SC wires from the terminals of HTS leads and the TGU were guided and clamped along the support structures. The wires were clamped to ensure that they

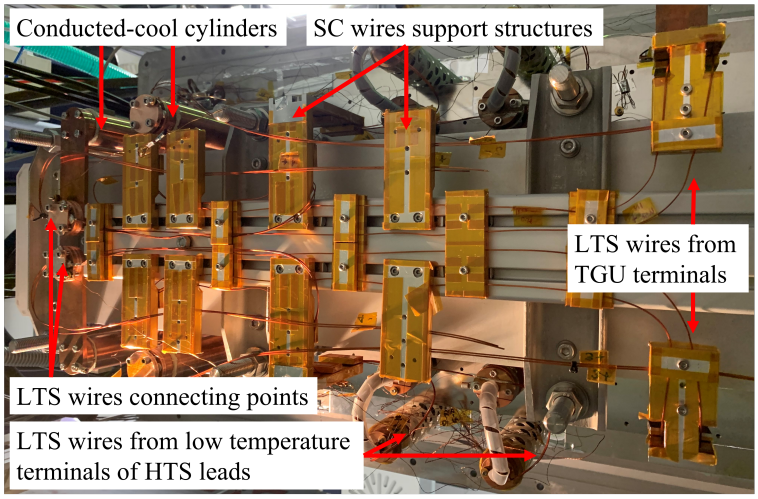


Figure 3.9.: Photograph showing the SC wires guided along their support structures to the connecting point.

were not displaced when the currents were applied, which could cause a quench [38]. Between the consecutive clamping positions, the SC wires have short spare lengths to avoid an over-tension force due to the thermal shrinking of the wire material during the temperature changes. In addition, a polyimide tape was attached on the surface of the aluminium support structure to a avoid short circuit (to ground) in case the thin insulation layer of the SC wire is damaged.

3.2.2. Conduct-cooled Cylinder

The soldering material used to connect the SC wires is a normal conductor and its resistance does not vanish at LHe temperature. This means that heat is generated at the soldering points while the current is applied to the SC wires. A temperature rise in the SC wires can degrade their stability in the superconducting state. Thus, special conduct-cooled cylinders were developed to allow an efficient heat transfer from the SC wire connecting point to the LHe reservoir.

Figure 3.10 shows the SC wiring between terminals of the TGU and HTS leads when both coils were connected in a parallel- and series-circuits, respectively. The black lines represent the LTS wires. The brown, gray and orange structures represent the TGU coils, the terminals of HTS leads and the conduct-cooled cylinders, respectively. Four and three conduct-cooled cylinders were used when the SC wires configurations were parallel- and series-circuits, respectively.

Figure 3.11 shows the conduct-cooled cylinder having 3 separated parts, which are made of oxygen-free copper. The uppermost part was attached to the LHe reservoir using four vacuum-type screws. The middle part was attached to the uppermost part using a non-conductive glue (Master Bond EP21TCHT-1) for establishing an electrical isolation between the cryostat and the entire TGU.

The heat can still be transferred through the glue. The lowermost part is the copper plate which is soldered with the SC wires. The lowermost part is simply attached to the

middle part using four vacuum-type screws. In addition, small indium sheets are attached on the contact surface of the uppermost and lowermost part to increase the heat transfer capability of the interfaces.

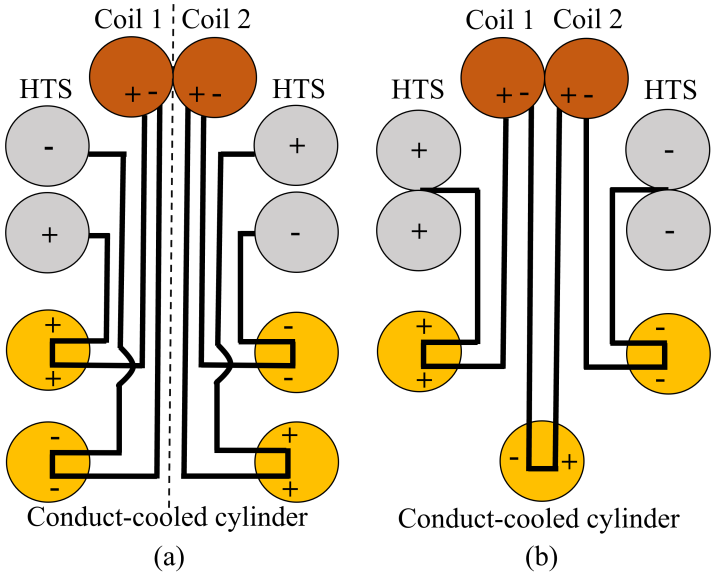


Figure 3.10.: Schematic diagrams of the SC wiring between terminals of the TGU and HTS leads when both coils were connected in (a) a parallel- and (b) series-circuits.

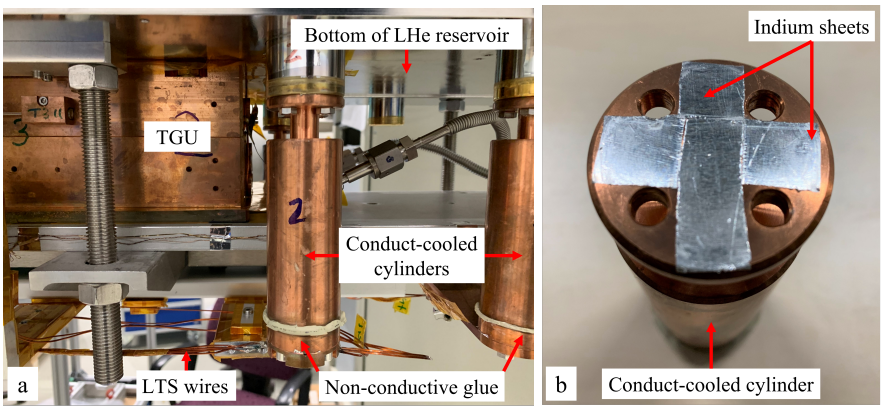


Figure 3.11.: (a) Conduct-cooled cylinder and (b) small indium sheets attached to the contact surface to increase the capability of the heat transfer.

3.2.3. SC Wire Soldering Method

Heat is generated at the connecting point of the SC wires due to the normal conducting soldering material. Thus, a low-resistance soldering material is required to connect the SC wires and to mount them on the copper plate. This plate is a part of the conduct-

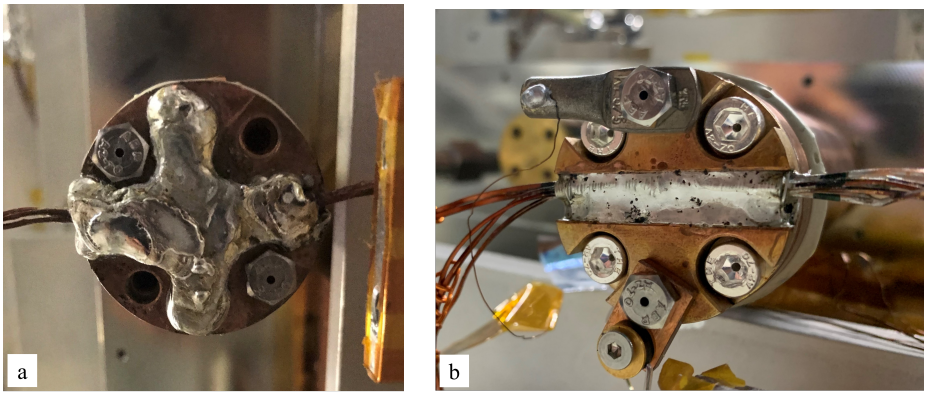


Figure 3.12.: (a) Original and (b) improved soldering methods for connecting the LTS wires.

cooled cylinder used for transferring the heat to the cold reservoir, described in the subsection 3.2.2.

For soldering the SC wires, the soldering material and the copper plate should be at identical temperature. Otherwise, the SC wires and the copper plate cannot be perfectly connected each other. Tension in the SC wires due to the thermal shrinking can destroy the connection to the copper plate. It causes a temperature rise and, consequently, the SC wires can behave as a normal conductor and be damaged as the temperature approaches the critical temperature. Moreover, the SC wires can be damaged if a high current is applied in normal conducting state.

Figure 3.12 shows the original and improved methods to solder the SC wires with the flat copper plate which is a part of the copper conduct-cooled cylinder. At the soldering positions on the SC wires for both methods, the insulation of the SC wires was removed by heating and polishing with a sand paper. Then, the bare terminal of the wires are tightly wrapped using a small normal conducting wire and then soldered with the copper plate.

Regarding the original solder shown in Figure 3.12 (a), the heating process was very difficult because the melted soldering material flowed to random directions. The melted material could only attach to the horizontal surface of the flat plate. Thus, the strength of the connection was relatively lower.

For the improved configuration shown in Figure 3.12 (b), the copper plate was designed to have a groove for containing the melted soldering material. The melted material could attach to the horizontal and vertical surfaces of the grooved plate and the mechanical stability was better than the original case. The soldering material, the wires and the copper plate can conveniently be maintained at the required temperature.

This wiring, cooling concept and soldering method contributed to the successful TGU experiments such as the investigation of the cool-down procedure, the magnetic powering tests and the magnetic characterization and the field measurement, which will be described in the following sections and chapters.

Table 3.3.: Properties of LN_2 and LHe [40, 41] at atmospheric pressure.

Parameter	Value	Unit
LN_2		
Melting Point	63.14	K
Boiling Point	77.36	K
Density (at 77.31 K)	806.8	$kg\,m^{-3}$
Specific heat capacity, C_p (at 77.31 K)	2.042	$kJ\,kg^{-1}\,K^{-1}$
Thermal conductivity (at 77.31 K)	133	$mW\,m^{-1}\,K^{-1}$
Specific latent heat of vaporization (at 77.36 K)	199	$kJ\,kg^{-1}$
LHe		
Melting Point	0.949	K
Boiling Point	4.224	K
Density (at 4.222 K)	142.9	$kg\,m^{-3}$
Specific heat capacity, C_p (at 4.222 K)	13.58	$kJ\,kg^{-1}\,K^{-1}$
Thermal conductivity (at 4.222 K)	18.7	$mW\,m^{-1}\,K^{-1}$
Specific latent heat of vaporization (at 4.224 K)	21	$kJ\,kg^{-1}$

3.3. TGU Cool-down Procedure

The TGU cool-down was done in two steps. It was initiated by using LN_2 to cool the LHe reservoir and TGU to around 100 K to 120 K. Subsequently, the LHe reservoir was repeatedly filled with LHe until its bottom plate and the TGU reached the operating temperature of 4.3 K to 4.4 K. The entire procedure will be described more detail in this section.

Cooling Background

Table 3.3 shows the properties of LN_2 and LHe. The density of LN_2 is $806.8\,kg\,m^{-3}$ at 77.31 K at atmospheric pressure and the specific latent heat of vaporization of LN_2 is $199\,kJ\,kg^{-1}$. In case of the LHe, the density and specific latent heat of vaporization are $142.9\,kg\,m^{-3}$ and $21\,kJ\,kg^{-1}$, respectively [41, 42]. When a liquid contacts a much warmer surface, the amount of vaporization energy can be evaluated by

$$Q_L = \rho V L, \tag{3.2}$$

where ρ is the density of the liquid, V is the volume of the evaporated liquid and L is the specific latent heat of vaporization of liquid.

At ambient temperature and a vacuum pressure in an order of 10 Pa, the TGU cool-down procedure was started by using a LN_2 because the specific latent heat of vaporization of the LN_2 at 77.36 K is much larger than that of the LHe at 4.224 K [41]. Therefore, the initial cool-down procedure using LN_2 has a higher efficiency than using the LHe.

The LN_2 and LHe reservoirs were cooled until they reached 77 K and 4 K, respectively. Then, nitrogen and helium can be liquid inside their own reservoirs. The 77 K- and 4 K-thermal shields were cooled by direct contact to the LN_2 and LHe reservoir, respectively. In case of the TGU, it was contact-cooled by the LHe reservoir and the LHe-cooled heat exchanger plates.

The heat is transferred from the thermal shields to the liquid reservoirs via a conduction process. A 1-dimensional conceptual analysis of the heat transfer between two objects can be started from Fourier's law of heat conduction,

$$\begin{aligned} Q_{cond} &= -kA\frac{dT}{dx} \\ q_{cond} &= -k\frac{dT}{dx}, \end{aligned} \tag{3.3}$$

where Q_{cond} is the heat transfer rate in W, k is the thermal conductivity of the material in $\mathrm{W\,m^{-1}\,K^{-1}}$, A is the area of the contacting surface, dT/dx is the temperature change per unit length (temperature gradient) and q_{cond} is the heat flux. In practice, heat flows from a high temperature area to a low temperature area in 3 dimensions. Then, Equation 3.3 is extended to

$$\vec{q}_{cond} = -k\left(\frac{\partial T}{\partial x}\hat{i} + \frac{\partial T}{\partial y}\hat{j} + \frac{\partial T}{\partial z}\hat{k}\right), \tag{3.4}$$

where $\vec{q}_{\mathrm{cond}}$ is a heat flux vector in 3 dimensions, the term in the bracket represents the gradient of the temperature distribution, $\hat{i}$, $\hat{j}$ and $\hat{k}$ are unit vectors in the x, y and z coordinate, respectively. Equation 3.4 can be written in a general form of Fourier's law as

$$\vec{q}_{cond} = -k\nabla T. \tag{3.5}$$

Equation 3.5 can only be applied if the temperature distribution is determined. For the TGU cryostat, it is complicated to determine the temperature distribution in its structure. However, it is clearly seen that the heat transfer rate by conduction is also determined by the temperature difference,

$$q_{cond} \propto (T_H - T_C), \tag{3.6}$$

where $\mathrm{T_H}$ is a temperature of the hot material and $\mathrm{T_C}$ is that of the cold one.

The 40 K-shield was not cooled by contact to the liquid reservoirs but by cold He vapour, which flows through a heat exchanger in contact with the shield. Inside the heat exchanger, the heat is transferred across the solid surface of the heat exchanger channel walls to the surrounding liquid or vapour that is a convection process and based on Newton's law of cooling. It can be described by

$$Q_{conv} = H_C A(T_H - T_C), \tag{3.7}$$

where Q_{conv} is the heat transfer rate in the convection process, H_{C} is the heat transferred per unit area per kelvin (heat transfer coefficient) in $\mathrm{W\,m^{-2}\,K^{-1}}$, T_{H} is the temperature of the solid surface and T_{C} is the temperature of the liquid. Equation 3.7 can be rewritten as the heat transfer rate per unit area, which is

$$q_{conv} = H_C(T_H - T_C), \tag{3.8}$$

where q_{conv} is the heat transfer rate per unit area or heat flux in $\mathrm{W\,m^{-2}}$. In practice, the heat transfer from the solid surface cooled by liquid cannot be described by a constant heat transfer coefficient. The heat transfer coefficient depends on the dynamics of the liquid, which is laminar or turbulent flow [43]. However, this dynamics was not taken into account in this point. It is clearly seen that the heat transfer rate by convection depends on the temperature difference,

$$q_{conv} \propto (T_H - T_C). \tag{3.9}$$

Both, heat transfer by convection and conduction are involved in transferring the heat from the initially warm cold mass inside the cryostat to the LN_2 and LHe. Then, the liquids carry the heat out of the cryostat by evaporation. As long as the liquids evaporate, the cooling power depends on the latent heat of evaporation and the evaporated volume of liquid.

Methodology for the cool-down

The LN_2 was filled using a small flowing ratio to the nitrogen reservoir until the LN_2 temperature was reached. To transport the LN_2 from the external storage to its reservoir inside the cryostat, an external pressure of 50 kPa was applied to the storage. It is necessary to fill the LN_2 reservoir using a small flowing ratio because the LN_2 evaporates immediately when it contacts the inner reservoir surface. This evaporation can cause an over pressure inside the LN_2 transferring system.

The first step of cool-down by the vaporization of the liquid was discussed at the previous, the second step could be described by a heat transfer to the cold vapor. After LN_2 evaporates, the heat is transferred to the cold vapor as long as the vapor flows in the LN_2 transferring system of the cryostat. The capability to bring the heat out of the system of the cold vapor is relative small with respect to the vaporization of LN_2. The specific heat capacity (C_p) of LN_2 at 77.31 is 2.042 $\mathrm{kJ\,kg^{-1}\,K^{-1}}$. This parameters decreases to 1.343 $\mathrm{kJ\,kg^{-1}\,K^{-1}}$, upon the phase transition to gaseous N_2 at 77.31 K [42].

After the phase transition to gaseous, the temperature of the cold vapor can be increased by a small heat transfer from the system due to a small heat capacity. This results an increasing of kinetic energy of the vapor. Eventually, this vapor will be released out of the LN_2 transferring system of the cryostat. Moreover, the capability to bring the heat out of the system of the cold vapor will be wasteful, if too much of LN_2 evaporate and this cold vapor is released due to the high pressure.

Around 0.07 $\mathrm{m^3}$ of LN_2 were used to cool the LN_2 reservoir to reach the LN_2 temperature at 77 K. From this point, liquid could be filled into the tank. After that, the 77 K-thermal shield, interfacing with the bottom of the LN_2 reservoir, was conduct-cooled. Around 0.05 $\mathrm{m^3}$ per 24 hours were required to sustain the temperature of the 77 K region at the LN_2 temperature. Therefore, the amount of transferred energy which vaporizes the LN_2, at 77.36 K, per 24 hours can be evaluated to

$$\begin{aligned} Q_L &= \rho V L \\ &= 806.8\ [\mathrm{kg\,m^{-3}}] \times 0.05\ [\mathrm{m^3}] \times 199 \times 10^3\ [\mathrm{J\,kg^{-1}}] \\ &\approx 8.028 \times 10^6\ \mathrm{J}. \end{aligned}$$

The amount of the energy transferred to the 77 K region per unit time can be evaluated to

$$\begin{aligned} q_L &= \frac{Q_L}{t} \\ &= \frac{8.028 \times 10^6}{24 \times 3,600}\frac{[\mathrm{J}]}{[\mathrm{s}]} \\ &= 92.9\ \mathrm{W}. \end{aligned} \tag{3.10}$$

Inside the cryostat there is a 10^{-6}-Pa vacuum. Therefore, the heat transfer to the 77 K region can mostly be attributed to radiation from the outermost thermal shield which is at ambient temperature and the heat transferred through the internal structure of the cryostat.

This consideration is a simplistic estimation, which assumes that the 77 K-thermal shield is surrounded by a very far away surrounding surface. Thus, a distance between two surface is very much larger than dimensions of the 77 K-thermal shield. A fact that this shield is wrapped by a multi-layer insulation and a reflectivity are not taken into account. The heat transfer rate per unit area by radiation can simplistically be evaluated by

$$\frac{Q_{rad}}{A} = \sigma\varepsilon(T_H^4 - T_C^4) \tag{3.11}$$

where σ is Stefan-Boltzmann constant, ε is emissivity coefficient of the surface of 77 K-thermal shield, T_H is a temperature of the outermost thermal shield and T_C is a temperature of the 77 K-thermal shield. The 77 K-thermal shield is made of an aluminized Mylar and its emissivity coefficient at 77 K is approximated 0.009 [44]. Then, the heat transfer rate per unit time an be evaluated by

$$\begin{aligned} \frac{Q_{rad}}{A} &= \sigma\varepsilon(T_H^4 - T_C^4) \\ &= 5.6704 \times 10^{-8}\ [\mathrm{W\,m^{-2}\,K^{-4}}] \times 0.009 \times (300^4 - 77^4)\ [\mathrm{K^4}] \\ &\approx 4.12\ \mathrm{W\,m^{-2}}. \end{aligned}$$

The evaluated heat transfer rate per unit time is $4.12\,\mathrm{W\,m^{-2}}$. If the total area of the surface of the 77 K-thermal thermal shield is approximated to the order of $2.50\,\mathrm{m^2}$, the heat transfer rate per unit time becomes 10.3 W. This evaluated value does not correspond to the order of the energy transferred to the 77 K region per unit time described above.

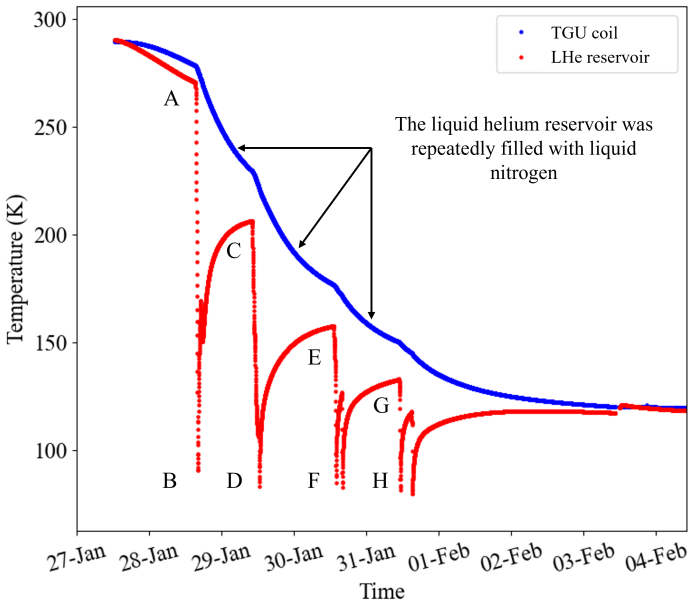


Figure 3.13.: Temperatures of the TGU and a bottom of LHe reservoir, which is a cold reservoir, during cool-down procedure using the liquid nitrogen.

Thus, the heat transfer cannot mainly be attributed to radiation from the outermost shield. The heat conduction by the internal structures of the cryostat and cables for temperature sensors as well as the heat transferred to LN_2 reservoir needs to be considered.

Figure 3.13 shows temperatures of the TGU and at the bottom plate of the LHe reservoir during the cool-down procedure using LN_2. The LN_2 filling was started at point A. The LN_2 filling was suspended when the temperature of the bottom of LHe reservoir was close to 80 K, at point B, and it was restarted when the temperature of the bottom of the LHe reservoir had risen to the order of 200 K at point C and was suspend again at point D. This procedure was used to maximise the amount of heat transferred from the TGU to the LHe reservoir and then to the LN_2, which depends on the difference between the LHe reservoir and the LN_2 temperature, as described by Equation 3.9. This cool-down procedure was continued until the TGU temperature was around 100 K to 120 K.

For the fillings starting at point E and G which the temperature differences with respect to the filling end points F and H are smaller than for the two previous fillings. Therefore, also the LN_2 filling times were shorter. Moreover, the differences between the TGU and the LN_2 temperature are smaller. Combining these two conditions, the capability to reduce the TGU temperature decreases. In order to reach 4 K, the further cool-down procedure used LHe.

During the LN_2 filling, it was taken care that the temperature of the bottom of the LHe reservoir stayed above 80 K to avoid condensation of the LN_2 inside the helium system. For the following step, warm helium gas was filled into the helium system to flush the remaining nitrogen gas. An additional vacuum pump was installed to bring the mixture of gases out of the helium system. These two steps were repeated to ensure there is no

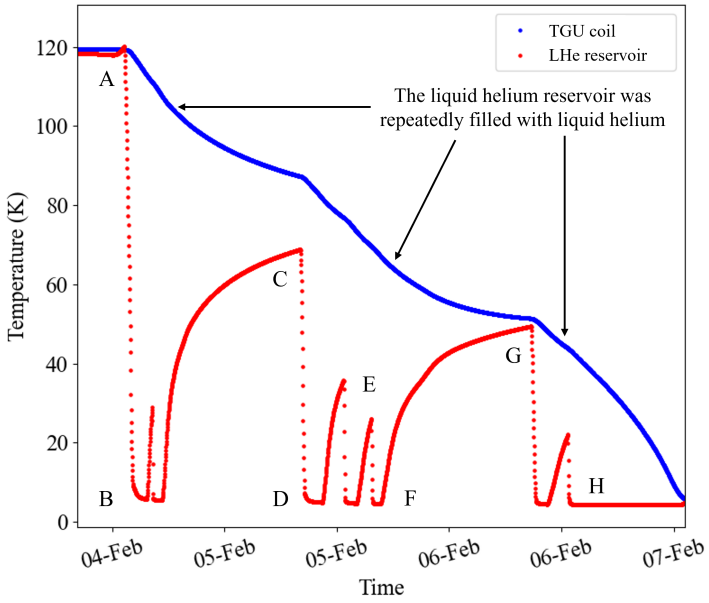


Figure 3.14.: Temperatures of the TGU and a bottom of LHe reservoir, which is a cold reservoir, during cool-down procedure using the liquid helium.

remaining nitrogen gas, which could condense and freeze inside the helium system during the cool-down with LHe.

Figure 3.14 shows the temperatures of the TGU and at the bottom of the LHe reservoir during the cool-down procedure using the LHe. External helium gas with a pressure of 25 to 30 kPa and a flow rate of 2×10^{-3} m^3 per minute was applied to the LHe dewar in order to transport the LHe to its reservoir inside the cryostat. At temperatures above 4.2 K, the LHe was repeatedly filled into the LHe reservoir with a small flow rate for similar reasons, as discussed for the LN_2 filling.

In Figure 3.14, the LHe filling was started at point A and it was suspended at point B. At point B, the temperature of the bottom of LHe reservoir was still higher than the LHe temperature. There were two LHe fillings in the period between points A and C. The TGU temperature rapidly decreased because a large amount of heat could be transferred from the TGU to the LHe reservoir due to the large temperature gradient, as described in Equation 3.6.

In Figure 3.14, when there was no LHe inside the reservoir, its temperature rose from point B to point C. In the meantime, the TGU temperature continued to decrease because its heat was transferred to the bottom of LHe reservoir. The LHe filling was started again at point C and was suspended at point D. At lower temperature, the TGU temperature decreased with a smaller ratio due to the smaller temperature gradient between the TGU and the bottom of the LHe reservoir. The LHe filling was repeated for another two times in this second period between points D, E and F.

Figure 3.15 shows temperatures of the TGU, the bottom of the LHe reservoir and the heat exchanger plates at the final step of the cool-down procedure using LHe. The LHe reservoir was filled again at point G and the filling was continued until it reached the LHe

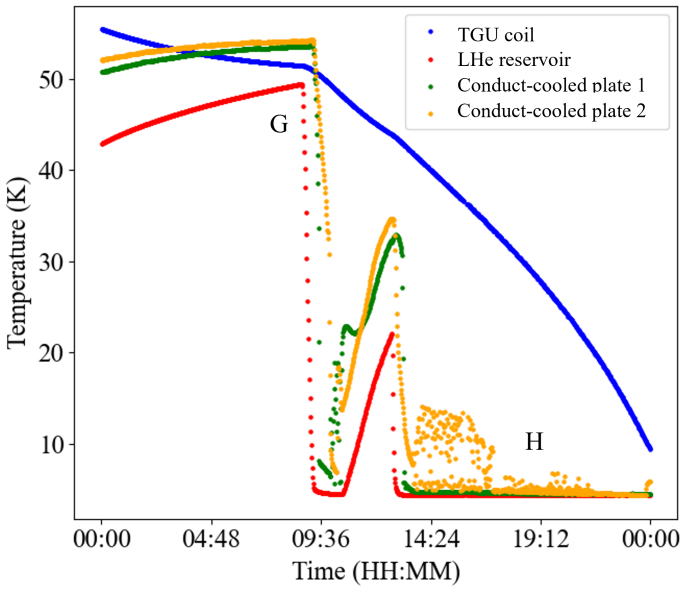


Figure 3.15.: Temperatures of the TGU, the bottom of LHe reservoir and conduct-cooled plates at a final step of the cool-down procedure using the LHe.

temperature at point H. At this point, the LHe could be stored inside the reservoir and flows through the heat exchanger plates below the TGU, as shown in Figure 3.1. In this condition, heat can be transferred to both the bottom of the LHe reservoir and the heat exchanger plates. From point G at around 50 K, the TGU temperature decreases to 4.3 K to 4.4 K in 15 hours.

Around 0.3 m^3 of LHe were used in this step. In addition, the evaporated helium from the LHe reservoir flows through the heat exchanger plate, which contacts to the 40 K-thermal shield. Therefore, the temperature of this shield was reduced to 20 K. After the TGU reached the LHe temperature, it was necessary to sustain the LHe temperature to allow all components to reach an equilibrium state. This is a preparation for the magnet powering tests, which will be described in the following section. Around 0.05 m^3 (per 15 hours) of LHe were used to sustain the TGU as LHe temperature at the zero-current condition. The vaporization energy per unit time in this case can be evaluated by using Equation 3.2 together with the density (ρ) [42] and the specific latent heat of vaporization (L) [41] of LHe at 4.222 K at atmospheric pressure. The amount of energy transferred to the 4 K region per unit time is evaluated to

$$\begin{aligned}\frac{Q_L}{t} &= \frac{\rho V L}{t} \\ &= \frac{142.9\ [\mathrm{kg\,m^{-3}}] \times 0.05\ [\mathrm{m^3}] \times 21 \times 10^3\ [\mathrm{J/kg}]}{15 \times 3600\ [\mathrm{s}]} \\ &= 2.78\ \mathrm{W}.\end{aligned}$$

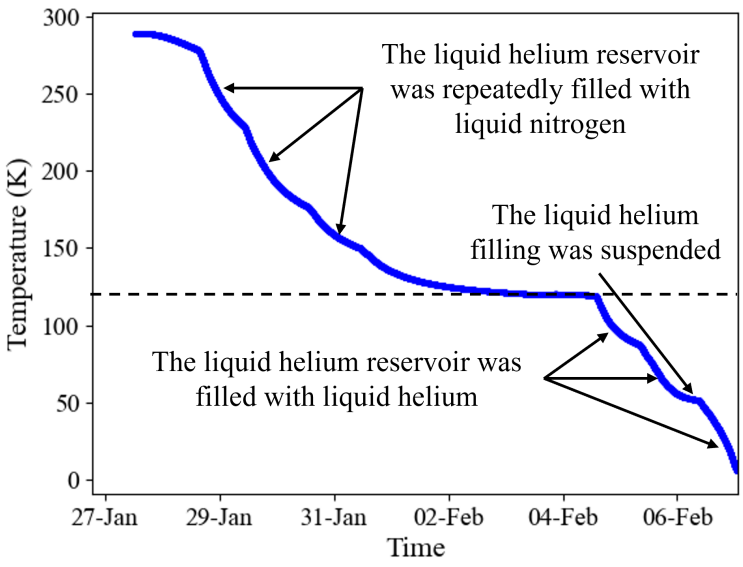


Figure 3.16.: TGU temperature during the entire cool-down procedure.

Inside of the 10^{-6}-Pa vacuum condition, the heat transfer to this region is attributed to heat radiation from the surrounding thermal shield at 20 K. The 4 K-thermal shield is made of a polished aluminium and its emissivity coefficient at 4 K is approximated to 0.05 [44]. The heat transfer rate per unit area via the radiation process can be evaluated by using Equation 3.11,

$$\begin{aligned}\frac{Q_{rad}}{A} &= \sigma\varepsilon(T_H^4 - T_C^4) \\ &= 5.6704 \times 10^{-8}\ [\mathrm{W\,m^{-2}\,K^{-4}}] \times 0.05 \times (20^4 - 4.4^4)\ [\mathrm{K^4}] \\ &\approx 4.53 \times 10^{-4}\ \mathrm{W\,m^{-2}}.\end{aligned}$$

The evaluated heat transfer rate per unit time is 4.53×10^{-4} W m^{-2}. If the total area of the surface of the 4 K-thermal shield plus LHe reservoir is approximated to 1.5 m^3, the heat transfer rate per unit time becomes 6.79×10^{-4} W. Similar to the 77 K-shield, the heat transport cannot mainly be attributed to radiation from the 20 K shield. The entire heat transfer via the conduction through the cryostat structures and via the convection through opening slits, for the sliding part of the magnetic field measurement system, on the 40 K- and 77 K-shields need to be considered.

Figure 3.16 summarizes the TGU temperature during the entire cool-down procedure using both LN_2 and LHe. The TGU temperature slowly decreases at the beginning of the cool-down procedure while the LN_2 reservoir was cooled using LN_2. In the following section, the temperature rapidly decreases while the LHe reservoir was repeatedly cooled using the LN_2 because the flat-top surface of the TGU support structure directly contacts the bottom of the LHe reservoir.

The LN_2 filling was repeated until the TGU reached around 120 K to avoid condensation of LN_2 inside the LHe system and to ensure that all filled LN_2 was evaporated. The remaining nitrogen gas in the LHe reservoir was flushed out using warm helium gas.

Subsequently, the LHe reservoir was repeatedly filled with LHe until it reached the LHe temperature and LHe could flow through the conduct-cooled plates below the TGU. Both cold reservoirs contributed to the cool-down procedure and the TGU reached the LHe temperature at 4.3 K to 4.4 K. The entire procedure consumed 9 days. At zero-current condition, the cryostat efficiency could sustain the TGU at LHe temperature for 15 hours until all LHe inside the reservoir is evaporated.

3.4. TGU powering tests

In the previous section, the TGU cool-down procedure to the operating temperature of 4.5 K was described. This section describes the powering tests for investigating the optimum operating method of the TGU. The tests were also preparations for the magnetic characterization of the TGU.

The TGU was designed to produce a transverse magnetic field of 1 T at the central axis, when it is operated with a current of 750 A. The TGU operating must to avoid approaching the critical condition of the SC wire which is defined by its temperature, self-field and current density. Thus, the operating temperature must be sufficiently low to enable a safe operation of the TGU in self field well at the current of 750 A. This means a sufficient temperature margin is required for powering the TGU because the critical current at self-field is a function of temperature.

There are various possible electrical connection schemes to perform the TGU powering tests such as powering tests using single coils and two coils in series. The powering tests of a single coil will be described in subsection 3.4.3. For the powering tests using two coils, more details will be provided in subsection 3.4.4.

3.4.1. Current supply and quench protection equipment

A current supply used in the TGU powering tests and operations is a direct current (DC) power supply of O.C.E.M Power Electric company. The specifications of the current supply are shown in Table 3.4. The TGU cryostat has four external current feedthroughs connected to four power lines coming from the current source.

Table 3.4.: Specifications of the current supply used for the TGU powering tests and operations.

Output Parameter	Value	Unit
Current	0-1,200	Ampere (DC)
Voltage	±2	Volt
Accuracy	$\pm 10^{-4}$	

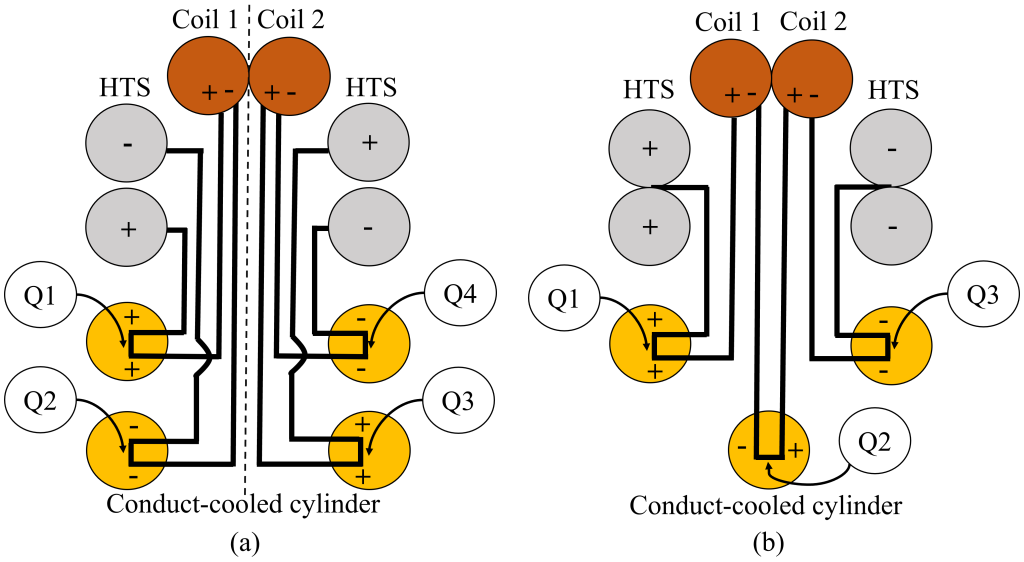


Figure 3.17.: Schematic diagrams show positions of the voltage taps (Q1 to Q4) for quench detection in powering tests of (a) a single coil and (b) two coils.

In the powering tests of a single coil, two current feedthroughs on one side of the cryostat were used for positive and negative current lines of a single coil. The other two feedthroughs on the opposite side were used for the other coil. In the first scheme, each coil was alternatively powered. For the second scheme, both coils were simultaneously powered in a parallel-circuit without an interconnection. In the powering tests using two coils, it is possible to use two current feedthroughs on one side of the cryostat for the positive current lines and the other two on the opposite side for the negative current lines for both coils.

During the powering tests and TGU operations, it is required to monitor the voltage of the SC wires to detect a possible quench. Voltages of the SC wire when it reaches the superconducting stage are in order of a few hundred microvolts because its resistance is zero. On the other hand, the SC wire behaves as a normal conductor and has a finite resistance when a quench occurs. Applying high currents while the SC wire behaves as a normal conductor generates a large amount of heat and causes an overheat and a possible destruction of the wire.

Therefore, additional measuring wires are attached at various connection points of the SC wires aiming to measure the voltage of each section of the SC wires, especially the TGU coil, during the powering tests and other experiments. If the detector monitors improper voltages of the SC wires due to a quench, the current supply is immediately suspended. For example, the quench voltage limit of the TGU coil is defined as 50 mV when the applied voltage of the current supply is 1 V.

Figure 3.17 shows positions of the voltage taps for measuring the voltage of the circuit for quench detection. The voltage taps are attached at 4 K connection points of the HTS leads and the connection points between the TGU wires and the LTS connecting wires. However, this figure represents only positions of voltage taps for the LTS parts of the TGU.

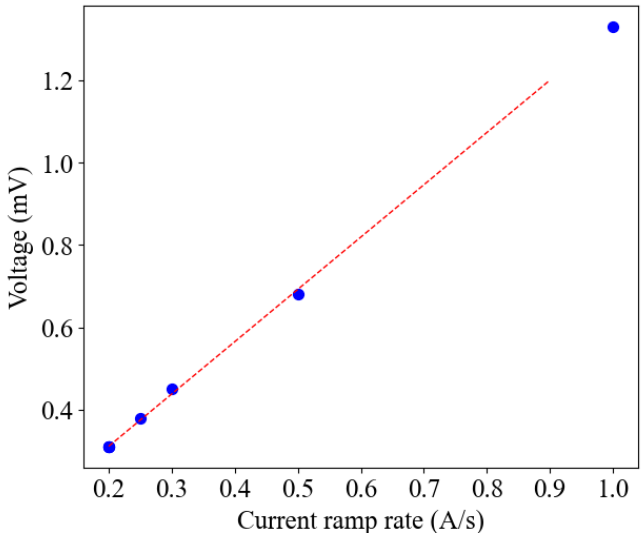


Figure 3.18.: Voltage drop across a complete LTS parts of a single TGU coil as a function of the current ramp rate.

When each TGU coil was alternatively powered, Figure 3.17 (a), a pair of voltage tap Q1 and Q2 and a pair Q3 and Q4 were used to measure the voltage across the complete LTS part of coil 1 and coil 2, respectively. When both coils were connected in series-circuit, Figure 3.17 (b), the voltage tap Q1 and Q3 were used to measure the voltage across the complete LTS parts of both coils and the voltage across the alternative coil could be measured using Q2.

When the quench occurs, the stored electromagnetic energy of the TGU is conversed into heat. If this heat could uniformly be transferred through the TGU winding, it would rarely be a trouble [45]. The stored energy is given by

$$E_{\text{stored}} = \frac{1}{2} L I^2, \tag{3.12}$$

where L is an inductance of the magnet and I is the applied current of magnet. The inductance can be evaluated from the voltage drop across a complete LTS part of a single TGU during the magnetic powering tests. The voltage drop can be represented in terms of the inductance and the current ramp rate (dI/dt) by

$$V\ [\text{mV}] = L\ [\text{mH}]\ \frac{dI}{dt}\ [\text{A s}^{-1}], \tag{3.13}$$

Figure 3.18 shows the measured voltage drop across the complete LTS part of a single TGU as a function of the current ramp rate during the powering test. This voltage drop can be described by

$$V\ [\text{mV}] = 1.269 \times \frac{dI}{dt}\ [\text{A s}^{-1}] + 0.0578. \tag{3.14}$$

In this consideration, the inductance of the complete LTS part of a single coil is 1.269 mH. In the TGU operation using two coils connected in series, evaluations of the total inductance

of the complete LTS parts of both TGU coils and the stored energy are required for a consideration of the quench protection scheme. The total inductance (L_{Total}) is given by

$$L_{\text{Total}} = L_{\text{coil1}} + L_{\text{coil2}}, \tag{3.15}$$

where L_{coil1} and L_{coil2} are the inductance of the complete LTS parts of the coil 1 and coil2, respectively. Thus, th total inductance is 2.539 mH. Eventually, the stored energy of two TGU coils connected in series-circuit, when the current of 750 A is applied, can be evaluated by Equation 3.12,

$$\begin{aligned} E_{\text{stored}} &= \frac{1}{2}\, 2.539\ [\text{mH}]\ \times\ 750^2\ [\text{A}^2] \\ &\approx 714\ \text{J}. \end{aligned}$$

In the TGU experiments, there is no a bypass circuit for magnet protection in case a quench is detected because the stored energy of the TGU is small.

3.4.2. Eddy current heating

Considering the two TGU coils shown in Figure 2.5, each coil consists of 40 magnetic periods and each period consists of two short SC coils. The coil former consists of copper and is enclosed by the SC wire of n layers with N turns each. The relative permeability (μ_r) of the coil former equals to 1 because it is made of non-magnetic material. The neighbouring coils generate fields of opposite direction. Thus, large fractions of the generated fields at the center of the enclosed area of the coil cancel out. If this fact is neglected, the magnitude of the magnetic field at the center of the enclosed area of the coil for each short coil can be approximated by

$$B = \frac{\mu_0 nNI}{L}, \tag{3.16}$$

where μ_0 is the magnetic permeability of free space, L is the length of the coil and I is the applied current. An example photograph of a 2-period TGU short model explaining the SC coils, two cylindrical coil former and support structures is shown in Figure 3.19.

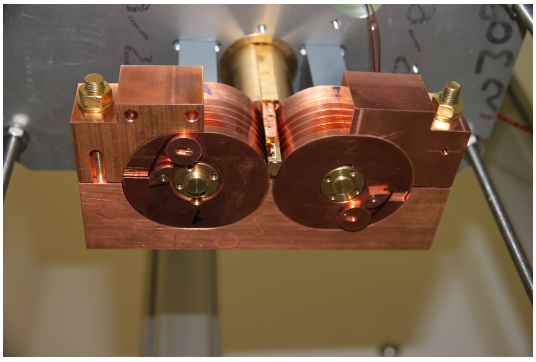


Figure 3.19.: Photograph of 2-period TGU explaining the SC coils, two cylindrical coil former and rectangular support structures [12].

Table 3.5.: Parameters used for the simplistic estimation of heat generated by the eddy current from the short SC coil.

Parameter	**Value**	**Unit**
Number of SC wire layer (n)	6	layer
Number of SC wire turn per layer (N)	4	turn
Material of coil former	OFHC copper	
Estimated temperature of coil former (T)	4.2	K
Resistivity of OFHC copper at 4.2 K [47] (ρ)	$\approx 10^{-10}$	Ω m
Radius of coil former (r)	30	mm
Length of coil former (L)	5.25	mm
Rate of change of applied current (dI/dt)	1	A s^{-1}

The observed thermal behaviour during the powering tests can be attributed to the eddy current heating. An increasing or a decreasing of superconducting coil current causes a change in magnetic flux, which gives rise to induced currents in the copper coil former. These induced currents decay slowly due to the high conductivity of the material at LHe temperature. The cylindrical copper coil former shown in Figure 3.19 is the main source for the eddy current heating. The intensity of the eddy current [46] is given by

$$I_e = -\frac{1}{R}\frac{d\phi_B}{dt} \qquad \text{and} \qquad \phi_B = \vec{B} \cdot \vec{A}, \tag{3.17}$$

where R is the coil former resistance, $\vec{B}$ is the magnetic flux density and $\vec{A}$ is the area enclosed by the superconducting (SC) wire.

In reality, there is an induced electric field when the magnetic flux change which resulting in a current density distribution in the copper coil former. The heat generated due to this current density distribution need to be integrated together with heat generated due to the eddy current. For simplistic treatment, the heat generated by the eddy current from each short section of the SC coil is given by

$$P = I_e^2 R. \tag{3.18}$$

Combining Equation 3.16 and Equation 3.17, example of the heat generated by the eddy current at the center of this short SC coil can simplistically be evaluated by the follows. Table 3.5 show parameters used for the simplistic estimation of heat generated by the eddy current from the short SC coil. The former of this SC coil is made of oxygen-free-high-conductivity (OFHC) copper. At 4.2 K, the current of 100 A is applied to this SC coil. Then, the applied current is increased to 200 A within 100 s. Thus, the intensity of the the eddy current becomes

$$I_e = \frac{\mu_0 n N A}{RL}\frac{dI}{dt},$$

where $R = \rho L/A$. Resistivity (ρ) value of the OFHC copper former is approximated to the order of 10^{-10} Ω m. Inserting I_e into Equation 3.18, the heat generated by the eddy current from each short SC coil for this current ramping step can be estimated by

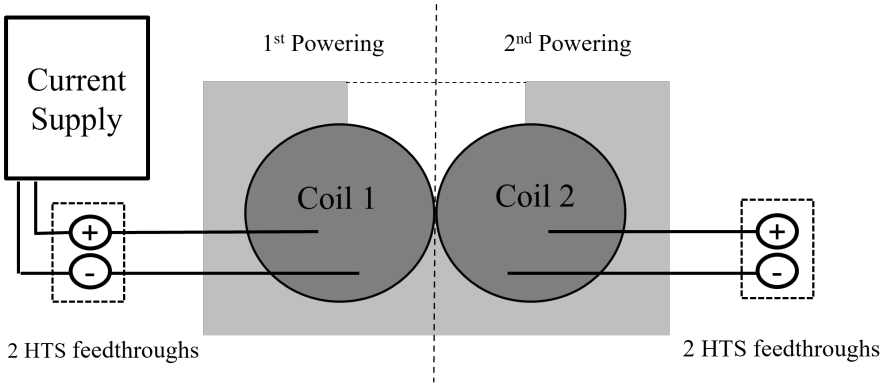


Figure 3.20.: Diagram explaining electrical connections of the TGU coils when each coil is powered separately [39].

$$P = \frac{1}{\rho}\left(\frac{\mu_0 n N d I}{dt}\right)^2 \left(\frac{A}{L}\right)^3$$

$$P = \frac{\left(1.2566 \times 10^{-6}\ [\mathrm{V\,s\,A^{-1}\,m^{-1}}]\ \times\ 6\ \times\ 4\ \times 1\ [\mathrm{A\,s^{-1}}]\right)^2 \left(\pi\ \times\ 0.03^2\ [\mathrm{m^2}]\right)^3}{1 \times 10^{-10}\ [\Omega\,\mathrm{m}]\ \left(5.25 \times 10^{-3}\ [\mathrm{m}]\right)^3}$$

$$\approx 1.42\ \mathrm{W}.$$

3.4.3. Powering tests using a single TGU coil

In the first configuration, each single coil of the TGU was separately powered. Two SC current feedthroughs on each side of the cryostat were used for each powering test. One of them is for positive current lines and the other is for negative current lines. The SC wires coming from the current feedthroughs and from the TGU were connected using the soldering to a flat copper plate described in subsection 3.2.3, which is the original method shown in the Figure 3.12 (a).

A diagram explaining electrical connections for powering tests in the first configurations is shown in Figure 3.20. The operational limit of the SC current feedthroughs is 600 A. Therefore, the maximum current used in the first powering configuration was 600 A. The TGU temperature at zero-current state was 4.7 K in this configuration.

In the powering tests, it was required to increase the the current in steps and to allow the cryostat to reduce the TGU temperature back to 4.7 K to avoid reaching the critical temperature of the superconducting coil. Applying currents up to 600 A using increasing rates of 0.5 , 1.0 and 2.0 $\mathrm{A\,s^{-1}}$ were successful. Each TGU coil achieved a stable operation at 600 A.

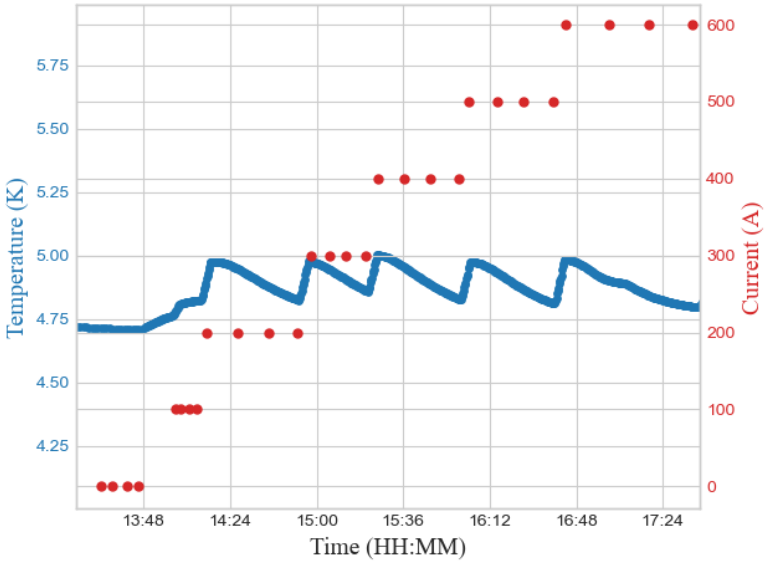


Figure 3.21.: Thermal behaviour of the TGU during powering test of a single coil using a current ramp rate of 0.5 A s^{-1} when the applied current was normally increased [39].

Figure 3.21 shows operating current (red dots) and temperature of the TGU coil (blue dots) as a function of time during ramping the current in several steps using a ramp rate of 0.5 A s^{-1}. The powering test started when the TGU temperature was 4.675 K at the zero-current state. Then, the current was increased to 100 A. The TGU temperature slowly increased to around 4.76 K and remained almost constant when the TGU reached the steady state and the induced current decayed.

After that, the current was increased to 200 A and the TGU temperature rapidly increased to 4.934 K. At constant current, the TGU temperature slowly decreased to around 4.765 K in 40 minutes. This procedure was repeated for the following current values until the applied current reached 600 A and the cryostat reduced the TGU temperature to around 4.77 K again.

It is clearly seen that the TGU temperature rises to around 4.9 K to 5.0 K, which is well below the critical temperature of the SC material. The thermal behaviour is similar in each ramp step because the current change is 100 A with a ramp rate of 0.5 A s^{-1} for each ramp step. The entire procedure consumed approximately 4 hours starting from the zero-current stage to the operating current one and the subsequent temperature reduction to around 4.77 K.

Figure 3.22 shows current and TGU coil temperature during a stepwise ramp with 2.0 A s^{-1}, up to a quench. The TGU temperature was around 4.653 K at the zero-current stage. The powering procedure was similar to the powering test using the ramp rate of 0.5 A s^{-1}. At 100 A, the TGU temperature was constant at 4.775 K. The results show that TGU temperature rose to around 5.2 K after the currents were constant at 200 A, 300 A and 400 A.

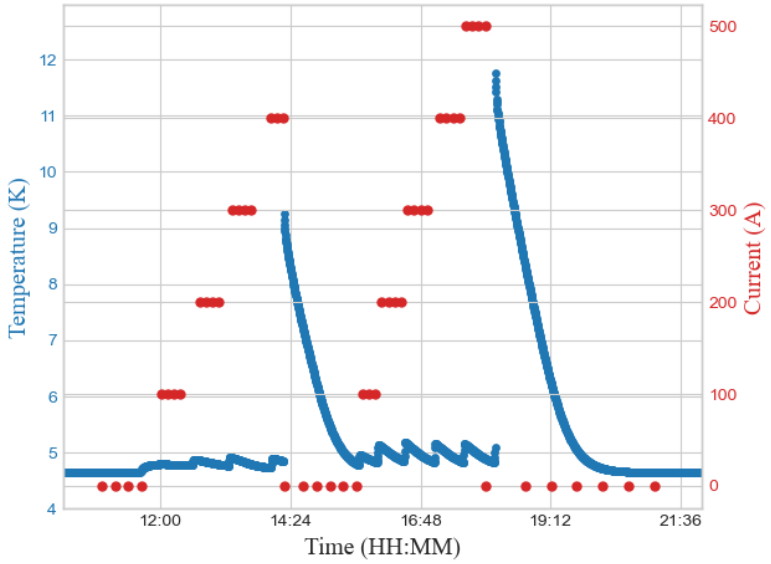


Figure 3.22.: Thermal behaviour of the TGU during powering test of a single coil using a current ramp rate of 2.0 A s^{-1} when the applied current was immediately suspended [39].

However, the current supply was immediately suspended due to a quench while the applied current was constant at 400 A, leading to an increase of the temperature. The applied current was immediately changed from 400 A to zero. This change causes a large change in magnetic flux density in the copper coil former. From the relationships Equation 3.17 and Equation 3.18, a large amount of heat was generated causing a rise of TGU temperature to 9.5 K.

The temperature was reduced back to 4.8 K in one hour. After that, the entire procedure was repeated to reach an applied current of 600 A. This time, a quench occurred during the ramp from 500 A to 600 A. A large amount of heat was generated, which caused a rise of TGU temperature to around 11.8 K. At the zero-current stage, the cryostat could reduce the TGU temperature from 11.8 K to 4.7 K in two hours.

During the powering tests in this configuration, the rise of the TGU temperature, the cooling efficiency of the cryostat and the total time consumed for the entire ramping were investigated. This information was applied to improve the ramping schemes for the series-connected TGU coils to achieve an appropriate powering method.

3.4.4. Powering tests using two TGU coils in series

For the second configuration, both TGU coils were connected together using a series-circuit connection of the LTS wires. Two current feedthroughs of the cryostat were occupied for the positive-current lines and the other two for the negative-current lines of the current supply, each pair connected in parallel. In this configuration, the possible maximum current becomes 1200 A.

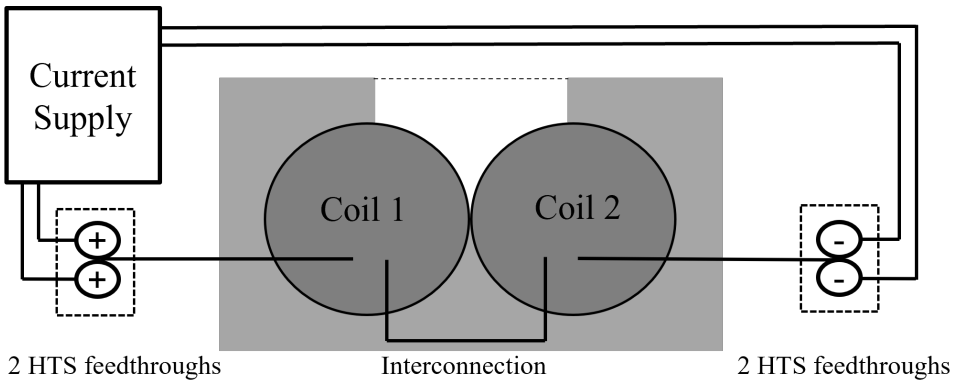


Figure 3.23.: Diagram explaining the electrical connections of the TGU coils when both coils are connected in series and powered together.

The positive-current SC wire of the coil number one is connected to the pair of positive-current feedthroughs and its negative-current SC wire is done to the positive-current SC wire of the coil number two. Then, the negative-current SC wire of the coil number two is connected to the pair of negative-current feedthroughs. A diagram to explain the electrical connections for powering tests in the second configuration is shown in Figure 3.23.

The TGU temperature in zero-current condition was 4.4 K for this configuration. It is assumed that the heat due to the eddy currents during ramping must be twice as large as compared to the test using a single coil. Therefore, at the beginning of the tests, the current was increased in steps to allow the cryostat to reduce the TGU temperature back to 4.4 K.

In addition, the results of the previous powering tests had shown that a quench had a larger probability to occur when a large ramp rate was used. Considering the two reasons above, ramp rates of 0.2, 0.25, 0.3, 0.5 and 1.0 A s^{-1} were used in the initial tests to overcome the current value of 600 A and to reach the operating current of 750 A.

Figure 3.24 shows temperatures of both TGU coils during a stepwise current ramp to 700 A using a current ramp rate of 0.5 A s^{-1} and the quench occurs more than half an hour after the ramp (holding quench). This phenomenon might be explained by the temporal behaviour observed in the magnetic field measurements, which is named a slow asymptotic increase of the current in the superconductor after the ramp.

In Figure 3.24, the applied current could overcome the previous limit of 600 A. When the applied current was increased in several steps from 0 A to 600 A, the TGU thermal behaviour showed that the rise in TGU Temperature, for each ramping step, did not reach the critical temperature of the SC material. From 0 A to 400 A, the temperature decreased back to 4.4 K. After the ramping to 500 A, the temperature base level increased to 4.5 K after each step. In the following step, a quench occurred immediately after the current ramping to 700 A was completed.

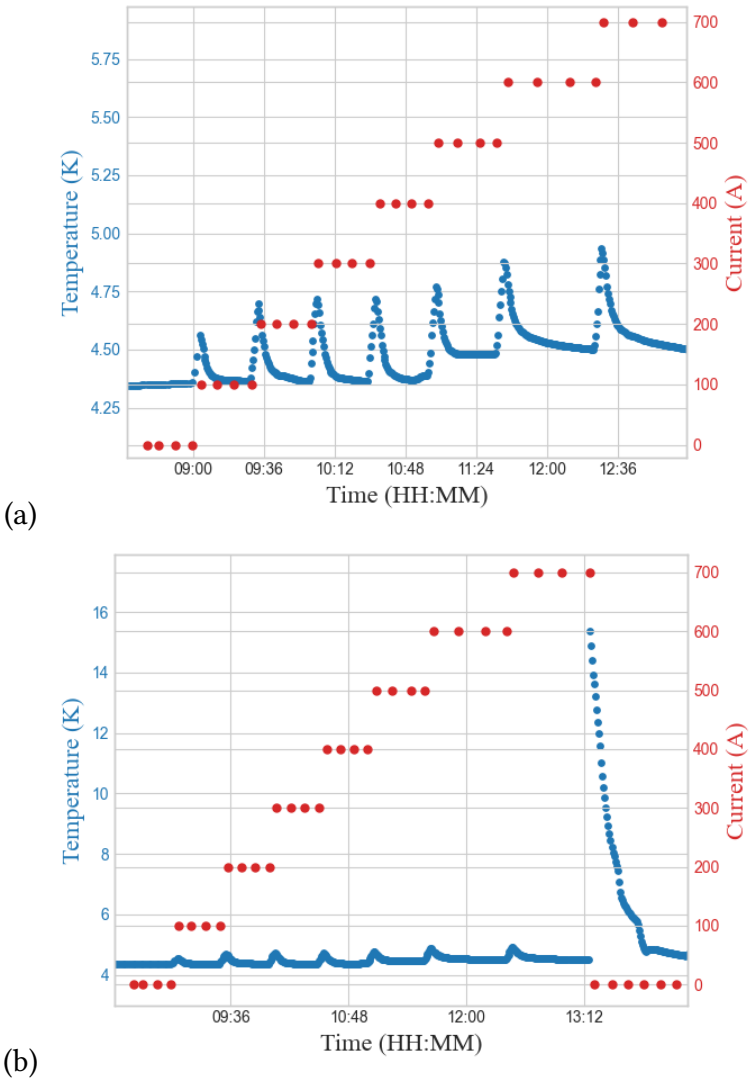


Figure 3.24.: Powering test of two TGU coils using a current ramp rate of 0.5 A s^{-1} when (a) the current was normally increased and (b) quench after the same ramp.

A possible reason for the quench at a higher current is, the first quench caused by a slight motion of the certain part of the wire due to the change of the Lorentz force. Then, that certain part of the wire moves to a stable position after the first quench, the TGU coil can be powered to a higher current afterwards. The following quench can then be caused by the motion of another part of the TGU winding at the higher applied current. [38].

Figure 3.25 shows the temperature of two TGU coils when a current ramp rate is 1.0 A s^{-1}. In this powering test, TGU temperature at the zero-current stage was 4.471 K. The applied current was increased in several steps from 0 A to 800 A, However, the ramping step size was reduced when the applied current was higher than 700 A to reduce the probability for a quench. This powering test could overcome the TGU operating current of 750 A. A quench occurred after the ramping from 775 A to 800 A was just finished.

Considering the two examples of powering tests where the current was increased in several steps, it is clearly seen that the entire procedure consumes a time of around 3

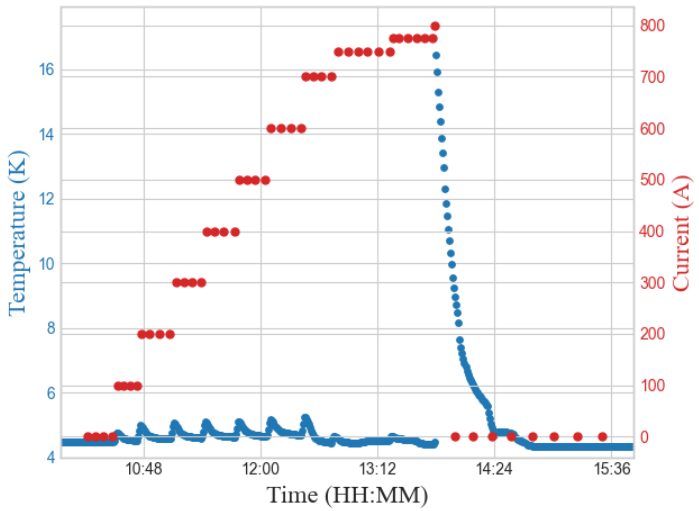


Figure 3.25.: Thermal behaviour of the two TGU coils while the applied current increases in several steps using a current ramp rate of 1.0 A s^{-1}.

hours to reach the operating current and to cool the TGU back to 4.5 K. This method is not convenient for the upcoming step to investigate the quench limit of the TGU at high current values because it is necessary to start the entire powering procedure again from zero-current stage at 4.5 K several times after the quench.

Therefore, a current ramping to the operating current in a single step or a few steps using rather small ramp rates was investigated. A smaller ramp rate was used to ensure that the TGU temperature stays well below critical conditions. Figure 3.26 shows the TGU temperature during a single-step ramping from zero to operating current with a ramp rate of 0.2 A s^{-1}. The TGU temperature rose from 4.352 K at the zero-current state to around 4.737 K when the TGU reached the operating current of 750 A after 1 hour and 13 minutes. Then, the TGU temperature decreases back to 4.337 K in 1 hour without the quench.

Beside the ramp rate of 0.2 A s^{-1}, a single-step ramping using ramp rates of 0.1, 0.25 and 0.3 A s^{-1} was investigated to find the optimum powering condition for the TGU to reach the operating current of 750 A. For example, the ramp rate of 0.3 A s^{-1} was used to ramp from 0 to 750 A and the result showed that the TGU temperature rose from 4.392 K, zero-current state, to around 5.390 K and then the quench occured while the applied current was around 740 A. This is because TGU temperature is approaching the critical temperature of the SC wire material at the given applied current and the resulting self-field.

On the way to reach the operating current, quenches occurred several times under several current ramping conditions and even at a constant current of 750 A. Therefore, the ramping method was changed to increase the current to a certain current value, such as 700 A, in a single step and then to increase the current in several further small steps aiming to reach the TGU operating current of 750 A and the quench limit at 900 A. This is to minimize the probability of triggering a quench at high current levels. Examples of powering test using this procedure are shown in Figure 3.27.

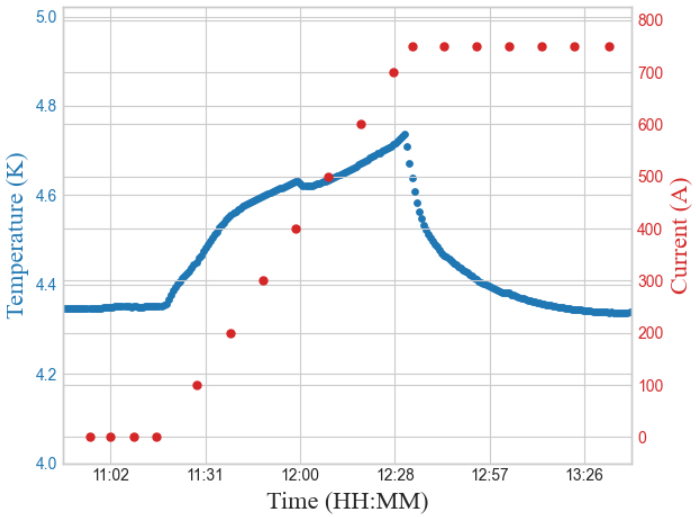


Figure 3.26.: The TGU temperature during a single-step ramping to operating current of 750 A using a ramp rate of 0.2 A s^{-1}.

In the ramp shown in Figure 3.27, the applied current continuously increased to 700 A in a single step using the ramp rate of 0.2 A s^{-1}. This step consumed a time of around 1 hour and 10 minutes and the TGU temperature rose from 4.389 K to 4.935 K. After the TGU temperature was reduced to 4.507 K, the ramping step size was reduced to 25 A per step and the powering was continued using a ramp rate of 0.2 A s^{-1}. For this ramping step size, the changes in the TGU temperatures were in the order of 0.05 K to 0.1 K. Eventually, the TGU reached 750 A with an associated temperature of 4.452 A in 5 minutes after the current was constant.

After reaching the operating current, the powering test was continued to reach 900 A. However, the current supply was suspended due to a quench during ramping from 850 to 875 A, while the applied current was 856 A and the TGU temperature was 4.491 K. The TGU temperature immediately rose to around 17 K and the cryostat could reduce the TGU temperature back to 4.375 K in 30 minutes.

Combining the powering test results from both, current ramping in several steps and in a single step, in order to reach the TGU operating current and to study the quench limit, relationships between the TGU temperatures, applied current values and current ramp rates were investigated. The accumulated results of this study are shown in Figure 3.28.

Figure 3.28 shows the applied currents of the TGU, at which the quenches occurred, as a function of the current ramp rates. The several-step ramping using a ramp rate of 0.5 A s^{-1} has a large probability for quenches at low current values before reaching the TGU operating current. For the single-step ramping to operating current, it is required to use a ramp rate smaller than 0.3 A s^{-1} to avoid reaching the critical temperature of the SC wire material. After the TGU reaches its operating current, further increasing the applied current above 800 A strongly increases the probability for a quench because the current level approaches the TGU quench current limit.

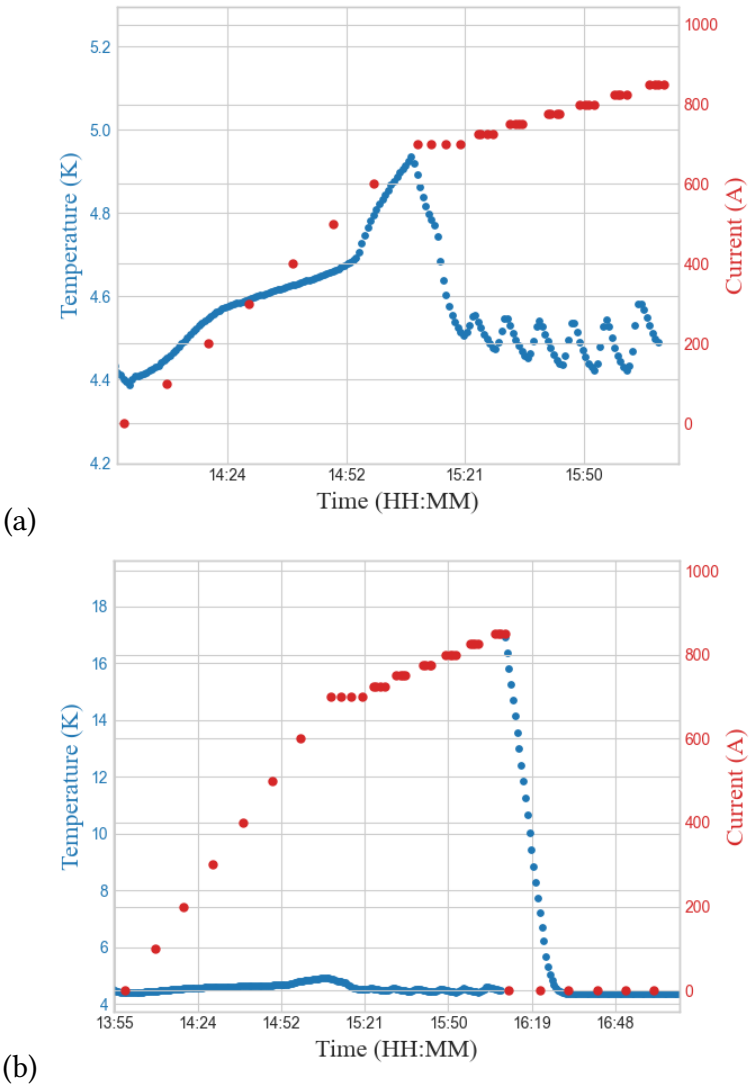


Figure 3.27.: Powering test of two TGU coils (a) reaching 850 A using a current ramp rate 0.2 A s^{-1} and (b) when the quench immediately occurs.

Figure 3.29 shows the quench history. The quench current steadily increased as a function of quench number. After the TGU coils overcame the current limit of a single current feedthrough as 600 A, the first quench occurs when applied current was 700 A and the following quenches occured at higher applied currents. Finally, the TGU reached the operating current of 750 A and could be powered up to 850 A. This is both due to a training effect and to the optimisation of the ramping scheme.

It is clearly seen that the current ramping to the operating current or a certain current nearby in a single step is more appropriate than the several-step ramping. In addition, it is necessary to use ramp rates smaller than 0.3 A s^{-1} in a single-step ramping to avoid reaching the critical temperature of the SC wire material.

To conclude, powering tests using each single TGU coil and both coils were performed in order to accumulate significant information such as the rise of the TGU temperature during

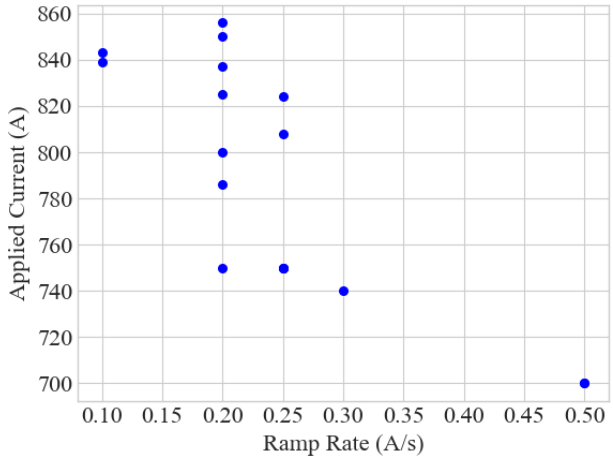


Figure 3.28.: Quench dependency on the current ramp rate of the applied current of the TGU.

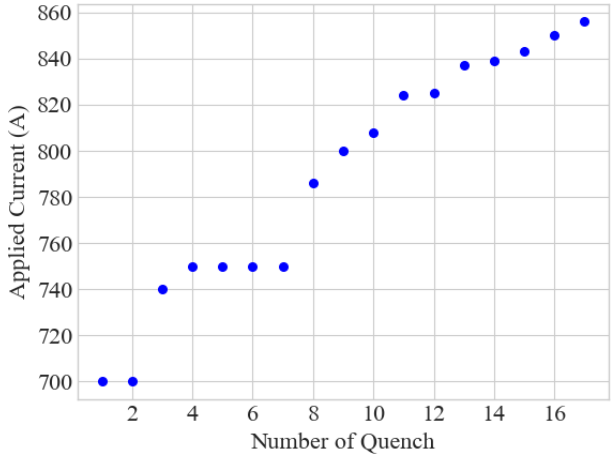


Figure 3.29.: Quench numbers with respect to the applied current of the TGU.

current ramping, the cooling capability of the cryostat and the total time consumed for the ramping from zero current state to the maximum possible current. The TGU reached its operating current of 750 A and the maximum stable current was 850 A.

This experienced information was applied in order to achieve an appropriate powering method and an optimum TGU operating procedure for the magnetic characterization, which will be described in the following chapter.

4. Magnetic Field Measurements of the TGU

The magnetic field measurements of the TGU were performed in the TGU's own cryostat described in detail in chapter 3. In this chapter, the method of the magnetic field measurement, the experimental setup and the measurement results are presented and discussed.

4.1. Methodology

4.1.1. Hall Effect

The transverse magnetic field in the TGU was measured via a longitudinal scan using 1-D Hall probes. The working principle of a Hall probe is based on the Hall effect, which is a phenomenon that occurs in current-carrying elements with a magnetic field. When a current is applied to the Hall probe placed in a magnetic field, a Hall voltage is induced in the direction perpendicular to both the current and the magnetic field component [48, 49]. The current-carrying elements are usually formed on semiconductor plates. A diagram explaining the Hall effect is shown in Figure 4.1.

The operating current $\vec{I}$ (current density $\vec{J}$) flows in y-direction of the plate and the measured magnetic field component $B_\perp$ is perpendicular to the plate. In case that no magnetic field is present, the electrons travel in y-direction, parallel to the longitudinal electric field $\vec{E}_e$. The electrons with velocity $\vec{v}_\mathrm{n}$ move by the Lorenz force:

$$\vec{F}_L = e\ (\vec{E}_e + \vec{v_n}\ \times\ \vec{B}), \tag{4.1}$$

where e is the elementary charges. Due to the magnetic force, the electrons are pushed to one side of the semiconductor plate. Consequently, the density of electrons on the opposite side decreases and an electric field E_H is generated between the two sides of the plate. E_H obeys the equilibrium condition of

$$\vec{E_\mathrm{H}} + \vec{v_n}\ \times\ \vec{B} = 0 \tag{4.2}$$

and gives rise to a measurable transverse voltage, the Hall voltage V_H, which is produced between two edges of the Hall sensor. The Hall voltage is given by

$$V_\mathrm{H} = \int_{S1}^{S2} \vec{E_\mathrm{H}} \cdot d\vec{l}, \tag{4.3}$$

where the integration path is a distance between two electrodes along the width of the plate. The electron velocity is related to the electron mobility μ_n and the external electric field $\vec{E}_e$ by

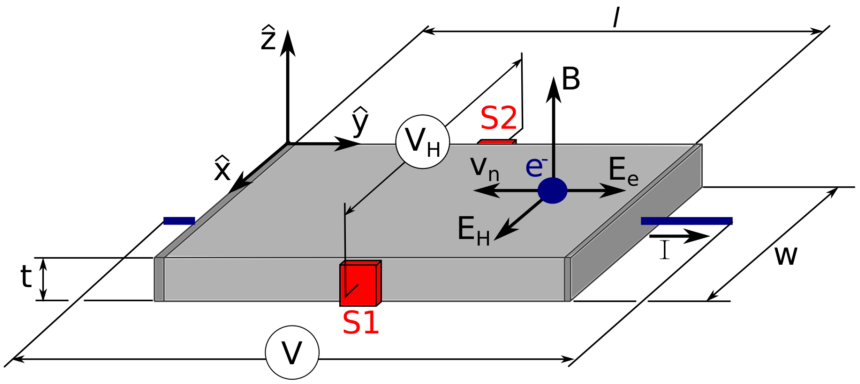


Figure 4.1.: Diagram explaining the working principle of the Hall probe which consists of a thin semiconductor plate with length l, width w and thickness t [12].

$$\vec{v_n} = -\mu_n \vec{E_e}. \tag{4.4}$$

On the other hand, the current density, $\vec{J}$ is related to the external electric field by Ohm's law:

$$\vec{J} = \sigma \vec{E_e}, \tag{4.5}$$

where J is related to the applied current I and a cross-sectional area of the current-carrier plate by $J = I/tw$. The conductivity σ of the current-carrier plate is expressed by

$$\sigma = ne\mu_n, \tag{4.6}$$

where n is the electron density. Therefore, the current density becomes

$$\vec{J} = ne\mu_n \vec{E_e} = -ne\vec{v_n}. \tag{4.7}$$

Using Equation 4.2 and Equation 4.7, the V_H can be expressed as

$$\begin{aligned} V_\mathrm{H} &= \int_{S1}^{S2} \vec{E}_\mathrm{H} \cdot \vec{dl} = -\frac{J}{ne} B_\perp w, \\ V_\mathrm{H} &= \frac{R_\mathrm{H}}{t} I B_\perp \end{aligned} \tag{4.8}$$

where R_H is the Hall coefficient defined by $-1/ne$ [49].

4.1.2. Calibration of the Hall Probe

The magnetosensitivity of the Hall probe determines the response of the Hall voltage perpendicular to the magnetic field. The absolute sensitivity S, related to the transverse magnetic flux density $B_\perp$ and the measured V_H can be described by

Table 4.1.: Sensitivity of the Hall probe array (M7-TH5) at 77 K with the nominal control current of 10 mA and estimated errors.

Hall probe	**1**	**2**	**3**	**4**	**5**	**6**	**7**
S_{77K} [mV T^{-1}]	51.6	51.9	57.7	52.2	51.7	52.3	51.9
Estimated error [%]	3.88	3.85	3.47	3.83	3.87	3.82	3.85

$$S = \frac{V_{\mathrm{H}}}{B_{\perp}} = \frac{R_{\mathrm{H}} I}{t}. \tag{4.9}$$

It is necessary to calibrate the Hall probe before starting the magnetic field measurement. Firstly, the output voltage of each Hall probe when the applied current was zero was taken. This voltage is so-called the offset voltage (V_{off}) caused by the intrinsic properties of the Hall probe due to the manufacturing process without magnetic field. The possible cause of the offset voltage is a structural asymmetry of the active area of the Hall probe such as geometry errors, contact resistance, nonuniform doping density in the semiconductor and misalignment of the sensing electrode.

The offset voltage changes with time and was therefore recorded repeatedly before each Hall probe scan. The Hall voltage V_{H} in Equation 4.9 was then taken to be the measured Voltage ($\bar{V}_{\mathrm{H}}$) minus the offset voltage ($\bar{V}_{\mathrm{off}}$). Subsequently, the perpendicular magnetic field measured at the Hall probe was evaluated by [48]

$$B_{\perp}[\mathrm{T}] = \frac{\bar{V}_{\mathrm{H}}[\mathrm{mV}] - \bar{V}_{\mathrm{off}}[\mathrm{mV}]}{S_{4.2\mathrm{K}}[\mathrm{mV\,T^{-1}}]}, \tag{4.10}$$

where $\bar{V}_{\mathrm{H}}$ is the mean value of a Hall voltage, $\bar{V}_{\mathrm{off}}$ is that of an offset voltage measured at the Hall probe when the TGU current is zero, and $S_{4.2\mathrm{K}}$ is the sensitivity of the Hall probe at 4.2 K.

Unfortunately, the calibration data for 4.2 K of the Hall probe array was not available, which might cause an calibration error. This unknown difference can add a systematic error to the measurement results such as the evaluation of the transverse field gradient. It will be estimated and discussed in the following subsection.

It was reported that the sensitivity values at 4.2 K of the similar Hall probe array are smaller than those at 77 K around 2 mV T^{-1} [12]. Therefore, each sensitivity value of the probes at 4.2 K was estimated to be smaller than that at 77 K by 2 mV T^{-1}. It was also informed by the manufacturer that the mean linearity and sensitivity errors with respect to the magnetic field were less than 0.5 %, respectively. The sensitivities of the seven Hall probes at 77 K with the nominal operating current of I =10 mA and the estimated errors of the sensitivities due to the temperature are listed in Table 4.1.

4.1.3. Error Analysis of the Magnetic Field Measurement

The error propagation of the statistical errors of the measured quantities V_{H} and V_{off} yields for the standard deviation of the perpendicular magnetic field:

$$\sigma_{B_\perp} = \sqrt{\left(\frac{\partial B_\perp}{\partial \bar{V}_\mathrm{H}}\right)^2 (\sigma_{\bar{V}_\mathrm{H}})^2 + \left(\frac{\partial B_\perp}{\partial \bar{V}_\mathrm{off}}\right)^2 (\sigma_{\bar{V}_\mathrm{off}})^2}, \tag{4.11}$$

where $\sigma_{\bar{V}_\mathrm{H}}$ and $\sigma_{\bar{V}_\mathrm{off}}$ are the standard deviations of the measured Hall voltage and offset voltage, respectively. Each term of $\partial \mathrm{B}_\perp / \partial \bar{V}_\mathrm{H}$ and $\partial \mathrm{B}_\perp / \partial \bar{V}_\mathrm{off}$ can be evaluated by

$$\frac{\partial B_\perp}{\partial \bar{V}_\mathrm{H}} = \frac{\partial}{\partial \bar{V}_\mathrm{H}} \left(\frac{\bar{V}_\mathrm{H} - \bar{V}_\mathrm{off}}{S_{4.2\mathrm{K}}}\right) = \frac{1}{S_{4.2\mathrm{K}}}$$

and

$$\frac{\partial B_\perp}{\partial \bar{V}_\mathrm{off}} = \frac{\partial}{\partial \bar{V}_\mathrm{off}} \left(\frac{\bar{V}_\mathrm{H} - \bar{V}_\mathrm{off}}{S_{4.2\mathrm{K}}}\right) = -\frac{1}{S_{4.2\mathrm{K}}}.$$

The terms can replace the partial derivative terms in Equation 4.11 and the $\mathrm{S}_{4.2\mathrm{K}}$ is taken as the unknown sensitivity at 4.2 K. The standard deviation of $B_\perp$ can be evaluated by

$$\sigma_{B_\perp} = \frac{1}{S_{4.2\mathrm{K}}} \sqrt{(\sigma_{\bar{V}_\mathrm{H}})^2 + (\sigma_{\bar{V}_\mathrm{off}})^2}. \tag{4.12}$$

Beside the statistical error due to the measurement, the systematic error $\Delta_{B_\perp,S}$ due to the sensitivity of the Hall probe array is given by

$$\Delta_{B_\perp,S} = \frac{\partial B_\perp}{\partial S} \left(\Delta_S + \Delta_T\right), \tag{4.13}$$

where Δ_S is the mean systematic sensitivity error by the manufacturing which equals to 1.0 % of $\mathrm{S}_{4.2\mathrm{K}}$ and Δ_T is the additional systematic error due to the temperature dependence of sensitivity which is approximated to 3.89 % of $\mathrm{S}_{4.2\mathrm{K}}$. The term, $\partial \mathrm{B}_\perp / \partial \mathrm{S}$ is the partial derivative of the transverse field $\mathrm{B}_\perp$ related to the Hall probe sensitivity, which can be evaluated by

$$\frac{\partial B_\perp}{\partial S} = \frac{\partial}{\partial S} \left(\frac{\bar{V}_\mathrm{H} - \bar{V}_\mathrm{off}}{S_{4.2\mathrm{K}}}\right) = \frac{\bar{V}_\mathrm{off} - \bar{V}_\mathrm{H}}{{S_{4.2\mathrm{K}}}^2}.$$

Replacing the partial derivative term and linearity and sensitivity errors in Equation 4.13, the systematic error can be represented by

$$\Delta_{B_\perp,S} = \left(\frac{\bar{V}_\mathrm{off} - \bar{V}_\mathrm{H}}{{S_{4.2\mathrm{K}}}^2}\right) (0.0489\, S_{4.2\mathrm{K}}). \tag{4.14}$$

Moreover, $\Delta_{B_\perp,P}$ is systematic error due to the misalignment of the hall probe. With combining the mean values, the standard deviations of the measurement and the systematic error, the transverse magnetic field can be evaluated by

$$B_\perp = \bar{B}_\perp + (\sigma_{B_\perp} + \Delta_{B_\perp,S} + \Delta_{B_\perp,P}), \tag{4.15}$$

where $\bar{B}_\perp$ is the measured field. The magnetic flux density was evaluated by using the sensitivity value at 77 K, then, the flux density at 4 K must be larger. Thus, the deviation of the measured field has only one direction.

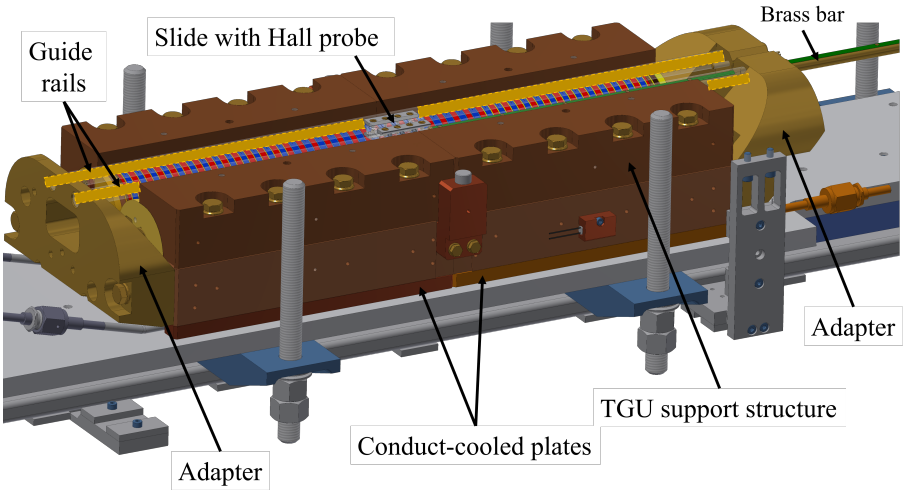


Figure 4.2.: Diagram of the magnetic field measurement system with the TGU [50].

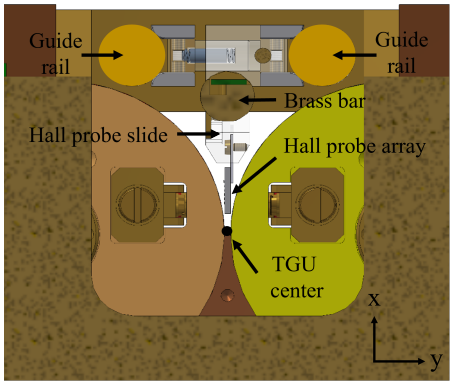


Figure 4.3.: 2-D cross-sectional view in the transverse plane showing a position of the slide with 7-Hall probe array [50].

4.2. Experimental Setup

4.2.1. Magnetic Field Measurement System

The field measurement system is operated by a longitudinal sliding apparatus attached to the TGU. This slide is carrying an array of seven Hall probes placed at equidistant transverse positions and is moved by a magnetically coupled linear translation unit operating at room temperature.

Figure 4.2 shows a diagram of the sliding system working at cryogenic temperatures. Two brass adapters were attached to both ends of the TGU. Then, two cylindrical guide rails were bolted to one adaptor and inserted into the opposite one. Using this assembly, the rails can slide with avoiding the mechanical stress due to different thermal expansions of the TGU support structure and the guide rails. The slide with the Hall probe array is pushed or pulled through the TGU gap by a brass bar bolted to the slide and passes through the adaptors.

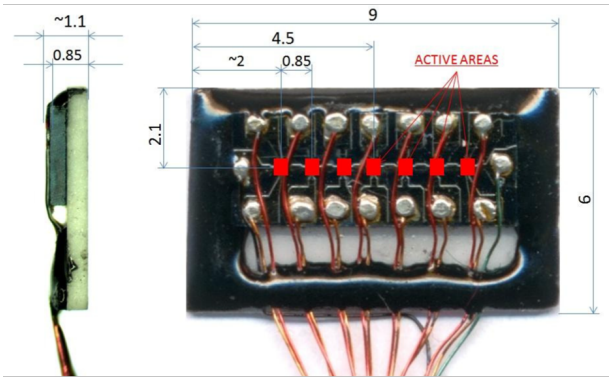


Figure 4.4.: Dimensions of the 7-Hall probe array (M7-TH5) in a unit of mm [12, 51].

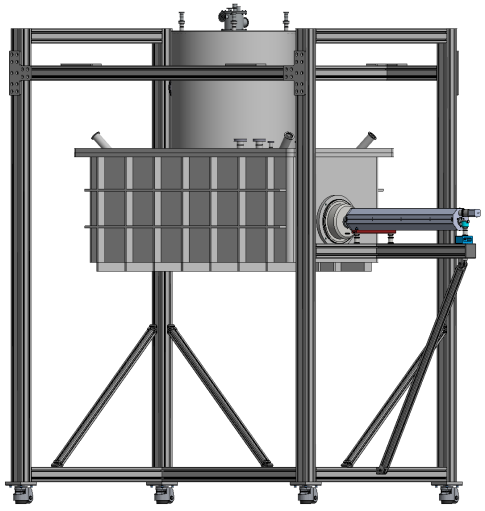


Figure 4.5.: Diagram of the linear translation unit coupled with the TGU cryostat.

Figure 4.3 shows a diagram explaining the position of the 7-Hall probe array between the two cylindrical magnetic poles of the TGU. The sliding system enables the Hall probes to record a two dimensional (2-D) field map by scanning in the longitudinal direction of the TGU.

Figure 4.4 shows photographs of the Hall probe array manufactured by AREPOC s.r.o, Slovakia. The probes were connected in series for a common supplied current of 10 mA. The array with seven Hall probes has a dimension of 9 mm × 6 mm × 1.1 mm (height, width, and thickness, respectively). The effective area of each probe has a dimension of 100 µm × 100 µm. The probes were aligned along a straight line with an equidistant spacing of 0.85 mm. This configuration enables the probes to simultaneously measure the magnetic fields in different transverse positions.

Figure 4.5 shows the linear translation unit operating at room temperature. The translation unit was installed to the outermost thermal shield of the cryostat. The aforementioned brass cylindrical bar operating at cryogenic temperature was then connected to the translation unit operating at ambient temperature with a polyetheretherketone (PEEK) coupling

to suppress the heat flow into the system. The brass bar was magnetically coupled with the translation unit under the identical vacuum in the cryostat. Refurbishment and installation of the entire magnetic field measurement system are described in subsection 4.2.3.

4.2.2. Misalignment of Hall probe array

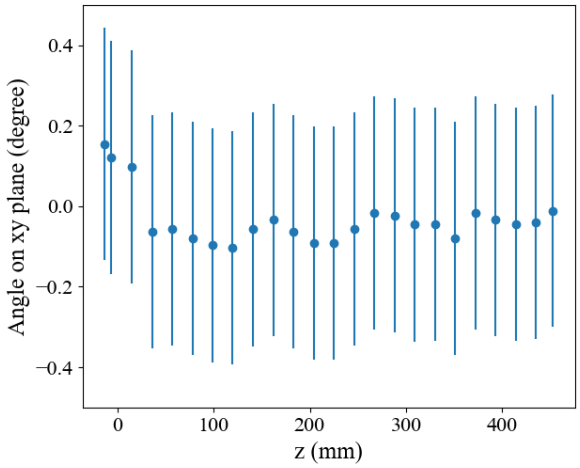


Figure 4.6.: Angles of the central vertical axis of the Hall probe array with respect to the xy-plane in the TGU coordinate system.

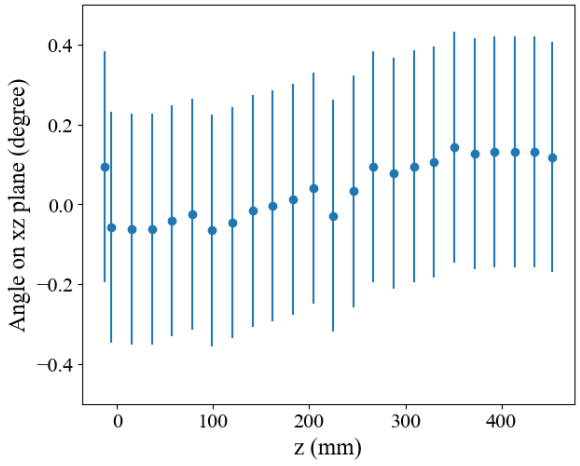


Figure 4.7.: Angles of the central vertical axis of the Hall probe array with respect to the xz-plane in the TGU coordinate system.

The mechanical structure of the Hall probe slide, shown in Figure 4.2, creates a force to the brass guide rails in transverse direction. Parts of the guide rails can be locally displaced due to their flexibility when the Hall probe slide moves along two guide rails. The displacements effect on the position and angle of the slide can also lead to a misalignment

of the Hall probes. Therefore, it is necessary to clarify the misalignment of the Hall probes to understand how much it is related to the systematic error of the measured magnetic field. The misalignment error of the Hall probe positions can be investigated by measuring the coordinates of the Hall probe slide because the Hall probes have the fixed positions with respect to the slide.

The coordinate measurement was performed at ambient temperature. The slide without Hall probe was longitudinally moved between the two cylindrical guide rails along the TGU gap. A portable 3-D coordinate measurement device, FARO Arm®, was employed to record the positions of the slide in a reference coordinate system with respect to the TGU. The angles of the slide were evaluated from the recorded positions during the movement.

Figure 4.6 and Figure 4.7 show the angle variations with the error bars of the vertical axis of the Hall probe array with respect to the xy- and xz-planes, respectively, in the TGU coordinate system. The x- and y-axes represent the vertical and horizontal directions, respectively.

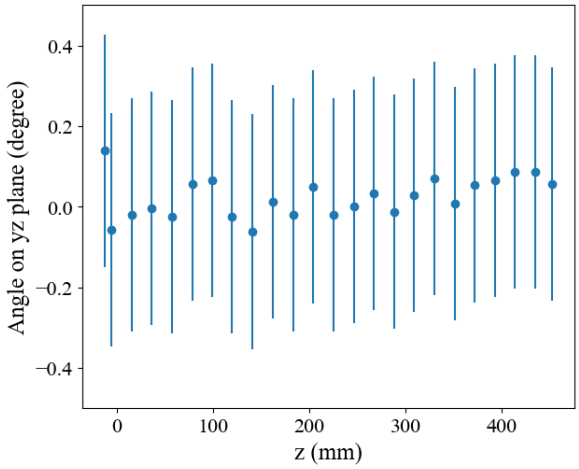


Figure 4.8.: Angles of the central vertical axis of the Hall probe array with respect to the yz-plane in the TGU coordinate system.

Figure 4.8 shows the angle variation with the error bars of the longitudinal axis of the hall probe slide, which is perpendicular to the Hall probe, with respect to the yz-plane.

Such angles with respect to three planes lead to the misalignment of the Hall probes and finally the systematic error of the measured magnetic field. The misalignment errors can cause damages of the Hall probe array from the collision in the narrow TGU gap.

A further investigation with a different strategy using a dummy was required to directly detect collisions at room temperature and also at low temperatures. The Hall probe slide with the dummy aims to investigate an influence of the misalignment error on the Hall probe by scanning along the TGU longitudinal direction.

The structures of the sliding system including the Hall probe slide, brass bar and guide rails were modified for mechanical stability to minimize the misalignments described in subsection 4.2.3. After refurbishment of the guide rails and the brass bar, the measurement system described in subsection 4.2.1 with the Hall probe dummy for the misalignment study was assembled to the TGU.

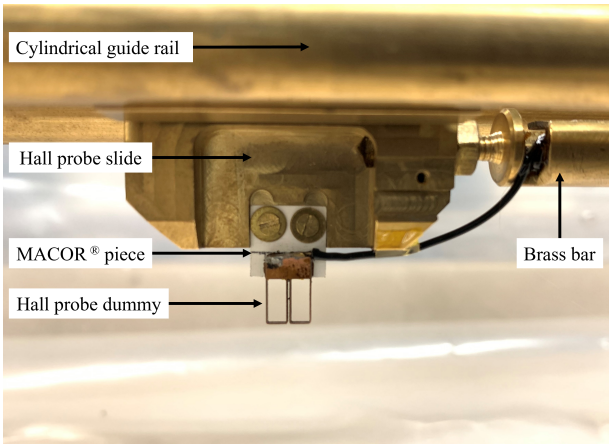


Figure 4.9.: Photograph of the sliding system with the Hall probe dummy attached to the slide.

In Figure 4.9, the MACOR® piece [52] with the dummy was attached to the Hall probe slide. The MACOR® piece is a machinable glass ceramic having an excellent dimensional stability in various environment. The dummy had a shape and dimensions similar to the 7-Hall probe array. It is a hollow structure made of copper to avoid a damage on the TGU coil and yoke because this structure can simply be deformed if the critical contact occurs. Moreover, copper dummy and additional cables were used to determine a possible contact with the coil yoke by an electrical signal. Then, a cryogenic glue, LakeShore varnish VGE-7031 [53], was employed to mount the dummy on the MACOR® ceramic piece. The mounting was tested in a liquid nitrogen bath and the result was that the glue was durable enough and the mounting was stable under cryogenic conditions.

The investigations on the misalignment error were performed in both conditions of atmospheric pressure at room temperature and vacuum with a pressure of 10^{-7} Pa at cryogenic temperature of 80 K to 90 K. The results showed that the repaired brass bar could move through the brass adapter and thus the Hall probe slide with dummy could move along the longitudinal axis of the TGU gap. No damage on the hollow structure of the dummy was also observed, which means no critical contact between the dummy and the TGU pole. In the TGU magnetic field measurement, a special attention is required to avoid a misalignment of the Hall probes which potentially can lead to a collision in the narrow TGU gap and a resultant damage of the probe.

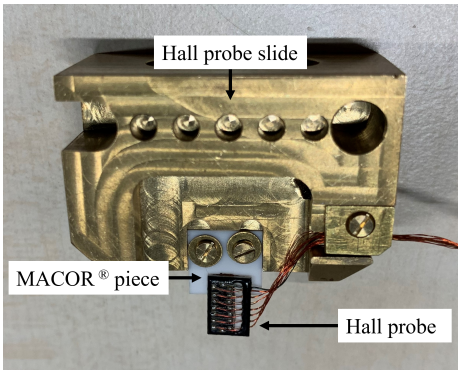
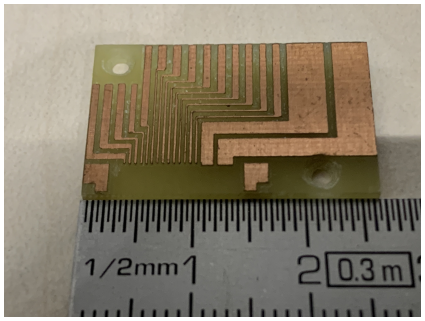


Figure 4.10.: Photograph of the 7-Hall probe array attached to the MACOR® ceramic piece for electrical isolation from the TGU and the measurement system.

(a)



(b)

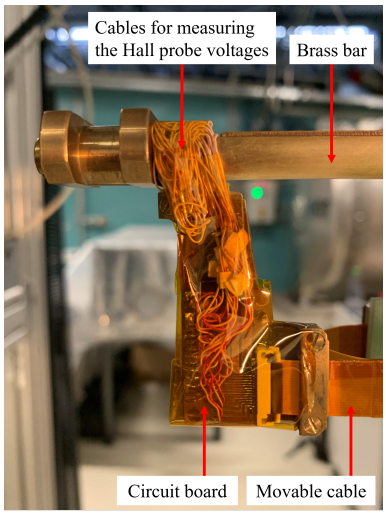


Figure 4.11.: Photographs of (a) a circuit board and (b) Hall probe cables and a movable multi-channel cable connected to the circuit board.

4.2.3. Refurbishment of the Magnetic Field Measurement System

As shown in Figure 4.10, The LakeShore varnish VGE-7031 glue was used to mount the Hall probe on the MACOR® piece. Then, the MACOR® piece with the Hall probe array was placed on the Hall probe slide and fixed with brass screws. Initially, the adapters, the cylindrical guide rails and the slide with the brass bar were assembled without the TGU. The slide was placed between two guide rails and the free end of the brass bar was passed through the borehole of the according adapter.

As shwon in Figure 4.11 (b), the Hall probe cables were inserted in a longitudinal slit of the brass bar and covered by the brass plate. Then, the Hall probe cables coming out from the end of the brass bar were connected to a movable multi-channel cable via a circuit board with separated channels. The surface mounted device (SMD) technique was used for the multi-channel cable connection, which has the advantage of immobility of the cables during scanning in the longitudinal direction.

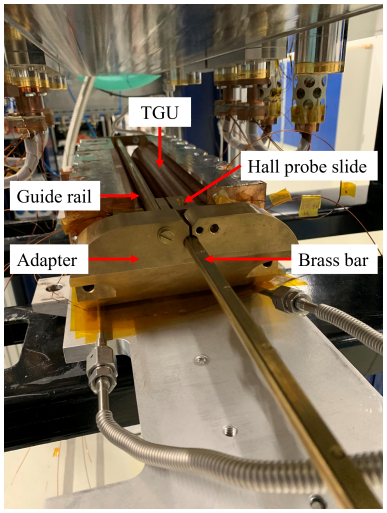


Figure 4.12.: Photograph of the completed sliding system with the Hall probe array attached to the TGU.

Figure 4.12 shows the completed sliding system with the Hall probe array and the associated cables assembled with the TGU. The position of the the TGU was adjusted and the SC wires of the TGU were finalized and clamped along their supports, as described in section 3.1.

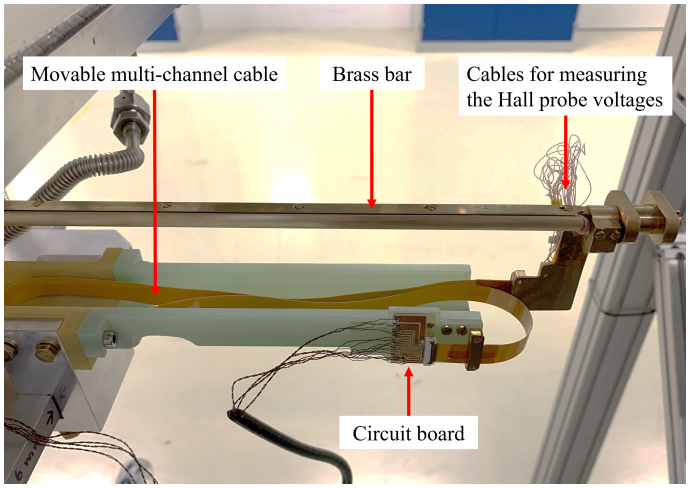


Figure 4.13.: Photograph of the PEEK groove used to limit a movement degree of freedom of the movable multi-channel cable.

Figure 4.13 shows that the movable multichannel cable was placed in the groove made of the G10 (glass-reinforced plastic) to limit its mobility during the longitudinal scanning. The other end of this cable was connected to another circuit board mounted on the G10 plate. 3-m-long phosphor bronze wires [34] were applied to connect the channels of this circuit board to the vacuum feedthroughs mounted on a flange at the top cylinder of the cryostat.

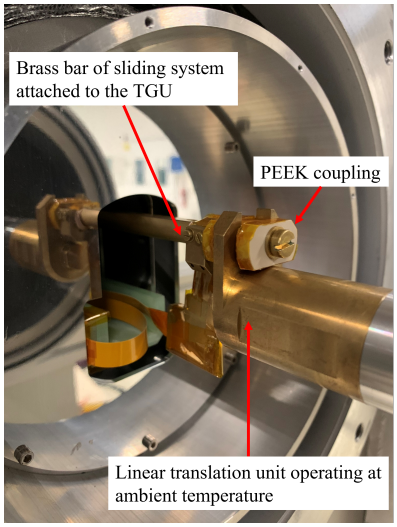


Figure 4.14.: Photograph of the PEEK coupling used for the sliding systems.

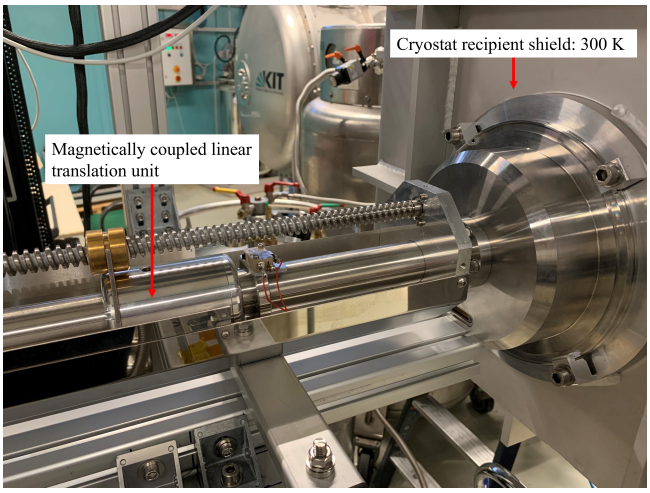


Figure 4.15.: Photograph of the linear translation unit attached to the cryostat recipient shield.

The air-side feedthroughs mounted on the flange of the cryostat were connected to cables of the multichannel scanning card (KEITHLEY Model 7700 Multiplexer Module) of the digital multimeter (KEITHLEY Model 2700). The voltage signals from the Hall probes were recognized by the multichannel scanning card. Finally, the voltages of seven Hall probes were measured by the multimeter [54, 55].

In Figure 4.14, the PEEK coupling was used to connect the brass bar of sliding system attached to the TGU and the linear translation unit operating at ambient temperature. In Figure 4.15, the thermal shields of the cyostat were closed and the brass bar passes through the opening slits in the 4-, 40-, and 77-K thermal shields to connect with the linear translation unit operating at ambient temperature. Finally, the external translation unit was flanged on the recipient.

4.3. Magnetic Field Measurement of the TGU Coil

In this configuration, two TGU coils were connected in series and powered using two pairs of high temperature superconducting (HTS) current feedthroughs with an ampacity of 600 A each, as schematically depicted in Figure 3.23. The magnetic field measurements were performed at a TGU temperature range between 5.8 K and 6.3 K.

4.3.1. Heat Load Introduced by the Measurement System

The first cool-down to the operating temperature of 4.3 K failed because the TGU coil reached 11 K with the measurement system attached. The assumption for this temperature state is that the heat load by conduction through the system of brass rods and couplings was too high and, therefore, the TGU coil did not reach the superconducting state. An estimation of the heat load through the measurement system are discussed as follows.

Table 4.2.: Thermal conductivities of brass at several temperatures [56].

Temperature (K)	**Thermal conductivity** ($\mathrm{W\,m^{-1}\,K^{-1}}$)
455	177
293	144
108	106

Table 4.2 shows thermal conductivities of brass at several temperatures, which can be described as a function of temperature by

$$k(T) = 0.2046T + 83.946.$$

If the heat reservoir at a temperature of 293 K is connected to the brass bar, the temperature at the end of the brass bar and the opposite one attached to the TGU are estimated to 293 K and 4.3 K, respectively. The rate of heat transfer (q) through the brass bar with a length (L) of 0.5 m and a cross-section area (A) of 0.0064 $\mathrm{m^2}$ to the TGU via the conduction process can be evaluate by

$$\begin{aligned} Q &= \frac{A}{L}\int_{T_1}^{T_2} k(T)\,dT \\ &= \frac{0.0064}{0.5}\,\frac{[\mathrm{m^2}]}{[\mathrm{m}]}\int_{4.3}^{293} (0.2046\,T + 83.946)\,dT\ [\mathrm{W\,m^{-1}\,K^{-1}}][\mathrm{K}] \\ &= 422.6\ \mathrm{W}. \end{aligned} \tag{4.16}$$

It is necessary to minimize the rate because the heat can be transferred to the TGU via the brass bar. A replacement of the brass coupling by a PEEK coupling was introduced because it was the least complex solution.

As the temperature distribution along the brass and PEEK coupling are unknown. It was assumed that one end of the brass or PEEK coupling, was attached to the heat reservoir with the temperature of 293 K (T_1). The opposite end was unknown temperature (T_2).

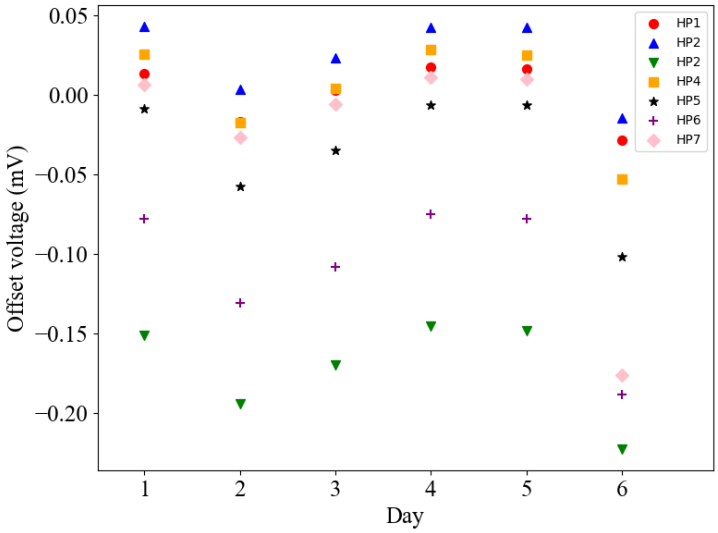


Figure 4.16.: Mean values of the offset voltage of each Hall probe during the measurements over consecutive days.

The thermal conductivities of the both couplings were assumed to be a constant over a temperature range between T_1 and T_2.

Both couplings have the same length and cross-section area. At 293 K, the thermal conductivity of the PEEK coupling is 0.27 W m^{-1} K^{-1}, which is much smaller than that of the brass one of 177 W m^{-1} K^{-1} by the ratio of 0.15 % [57]. This estimation of the heat flow suppression by using the PEEK coupling looks promising.

The second cool-down was performed by using the PEEK coupling instead of the brass one. The reachable temperature of the TGU was 5.8 K to 6.3 K by using the PEEK coupling. This is an evidence that the heat load introduced by the measurement system could be effectively reduced by the exchange of the coupling. However, for the magnetic field measurements at this coil temperature range the operating current of the TGU had to be limited to 50 A. The magnetic flux densities measured at this coil current can linearly be scaled to the values at the nominal operating current at 750 A because there is no an iron in the TGU structure, magnetic permeability equals to μ_0. Therefore, a relationship between the magnetic induction and magnetic field intensity is a constant of proportionality.

4.3.2. Measured Field of the TGU and Time Constant

Figure 4.16 shows the mean values of the offset voltages of each Hall probe during the magnetic measurements over consecutive days. The offset voltages were taken when the applied current of the TGU was zero to calibrate the Hall probes. Then, the mean values of the offset voltage were subtracted from the measured voltages of the Hall probes during the field measurements.

Figure 4.17 shows the offset-corrected measured voltages of the seven Hall probes as a function of time at a TGU current of 40 A. Figure 4.18 shows the temporal behaviours of the measured magnetic fields. The magnetic flux densities were evaluated by using

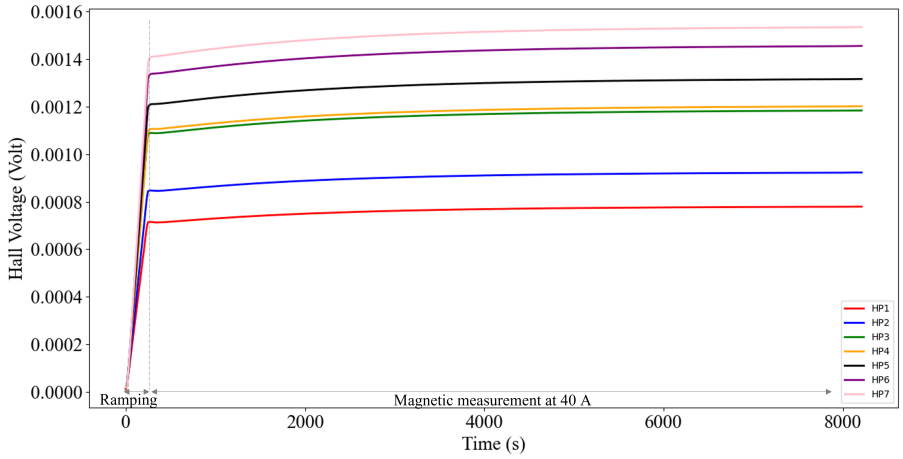


Figure 4.17.: Offset-corrected measured voltages of the seven Hall probes as a function of time at a TGU current of 40 A

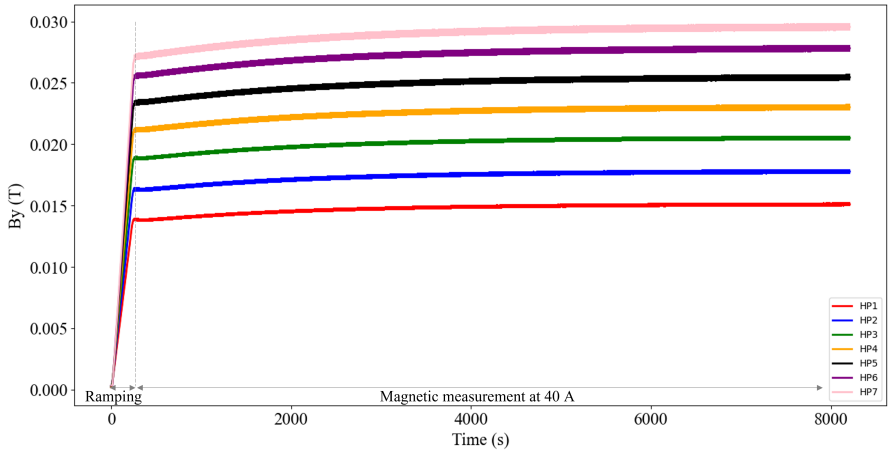


Figure 4.18.: Magnetic flux density amplitudes, including the error bars, measured by seven Hall probes as a function of time at the TGU current of 40 A.

the offset-corrected voltages and the sensitivities of the Hall probes listed in Table 4.1, according to Equation 4.10. The full field was not reached immediately after the current ramp, but showed an exponential asymptotic drift due to the presence of inter-turn and coil-to-former short circuits. The time constant of the exponential, τ is 1400 s. The field measurements were performed after a transient time of 5τ = 7000 s.

4.3.3. Transverse Magnetic Flux Density of the TGU

The perpendicular magnetic flux densities of the TGU were mapped with seven Hall sensors equidistant in the vertical direction along the longitudinal axis at TGU currents of 10, 20 and 30 A. The TGU was powered to the required operating current at the temperature range from 5.8 K to 6.3 K and the mapping of the transverse magnetic flux densities was performed after a transient time of 7000 s.

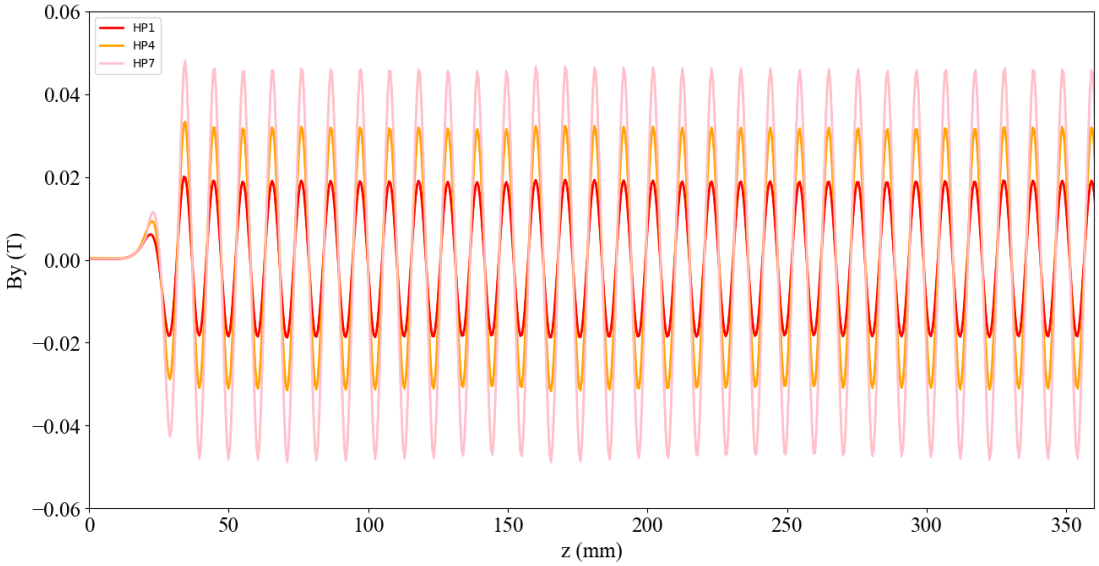


Figure 4.19.: Magnetic distribution along parallel longitudinal axes at the transverse direction of Hall probe 1, 4 and 7 at a TGU operating current of 30 A.

However, the mapping along the longitudinal axis could not be completed at the current of 50 A due to the unstable TGU temperature. The observed temperature rise while the Hall probes were moved approached the critical temperature of the SC wire, which could have lead to a quench.

Figure 4.19 shows the mapping of the transverse magnetic flux densities by seven Hall probes along the longitudinal axes at a TGU current of 30 A. The mapping could be performed for only 32 periods (out of 40 periods in total) with a resolution of 0.5 mm due to the mechanical restriction of the sliding system. The transverse positions of the Hall probes with respect to the center of the TGU were 9.30, 6.75, and 4.20 mm for the probe numbers of 1, 4, and 7, respectively. The transverse spacing between the probes is 0.85 mm.

Figure 4.20 shows the measured magnetic flux density of the TGU coil as a function of the coil current for the probe numbers of 1, 4, and 7. The measured results for the seven Hall probes showed linearities between the coil currents and the magnetic flux density as expected. This linearities confirm that the magnetic flux density can be proportionally scaled to the operating current of 750 A.

In subsection 4.2.2, the misalignment of the Hall probes due to the angles with respect to the reference planes was described. It should be noted that the flux density measurements are very sensitive to the misalignment of the Hall probe array due to the large flux density gradients present in the TGU gap. Therefore the standard deviation and the averaged value of the amplitude at each period were evaluated to investigate the measurement quality.

The measured field amplitudes averaged over the 32 measured periods including standard deviations and the ideal fields, at a TGU operating current of 30 A, and transverse positions of the Hall probes are listed in Table 4.3. A preliminary evaluation of the transverse flux density slope at the longitudinal position of a flux density maximum is shown in

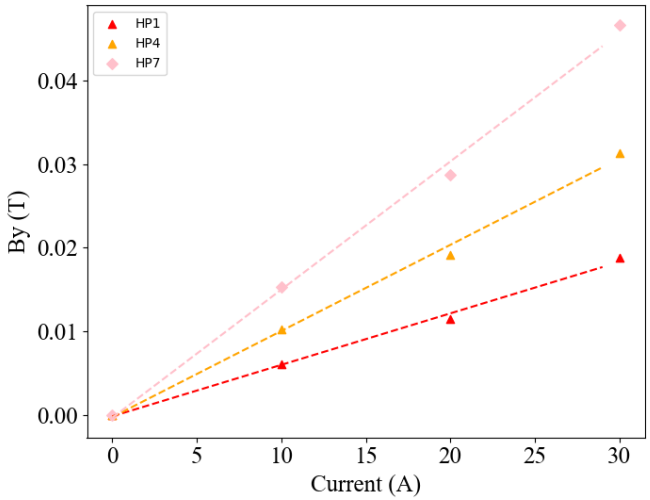


Figure 4.20.: Magnetic flux density as a function of the TGU coil current for the probe numbers of 1, 4, and 7.

Table 4.3.: Perpendicular magnetic fields of maximum flux densities averaged over the 32 measured periods and the ideal fields at a TGU operating current of 30 A.

Probe	**Ideal x-position** (mm)	**Measured field** (mT)	**Standard deviation** (mT)	**Ideal field** (mT)
1	9.30	18.75	0.191	22.86
2	8.45	22.61	0.247	26.72
3	7.60	26.97	0.322	30.83
4	6.75	31.37	0.407	35.09
5	5.90	36.11	0.511	39.41
6	5.05	41.44	0.627	43.62
7	4.20	46.63	0.752	47.57

Figure 4.21. The differences between the measured and theoretical data are caused by the error of sensitivities of the Hall probes due to the temperature difference. Unfortunately, as the sensitivity data at 4.2 K were not available, the data at 77 K were inevitably used. A comparison with the flux density values calculated using the OPERA 3-D code shows a similar tendency with a small difference. The error bars indicate the statistical and the systematic errors due to the Hall probe sensitivity error of the measurements.

Suppose that an electron with an energy of 120 MeV travels through the TGU in the ideal transverse position (x-axis) of 6.40 mm, which are the positions between the Hall prove 4 and 5, respectively [37, 58]. By a linear interpolation using the magnetic field amplitude of the position $x = 6.75$ mm and $x = 5.90$ mm, the field amplitude at the position $x = 6.40$ mm is equals 32.44 mT. The relative transverse magnetic field gradient, α, is given by:

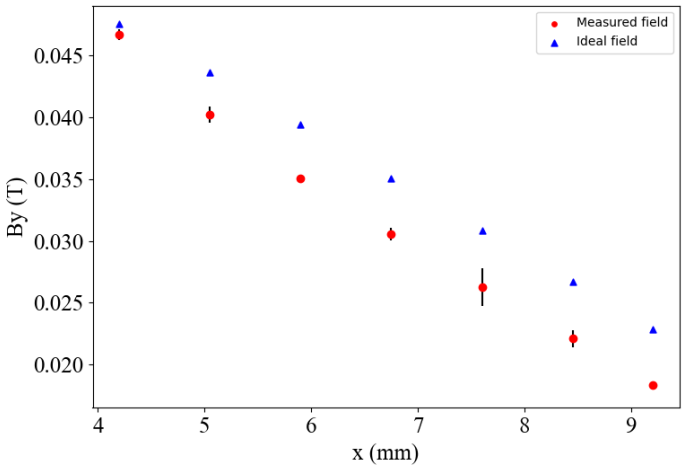


Figure 4.21.: Perpendicular magnetic fields measured from 7-Hall probe array and the fields calculated from the ideal position of the Hall probes dependent on a distance from the TGU center at a TGU operating current of 30 A.

$$\alpha\ [\mathrm{m}^{-1}] = \frac{\Delta B}{B\Delta x}\frac{[\mathrm{mT}]}{[\mathrm{mT\,m}]}, \tag{4.17}$$

where $\Delta B = B_{HP5} - B_{HP4}$, $\Delta x = 0.85$ mm and B is the result of linear interpolation of the magnetic field at the ideal position of the 120 MeV-electron beam. Then, the relative transverse flux density gradient at the ideal transverse position of the 120 MeV-electron beam., at 30 A, is evaluated to be

$$\begin{aligned}\alpha\ [\mathrm{m}^{-1}] &= \frac{35.1 - 30.58}{32.44\ \times\ 0.85 \times 10^{-3}}\frac{[\mathrm{mT}]}{[\mathrm{mT\,m}]} \\ &= 163.92\ \mathrm{m}^{-1}.\end{aligned}$$

In case of the expected model evaluation of the TGU, the relative transverse gradient was evaluated to 149.5 m^{-1} [58]. It is clearly seen that the systematic measurement error due to the sensitivity values of the Hall probes at 77 K used in the calculations of the field amplitudes affect the measured magnetic fields.

In the following step, 3-D magnetic field distributions will be constructed using the measured magnetic fields from the Hall probes and their ideal positions. The field distributions will then be employed for particle tracking and radiation field calculations in the WAVE simulations. The methodology and simulation results will be described and discussed in chapter 5.

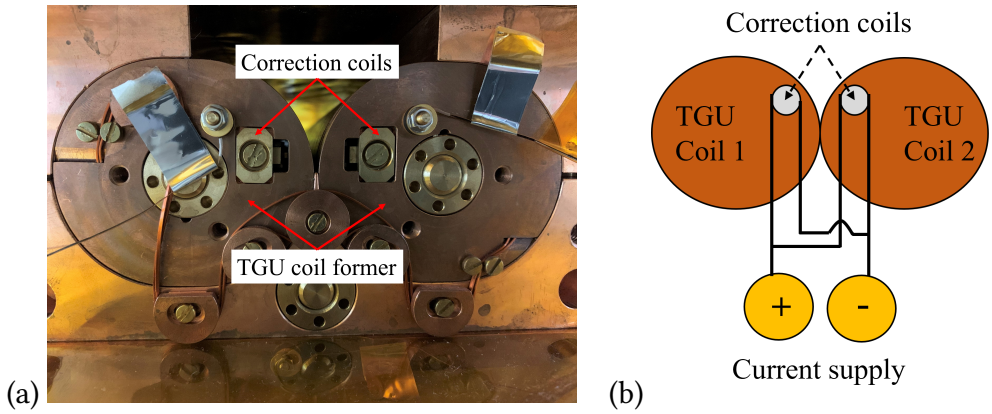


Figure 4.22.: (a) Photograph of correction coils inserted into the TGU coil former and (b) diagram explaining the wiring of the correction coil in a parallel circuit.

4.4. Magnetic Field Measurements of the Correction Coils

4.4.1. Measured Fields and Time Constants of the Correction Coils

As shown in Figure 4.22, two superconducting correction coils are installed inside the TGU coil former and they were connected in a parallel circuit with an additional DC current supply. Both coils were powered together with the current between 0 A and 10 A, which means that the maximum current for each coil is 5 A.

Figure 4.23 shows offset-corrected measured voltages of the seven Hall probes as a function of time at a correction coil current of 5 A. Figure 4.24 shows the temporal behaviour of the measured magnetic fields of the correction coil. The magnetic fields were evaluated using a procedure similar to the case of the TGU fields. The measurement results show that the full fields are reached within 10 minutes after the current ramp.

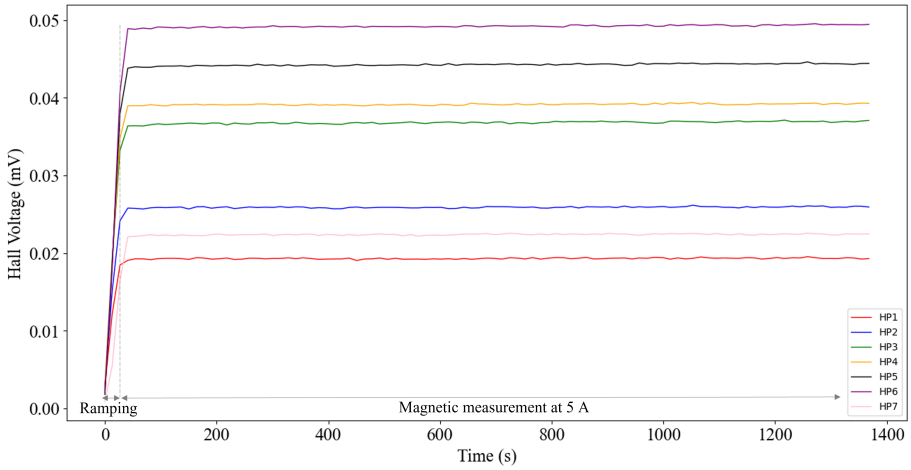


Figure 4.23.: Offset-corrected measured voltages of the seven Hall probes as a function of time at a correction coil current of 5 A.

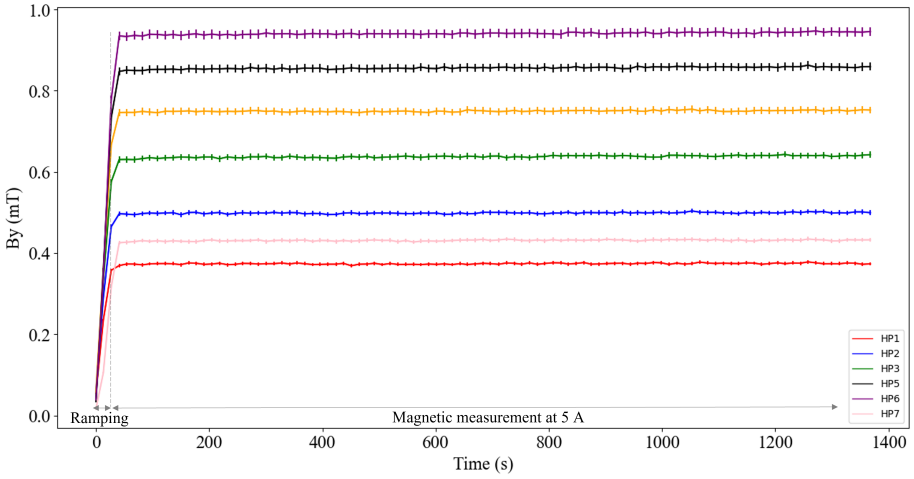


Figure 4.24.: Magnetic flux densities measured by the seven Hall probes as a function of time at a correction coil current of 5 A.

4.4.2. Transverse Magnetic Flux Densities of the Correction Coils

As shown in Figure 4.25, the perpendicular magnetic flux densities of the correction coils were mapped with the seven Hall sensors equidistant in the vertical direction along the longitudinal axis when the current of each coil was 5 A. The mapping of the magnetic flux densities was performed 30 minutes after reaching the constant correction coil current. The temperature of the TGU coil formers during the mapping was 5.8 K to 6.3 K. The mapping was performed with a resolution of 0.5 mm along the longitudinal axis, which could not be completed for the entire length of the TGU due to the mechanical restriction of the sliding system.

At the correction coil current of 5 A, the measured field amplitudes ranged from 0.4 mT to 1.1 mT. The magnetic flux densities should have constant field amplitudes along the longitudinal direction. However, the measured results showed an unexpected periodicity with small oscillation along the longitudinal direction. The period length of those periodic profiles was around 5 mm, which is equivalent to a half of the TGU period length.

The possible reason is expected that the TGU magnetic flux density did not decay completely. The similar effects have been observed for the 2-period model and a likely reason for these periodic structures are slowly decaying persistent currents in the TGU main windings [59]. To confirm this effect, the background field without magnetic powering should firstly be measured along the longitudinal direction. Then, the correction fields should be re-measured after the thermal cycle before powering the TGU main coils. In addition, the wiring configuration should be modified to the series-circuit to increase ability to control the distribution of the current on two coils.

Figure 4.26 shows the measured magnetic flux density of the correction coil as a function of the coil current. The temporal behaviour for each current ramping was investigated and then, the magnetic field values were recorded after reaching the full fields in 20 minutes after the current ramping. The measured results for the seven Hall probes showed linearities between the coil currents and the field as expected.

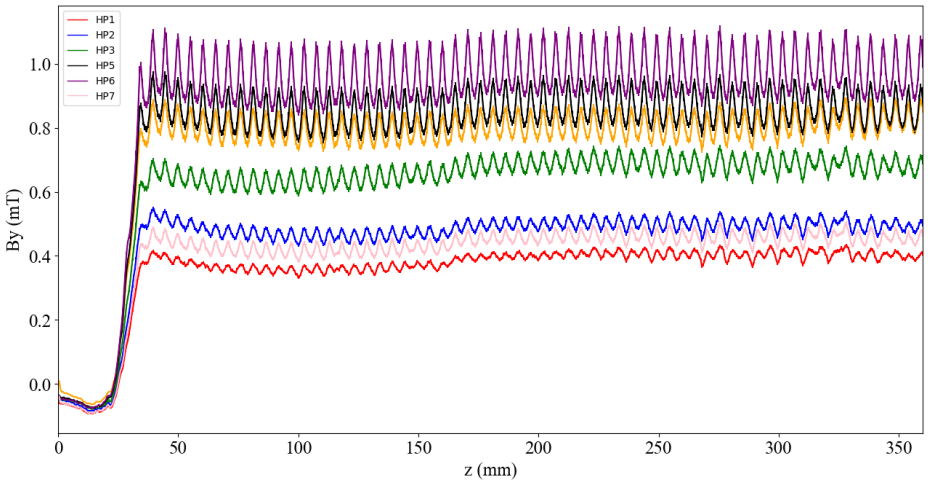


Figure 4.25.: Magnetic flux densities along longitudinal axes at the transverse positions of seven Hall probes at a correcting coil current of 5 A.

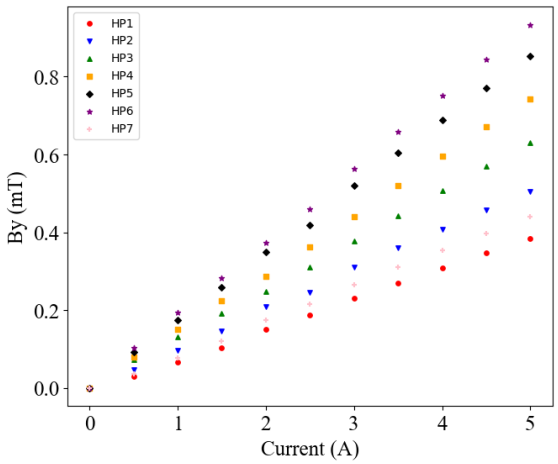


Figure 4.26.: Magnetic flux density as a function of the correction coil current.

Figure 4.27 shows the measured magnetic flux density as a function of the transverse position at the correction coil current of 5 A. The measured fields did not represent the parabolic distribution with respect to the design field [12]. At the transverse positions ranged from 5.05 mm to 9.30 mm magnetic flux density decreased with a parabolic slope. In case of the field at $x = 4.20$ mm showed a different tendency. The magnetic flux density of the TGU described in the previous section confirms that the difference of the field at $x = 4.20$ mm is not caused by the calibration error of the Hall sensor.

In conclusion of the magnetic measurements for both TGU and correction coils, the sliding system attached to the TGU and its coupling to the parts at ambient temperature should be redesigned to suppress the heat load through the magnetic measurement system and then to reach 4.3 K to 4.4 K. In the reported measurements, the replacement of the

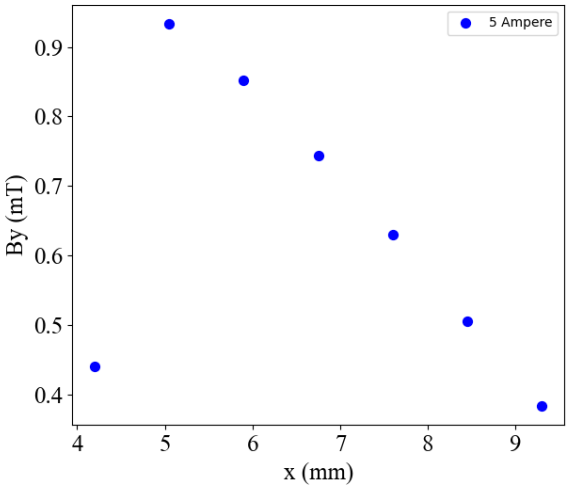


Figure 4.27.: Magnetic flux density as a function of the transverse position at correction coil current of 5 A.

brass coupling by the PEEK one between the sliding systems was sufficient for allowing the TGU temperature to be maintained below the critical temperature of the SC wire material. This provided the first measurement results described in this thesis.

For enhanced magnetic field measurements in the future, more investigations about the sensitivities of the Hall probes at 4.2 K, the correction schemes the sensitivity errors and the misalignments of the Hall probe array are required.

5. Evaluation of the TGU radiation

In this chapter, the radiation generated in the TGU where the electrons travel under the influence of the measured magnetic fields is evaluated using the WAVE simulation code. The code has been developed for evaluating spontaneous synchrotron radiation with arbitrary magnetic fields at the Helmholtz Zentrum Berlin (HZB) [1]. The electron trajectory in the simulation consists of pieces of circular paths with orientation and bending radii determined by the local magnetic field. The spectrum calculation is based on a numerical integration of the radiation field terms derived from the Lienard-Wiechert potential for a defined observation point. Then, the spectral flux density and brilliance are calculated.

The magnetic field distributions imported for the WAVE simulations, the electron trajectories in the magnetic fields and the estimation of the radiation properties at the observation points are described in the following. The evaluations aim to prove that narrow-bandwidth radiation can be generated in the TGU by a properly spectrally dispersed from high-energy spread electron beam, as expected from the theory described in section 2.3.

In the WAVE simulations described in the following, the large-energy spread beam is in a sense represented by a set of seven zero-emittance, zero-energy spread beamlets with a (more or less arbitrarily chosen) current of 0.1 A each. The simulations aimed to qualify the magnetic fields measured in the TGU, which means the influence of a deviation of the field amplitude on the spectral width of the radiation. Therefore, the monochromatic electrons were used in the simulations.

5.1. Construction of the 3-D Magnetic Field maps for Evaluation

A 3-D magnetic field distribution is required for the WAVE simulations. This is rather complicate to construct a full Maxwell-conform 3-D field distribution of the real TGU based on seven measured field lines. The strongly simplifying approach was selected, as the alternative method, in order to achieve a first understanding of the influence of the field quality on the radiation performance of the real TGU. The construction of magnetic field distribution is described in the follows.

As described in section 4.3, the perpendicular magnetic fields were measured at the TGU current of 30 A and the field values were scaled to the TGU operation current of 750 A. The dispersion plane of the TGU is $y = 0$ plane and the perpendicular magnetic fields (y-axis) in the plane were measured along the longitudinal direction (z-axis) at seven different Hall probe positions in x.

The 2-D field map is distinguished from seven 1-D field line corresponding to transverse positions of the Hall probes. Considering the 1-D field line measured from a single Hall

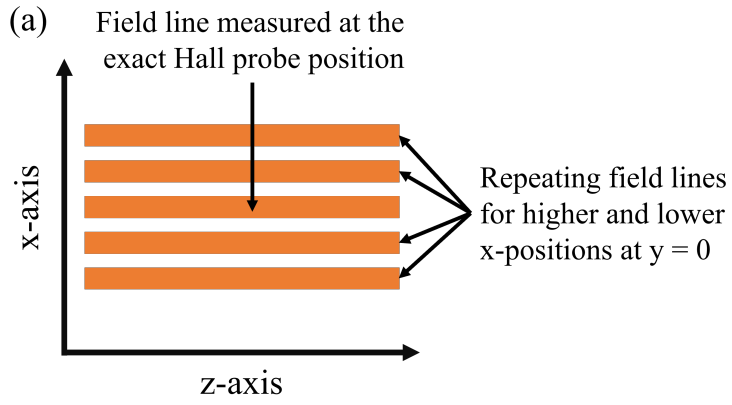


Figure 5.1.: Construction of the 2-D field map in the dispersion plane of the TGU, $y = 0$.

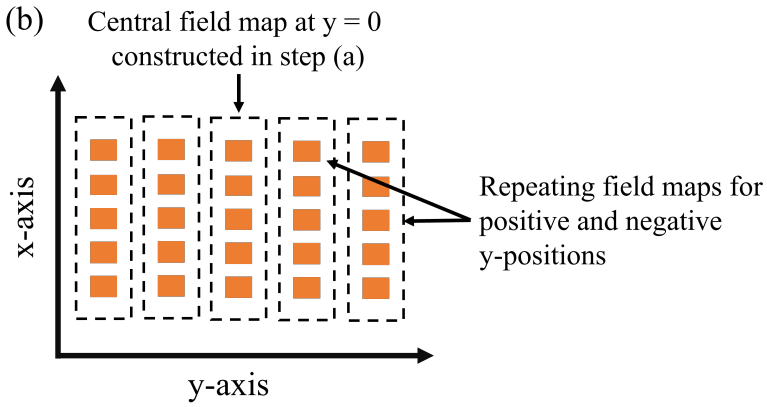


Figure 5.2.: Construction of the 3-D field distribution for the dispersion region of the TGU.

probe, the position of the field line was used as a central axis for constructing the 3-D field distribution. First, a 2-D field map in the vertical plane, at $y = 0$, was constructed by repeating the 1-D measured field line to place at higher and lower x-positions, as shown in Figure 5.1. Each orange-colored block represents a sinusoidal field structure. The result of the field map in this step is similar to the field at a center of the planar undulator, where vertical positions (x-axis) at any z-position have the same field amplitude.

Second, the entire 2-D field maps at $y = 0$ are repeated to construct the dispersion planes for other positive and negative y-positions, as shown in Figure 5.2. Thus, the horizontal positions (y-axis) at any $x-z$ plane have the same field amplitude. This procedure provides 3-D field distributions with central longitudinal axis at $y = 0$ and $x = 9.30$, 6.75 and 4.20 mm for the measured field of the Hall probe 1, 4 and 7, respectively. The longitudinal (z-axis) and vertical (x-axis) field components were defined as zero for all positions in the 3-D field distribution.

The 3-D distributions for each transverse position were initially imported to the WAVE code and the electron trajectories were evaluated. The origin of the reference coordinate system is at the same origin with the 3-D field, $(x, y, z) = (0, 0, 0)$. The results showed that

Table 5.1.: Average offset magnetic field of each hall probe.

Probe number	**Position in x-axis** (mm)	**Field integral** (mT mm)	**Offset magnetic field** (mT)
1	9.300	1422.02	3.99
2	8.450	1854.25	5.21
3	7.600	2297.53	6.45
4	6.750	2528.25	7.10
5	5.900	3021.96	8.49
6	5.050	3409.54	9.58
7	4.200	−8661.32	−24.33

the electron trajectories exhibited an influence from a dipole magnetic field component, which means that the electron trajectories had large overall bending angles. The final electron trajectory shifted from the initial one in order of 600 µm. Finally, the electrons are left from the magnetic field region. These field components were further investigated: Field integrals over different longitudinal regions of transverse distribution measured by the seven hall probes, which is given by

$$B_{\text{off}} = \frac{1}{L} \int B \, dl, \tag{5.1}$$

where L is a total length of the integration path along the magnetic field distribution and B is a magnitude of the transverse magnetic field which is perpendicular to the electron trajectory (dl). The field integral over the total length of the field divided by the total length is expected to be zero. A non-zero field integral result can be referred to as an average dipole field component or an average offset field likely generated by a surrounding magnetic source.

In this evaluation, the length from the zero-position of the field measurement to the end of the 32^{th} period was taken into account for the total length of 356 mm. The results of the field integrals and the offset field from surrounding magnetic source for each Hall probe position are shown in Table 5.1. The offset fields from positions of Hall probe 1 to 6 show a systematic increasing with a linear relation as shown in Figure 5.3. For the Hall probe 7, the value is much higher than the others. The minus sign of the value means that it is in the opposite direction to the others. These dipole field components were subtracted from all positions in the constructed 3-D field distributions.

The seven 3-D field distributions constructed from the measured TGU fields were imported to WAVE code to evaluate the radiation from different electron energies. The imported fields were evaluated using a quadratic interpolation. For further evaluations, a position to start the electron trajectory inside the TGU was selected in order to avoid the initial kick. The electron trajectories along the magnetic fields and the resultant radiation will be described in the following section.

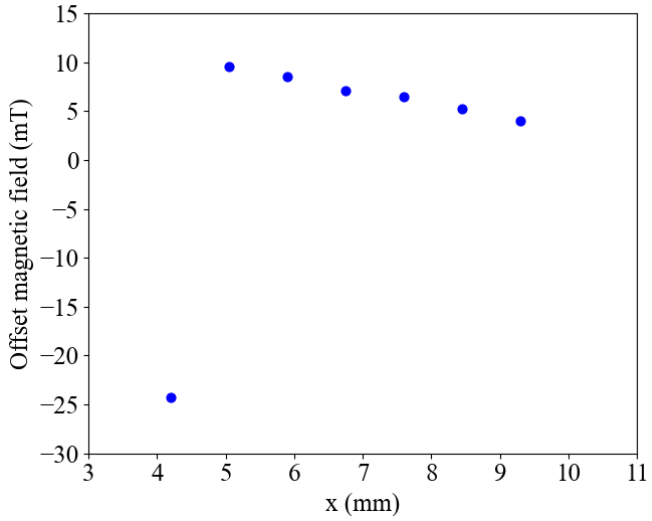


Figure 5.3.: Average offset magnetic field of each hall probe dependence of distance in x-axis.

5.2. Electron Trajectory in the Magnetic Field

In Figure 5.4 (a), the 3-D field distribution with a central axis at $x = 5.90$ mm and the magnetic field amplitude of 0.946 T were imported to the WAVE. A single electron with an energy of 112 MeV was initiated at a position of $z = 0$ and $x = 5.90$ mm, which correspond to the starting position of the field in z and the position of the Hall probe 5 in x, respectively. The electron travels through the magnetic field and follows a sinusoidal trajectory. The trajectory was evaluated with a precision of 200,000 steps per meter.

However, the subtraction of the average magnetic field is not sufficient to suppress the influence of the dipole field component. The trajectory shows two different bending behaviours. The first bending was found from the beginning of the path and the second from the position around $z = 200$ mm with a larger bending radius. The transverse position is shifted from the initial position by around 600 µm.

The relatively strong bending behaviour shown in Figure 5.4 (a) was also found in other evaluated electron trajectories with different 3-D field distributions. The initial and final x-positions and their differences for the electron trajectories evaluated along the seven 3-D magnetic field distributions are listed in Table 5.2.

In subsection 2.1.4, the characteristic conditions for the undulator radiation were discussed. When the relativistic electrons travel through the periodic magnetic field, they emit radiation in a narrow cone with a maximum opening angle (Equation 2.29) with respect to the axis of:

$$\theta_{\max} \leq \frac{1}{\gamma}, \quad (K \leq 1).$$

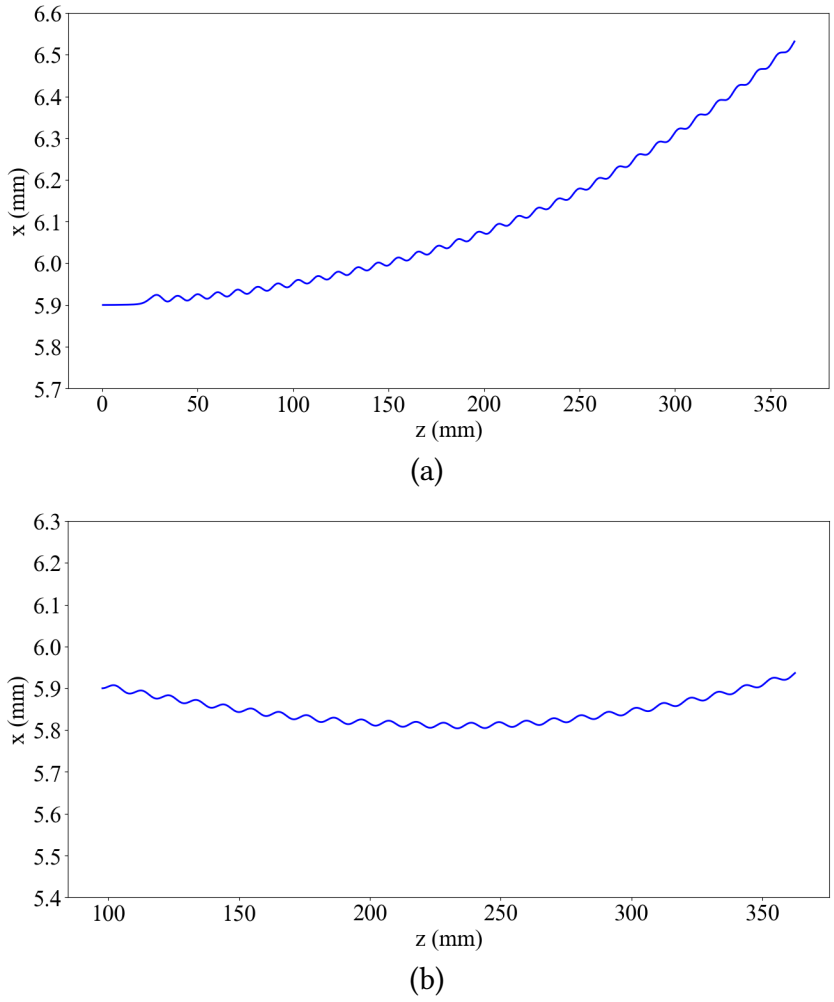


Figure 5.4.: Trajectories of the electron with an energy of 112 MeV (a) traveling through the entire magnetic field and (b) initiated at $z = 9.775$ mm traveling through the rest part of magnetic field.

In order to satisfy this condition, the initial longitudinal position of the electrons in the magnetic field was investigated to minimize the influence of the external dipole field component and to achieve a trajectory as straight as possible. It is expected that the radiation can be concentrated in a narrow cone, with a high intensity and a narrow spectral width, in the forward direction with respect to an electron beam.

In Figure 5.4 (b), an initial point at $z = 9.775$ mm and $x = 5.90$ mm was selected for the electron with an energy of 112 MeV to avoid the bending at the beginning of the trajectory and to minimize the influence of the second bending. The field at the selected initial position leads to a small initial kick, which can compensate for the second bending. Thus, the change in transversal position of the overall trajectory stays below 100 µm.

Beside the electron trajectory, the period number of the TGU (N_u) is another important parameter. In optimizations to minimize the bending behavior, it is necessary to achieve a sufficient magnetic field period. This is because the number of contributing periods

Table 5.2.: Comparison between the initial and final x-positions of the electron trajectories when electrons were initiated at $z = 0$ mm in all cases.

3-D field number	Initial x-position (mm)	Final x-position (mm)	Difference (μm)
1	9.300	9.630	330
2	8.450	8.864	414
3	7.600	8.064	464
4	6.750	7.299	549
5	5.900	6.531	631
6	5.050	5.712	662
7	4.200	5.160	960

determines the radiation bandwidth and the opening angle of the monochromatic undulator radiation as described in detail in the chapter 2. Due to optimizations of the initial position of electron, the contributing period of the magnetic field becomes 25 periods. The radiation evaluations contributed by these optimizations will be described in the following section.

However, the reason of the offset field is still unknown. For the further operation of the TGU and magnetic field measurements, a deeper investigation of the source of these fields and a correction scheme will be required.

5.3. Evaluation of the Radiation Properties

Resonance Condition of Radiation

Seven 3-D field distributions with seven central longitudinal axes and magnetic field amplitudes, as a function of transverse positions, represent the transverse gradient of the TGU magnetic fields. In the WAVE simulations, the field distributions with different field amplitudes were applied to emit radiation with similar wavelengths from electrons with different energies. The resonance condition for all electron energies is expressed by the following equation:

$$\lambda = \frac{\lambda_u}{2\gamma^2(x)}\left(1 + \frac{K^2(x)}{2} + \gamma^2(x)\theta^2(x)\right) \tag{5.2}$$

.

Assuming that the observation angle (θ) is close to zero due to the observation at a large distance from the radiation source, the resonance condition can be reduced to

$$\lambda = \frac{\lambda_u}{2\gamma^2(x)}\left(1 + \frac{K^2(x)}{2}\right) \tag{5.3}$$

.

Considering to the original TGU design parameters as published in [58], the design electron energy (E_0) is 120 MeV with the corresponding a Lorentz factor (γ) of 234.8 and the undulator parameter (K_0) of 1.07. By the Equation 5.3, the photon wavelength (λ)

Table 5.3.: Parameters used in the WAVE simulations.

Initial x-position (mm)	**Magnetic field amplitude** (T)	**Electron energy** (MeV)
9.300	0.469	100.518
8.450	0.566	102.681
7.600	0.674	105.523
6.750	0.784	108.813
5.900	0.903	112.771
5.050	1.036	117.699
4.200	1.166	122.903

was evaluated to 150 nm or in the photon energy E_{ph} of 8.265 eV. These parameters were determined from the nominal TGU period length (λ_u) of 10.5 mm and the corresponding magnetic field amplitude (B_0) of 1.09 T.

The radiation wavelength of around 150 nm or the photon energies of 8.26 eV to 8.27 eV are also the target values in the WAVE simulations. In the following, the electron energy as function of the x positions will be investigated in order to produce undulator radiations using the measured fields at the according x positions.

Initial Condition of the Electron

The magnetic field amplitudes averaged over the measured periods of each of the Hall probe scans were used to evaluate the related undulator parameter and electron energy. From Equation 5.3, the electron energy for a given undulator parameter can be determined by

$$E_0(x) = m_e c^2 \sqrt{\frac{\lambda_u}{2\lambda}\left(1 + \frac{K^2(x)}{2}\right)}. \tag{5.4}$$

Beside the central energy evaluated by using Equation 5.4, the electron energies larger and smaller than the central energy were also used in the simulations to investigate the photon energy dependence of the electron energy. The initial position of the Hall probe plus electron oscillation amplitude in x-axis, the average values of the magnetic field amplitudes over 32 periods, and the electron energies used in the WAVE simulations are listed in Table 5.3.

Radiation Spectrum Evaluation

The characteristic properties of the undulator radiation are generally described in terms of photon flux through a finite pinhole or the spectral photon flux density which is integrated over the radiation cone in the forward direction and divided by the size and divergence of the source [58].

For the simulations described in the following, seven observation points for evaluating the photon flux density were defined as the center of a rectangular pinhole, which were located at a longitudinal position of $z = 10$ m and associated x positions of electrons. That

Table 5.4.: Details of the pinhole for evaluating the photon flux densities

Parameter	Value	Unit
Width of pinhole	3	mm
Height of pinhole	3	mm
Number of horizontal grid points	100	
Number of vertical grid points	100	
Horizontal mesh size in pinhole	30	µm
Vertical mesh size in pinhole	30	µm
Position in z-axis	10	m
Position in x-axis	4.20-9.30	mm
Position in y-axis	0	mm

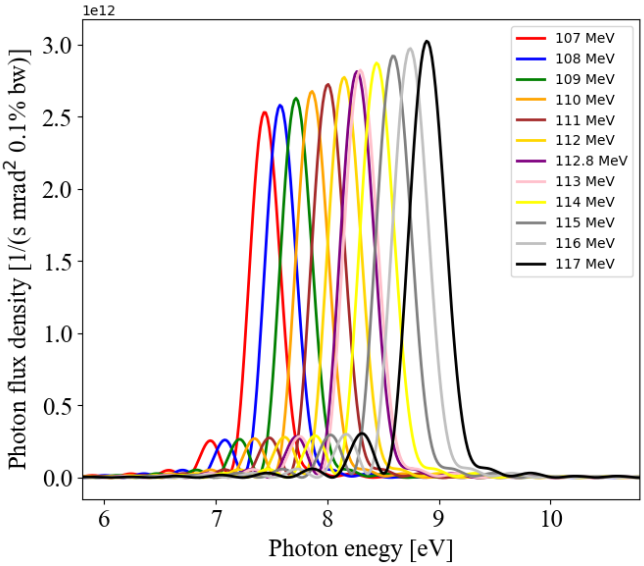


Figure 5.5.: Photon flux density vs. photon energy at the field amplitude of 0.903 T.

means that there are seven observation points with respect to the positions of the electrons. As the observation points are placed at a finite distance and have a finite aperture, the photon flux densities are evaluated within a small angular acceptance. The details of the pinhole are listed in Table 5.4.

For evaluating the photon flux density in the limits of the rectangular pinhole, each point on the rectangular grid was taken into account. The flux density was evaluated at the grid points and, then, integrated over the grid to obtain the flux using spline techniques [60]. An accuracy number (maximal number of integration steps per one source of the radiation) of 20,000 was used for the spectrum evaluation, which was informed to be sufficient for high precision evaluations [60].

For the resonance condition of the photon energy of 8.26 eV, the radiation spectrum was evaluated in the pinhole for 500 equidistant photon energies from the lowest photon energy of 4.0 eV to the highest one of 12.0 eV.

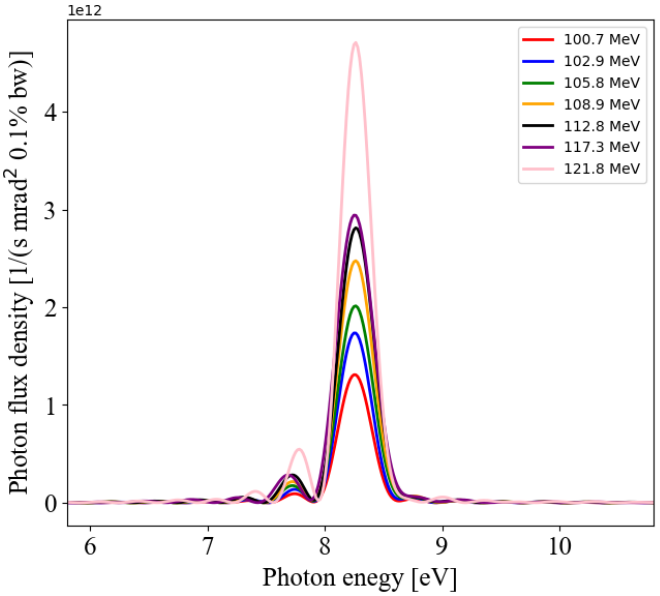


Figure 5.6.: Photon flux density vs. photon energy of 8.26 eV.

Figure 5.5 represents the example results of photon flux densities in the pinhole when electrons with various energies travel through the magnetic field with amplitude of 0.903 T. The electron energies were firstly varied from 107 MeV to 117 MeV using a step of 1 MeV to slope expected energy range which contribute photon energy around 8.2 MeV to 8.3 MeV.

Then, the electron energies were varied within that expected range using a step size of 0.1 MeV. Eventually, a linear interpolation was used to evaluate the electron energy which resulted the photon energy (ω_0) of 8.26 eV. For this magnetic field amplitude, the resulted electron energy was 112.744 MeV and the evaluated photon flux density has a spectral width ($\Delta\omega$) of 0.32 eV at FWHM. The relative spectral width ($\Delta\omega/\omega_0$) was evaluated to 0.038. In the Equation 2.48, the relative spectral width can also be evaluated using the contributing magnetic field of 25 periods (N_u), which equals to 0.04.

Figure 5.6 shows seven photon flux density distributions at the photon energies of around 8.26 eV. Each photon flux density was resulted from the electron energies corresponding to the magnetic field amplitudes at each transverse position. At the constant width and height of the aperture of 3 mm, the photon flux density is proportional to the electron energy, as described in Equation 2.47.

Figure 5.7 shows the electron energies for the photon energy of 8.26 eV achieved by the undulator equation and the WAVE simulations. The results show approximately linear relationships between the electron energies and the transverse positions of the TGU. The differences between the electron energies in the ideal dispersion and the WAVE simulation at the same field amplitude and the relative spectral widths of the simulated results are listed in Table 5.5.

In this chapter, the electron trajectories along the seven 3-D magnetic field distributions were simulated using the WAVE code. These field distributions were constructed using the 2-D field map scaled from the measured results with seven Hall probes. The selected

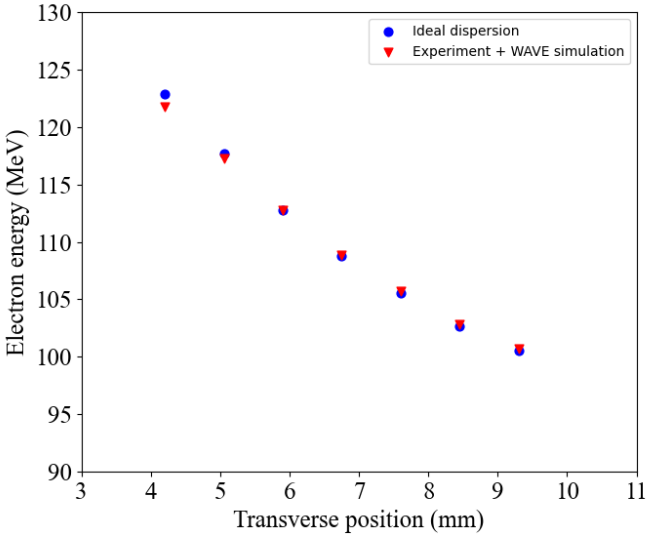


Figure 5.7.: Electron energy corresponding to the photon energy of 8.26 eV as a function of transverse position.

Table 5.5.: Comparison of electron energies for the photon energy of 8.26 eV in the undulator equation and the WAVE simulation and the relative spectral width.

Field amplitude (T)	**Ideal dispersion** (MeV)	**WAVE simulation** (MeV)	**Relative width** ($\Delta\omega/\omega_0$)
0.469	100.518	100.647	0.038
0.566	102.681	102.852	0.039
0.674	105.523	105.749	0.041
0.784	108.813	108.826	0.041
0.903	112.771	112.744	0.038
1.036	117.699	117.272	0.044
1.166	122.903	121.772	0.037

position in the longitudinal axis is sufficient to start the electron trajectories to avoid the initial bending and to achieve narrow-radiation cone through the finite aperture.

The simulation results showed that a narrow-bandwidth radiation with the relative spectral width and the photon energy of around 0.04 and 8.26 eV, respectively, could be generated from the TGU by the electrons with different energies and the constructed magnetic field distributions. The difference in the electron energies corresponds to an electron beam with dispersed electrons from the high energy spread.

6. Conclusions

The achievements of the experiments and evaluations described in this thesis can be summarized as follows:

1) Magnetic powering tests

A superconducting TGU having 40 periods was successfully tested in its own cryostat. Both TGU coils reached the nominal operating current of 750 A. The temperature of the TGU at the operating current was around 4.4 K. That could be achieved by means of the additional support structures for the SC wires, the conduct-cooled cylinders for the splices and the improved soldering connections between the SC wires. These measures also made it possible to stably operate the TGU at currents of up to 850 A.

It was clearly seen that the ramping to the operating current in a single step with a ramp rate of 0.2 A s^{-1} was more efficient than that in several steps. The rise of the TGU temperature due to the eddy current heating stayed well below the critical temperature of the superconductor and the entire ramping time to reach the nominal operating current was shorter than 1.5 hours.

The test results provide significant information such as the TGU temperature rise during the current ramping, the cooling efficiency of the cryostat and the total time consumed in the entire ramping from zero to operating current. From this information, an optimal powering method could be determined for the TGU operation and the following transverse magnetic field measurements.

2) Magnetic field measurements

Perpendicular magnetic fields of the TGU were measured at coil temperatures ranging from 5.8 K to 6.3 K. These elevated temperatures were caused by considerable heat transfer through the structure of the measurement system. The TGU can reach the superconducting state when its temperature is lower than the critical temperature. However, because it could not be powered to the nominal operating current, a rather small applied current between 10 and 50 A, which is 1.3 % to 6.7 % of the nominal operating current of 750 A, was used for the measurements. This magnetic field measurement can nonetheless be regarded as representative based on the fact that the TGU is an iron-free device and the magnetic flux density is proportionally scaling with the applied current.

The measured perpendicular magnetic fields showed an exponential asymptotic drift in time due to the presence of inter-turn and coil-to-former short circuits. The time constant of the drift was calculated to be $\tau = 1400$ s. The magnetic field of the TGU was measured after a transient time of $5\tau = 7000$ s to minimize the influence of the drift on the measure-

ment results.

The perpendicular magnetic flux density of the TGU was mapped with seven Hall sensors equidistant in the transverse direction moved in steps along the longitudinal axis at applied currents of up to 30 A. There was nothing for it but to perform the mapping for only 32 TGU periods rather than the total number of 40 , due to the mechanical limitation of the measurement system. Moreover, the flux density could not be completely mapped along the longitudinal axes at the current of 50 A owing to the unstable TGU temperature. The observed temperature rise in this case would likely have lead to a quench.

The TGU has a cylindrical pole shape for transverse flux density gradients much higher than those at the tilted rectangular one. The relative transverse gradient in a plane perpendicular to the beam axis was estimated to be 163.92 m^{-1} at the applied current of 30 A. The field gradient was nearly constant, which means a large acceptance for a linearly spectrally dispersed electron beam and in turn a large energy acceptance of the TGU.

For a better performance of the measurement system, the heat transfer from warm to cold sections needs to be minimized for the realization of temperatures around 4.5 K at an operation current of 750 A. A mechanical refurbishment is also required to measure the fields for the complete 40 periods.

3) Evaluation of the TGU Radiation

Seven 3-D field distributions with magnetic field amplitudes ranged from 0.469 T to 1.166 T were constructed by scaling the measured TGU fields to the nominal operating current. They were applied to evaluate the radiation from electrons with different energies using the WAVE simulation code. A superimposed dipole field was discovered, which affects the electron trajectories in the TGU.

After subtraction of the spurious dipole field, an optimization of the initial position of the electrons was performed to minimize the bending of the electron trajectories. And this also aimed to satisfy the condition for constructive interference leading to the features of undulator radiation. More investigations on the dipole fields and their correction methods are required to achieve straight electron trajectories in reality. And those are required for the TGU to perform as a radiation source as expected from the model calculations.

The simulation results showed that narrow-bandwidth radiation with a relative spectral width and a central energy of around 0.04 and 8.26 eV, respectively, was emitted from the TGU at electron energies ranged from 100 MeV to 122 MeV.

To our knowledge, the magnetic field measurements and the evaluation of the undulator radiation using the measured fields is the first time for a cylindrical superconducting TGU. I hope that the achievements in this thesis could contribute to the realization of LWFA-based FELs with compactness and cost efficiency.

Bibliography

[1] M. Scheer. "WAVE - A Computer Code for the Tracking of Electrons through Magnetic Field and the Calculation of Spontaneous Synchrotron Radiation". In: *Proceedings of the ICAP2012*. Rostock-Warnemünde, Germany, 2012, pp. 86–88.

[2] P. H. Bucksbaum and N. Berrah. "Brighter and faster: The promise and challenge of the x-ray free-electron laser". In: *Physics Today* 68 (July 2015), pp. 26–31. DOI: 10.1063/PT.3.2845. URL: https://doi.org/10.1063/PT.3.2845.

[3] D. H. Bilderback, P. Elleaume, and E. Weckert. "Review of third and next generation Synchrotron Light Sources". In: *Journal of Physics B: Atomic, Molecular and Optical Physics* 38.9 (Apr. 2005), S773–S797. DOI: 10.1088/0953-4075/38/9/022.

[4] M. Fuchs et al. "Laser-driven soft-X-ray undulator source". In: *Nature Phys* 5 (Sept. 2009), pp. 826–829. DOI: 10.1038/nphys1404. URL: https://doi.org/10.1038/nphys1404.

[5] W. Wuensch. "High-gradient Breakdown in Normal-conducting RF Cavities". In: *Proceedings of the 8th European Particle Accelerator Conference*. Paris, France, 2002, pp. 134–138.

[6] R.L. Geng et al. "World Record Accelerating Gradient Achieved in a Superconducting Niobium RF Cavity". In: *Proceedings of 2005 Particle Accelerator Conference*. Knoxville, Tennessee, 2005, pp. 653–655.

[7] D. Broemmelsiek et al. "Record High-gradient SRF Beam Acceleration at Fermilab". In: *New Journal of Physics* 20 (Oct. 2018), p. 113018.

[8] M. Yabashi, H. Tanaka, and T. Ishikawa. "Overview of the SACLA facility". In: *J Synchrotron Radiat* 22 (2015), pp. 477–484. DOI: 10.1107/S1600577515004658. URL: http://dx.doi.org/10.1107/S1600577515004658.

[9] T. Tajima and J. M. Dawson. "Laser Electron Accelerator". In: *Phys. Rev. Lett.* 43 (4 July 1979), pp. 267–270. DOI: 10.1103/PhysRevLett.43.267. URL: https://link.aps.org/doi/10.1103/PhysRevLett.43.267.

[10] W. P. Leemans et al. "GeV electron beams from a centimetre-scale accelerator". In: *Nature Phys* 2 (2006), pp. 696–699. DOI: 10.1038/nphys418. URL: https://doi.org/10.1038/nphys418.

[11] W. Wang et al. "Free-electron lasing at 27 nanometres based on a laser wakefield accelerator". In: *Nature* 595 (July 2021), pp. 516–520. DOI: 10.1038/s41586-021-03678-x. URL: https://doi.org/10.1038/s41586-021-03678-x.

[12] V. A. Rodríguez. "Electromagnetic Design, Implementation and Test of a Superconducting Undulator with a Transverse Gradient Field Amplitude". PhD thesis. 2015, pp. 93–101.

[13] H.-P. Schlenvoigt et al. "A compact synchrotron radiation source driven by a laser-plasma wakefield accelerator". In: *Nature Phys* 4 (Feb. 2008), pp. 130–133. DOI: 10.1038/nphys1404. URL: https://doi.org/10.1038/nphys1404.

[14] G. Fuchert et al. "A novel undulator concept for electron beams with a large energy spread". In: *Nuclear Instruments and Methods in Physics Research Section A: Accelerators, Spectrometers, Detectors and Associated Equipment* 672 (2012), pp. 33–37. ISSN: 0168-9002. DOI: https://doi.org/10.1016/j.nima.2011.12.097.

[15] H. Wiedemann. "Particle Accelerator Physics". In: Springer International Publishing Switzerland, 2015. Chap. Theory of Synchrotron Radiation, pp. 857–864. ISBN: 978-3-319-18317-6.

[16] D. J. Griffiths. "Introduction to Electrodynamics". In: Prentice Hall, Inc., 2018. Chap. Conservation Laws, pp. 346–348. ISBN: 978-1108420419.

[17] P. Schmüser et al. "Free-Electron Lasers in the Ultraviolet and X-Ray Regime". In: Springer International Publishing Switzerland, 2014. Chap. Undulator Radiation, pp. 11–23. ISBN: 978-3-319-04080-6.

[18] G. Margaritondo. "Elements of Synchrotron Light". In: Oxford University Press Inc., 2002. Chap. A real synchrotron source, p. 19. ISBN: 0-19-850931-6.

[19] D. J. Griffiths. "Introduction to Electrodynamics". In: Prentice Hall, Inc., 2018. Chap. Radiation, p. 462. ISBN: 978-1108420419.

[20] H. Wiedemann. "Particle Accelerator Physics". In: Springer International Publishing Switzerland, 2015. Chap. Undulator Radiation, pp. 899–927. ISBN: 978-3-319-18317-6.

[21] G. Margaritondo. "Elements of Synchrotron Light". In: Oxford University Press Inc., 2002. Chap. Controlling the source parameter, pp. 25–26. ISBN: 0-19-850931-6.

[22] P. Schmüser et al. "Free-Electron Lasers in the Ultraviolet and X-Ray Regime". In: Springer International Publishing Switzerland, 2014. Chap. X-Ray Free-Electron Lasers: Technical Realization and Experimental Results, pp. 165–167. ISBN: 978-3-319-04080-6.

[23] Y. V. Shvyd'ko et al. "High-reflectivity high-resolution X-ray crystal optics with diamonds". In: *Nature Phys* 6 (Mar. 2010), pp. 196–199. DOI: 10.1038/NPHYS1506.

[24] R. Bonifacioa, N. Piovellaa, and G.R.M. Robbb. "Quantum theory of SASE FEL". In: *Nucl. Instrum. Meth. A* 543 (2005), pp. 645–652. DOI: 10.1016/j.nima.2005.01.324.

[25] S. V. Milton et al. "Exponential Gain and Saturation of a Self-Amplified Spontaneous Emission Free-Electron Laser". In: *Science* 292 (5524 May 2001), pp. 2037–2041. DOI: 10.1126/science.1059955.

[26] P. Schmüser et al. "Free-Electron Lasers in the Ultraviolet and X-Ray Regime". In: Springer International Publishing Switzerland, 2014. Chap. Low-Gain FEL Theory, pp. 25–38. ISBN: 978-3-319-04080-6.

[27] H. Wiedemann. "Particle Accelerator Physics". In: Springer International Publishing Switzerland, 2015. Chap. Free Electron Lasers, pp. 929–947. ISBN: 978-3-319-18317-6.

[28] G. Margaritondo. “Elements of Synchrotron Light”. In: Oxford University Press Inc., 2002. Chap. Free electron lasers (FELs), pp. 227–249. ISBN: 0-19-850931-6.

[29] P. Schmüser et al. “Free-Electron Lasers in the Ultraviolet and X-Ray Regime”. In: Springer International Publishing Switzerland, 2014. Chap. One-Dimensional Theory of the High-Gain FEL, pp. 39–61. ISBN: 978-3-319-04080-6.

[30] J. M. J. Madey. “Relationship between mean radiated energy, mean squared radiated energy and spontaneous power spectrum in a power series expansion of the equations of motion in a free-electron laser”. In: *Nuov Cim B* 50 (1979), pp. 64–88. DOI: 10.1007/BF02737622. URL: https://doi.org/10.1007/BF02737622.

[31] Z. Huang, Y. Ding, and C. B. Schroeder. “Compact X-ray Free-Electron Laser from a Laser-Plasma Accelerator Using a Transverse-Gradient Undulator”. In: *Phys. Rev. Lett* 109 (Nov. 2012), p. 204801. DOI: 10.1103/PhysRevLett.109.204801.

[32] K.-H. Mess, P. Schmüser, and S. Wolff. *Superconducting Accelerator Magnets*. World Scientific Publishing Co. Pte. Ltd., 1996, p. 8. ISBN: 981-02-2790-6.

[33] V. A. Rodríguez et al. “Development of a Superconducting Transverse-Gradient Undulator for Laser-Wakefield Accelerator”. In: *IEEE Transactions on Applied Superconductivity* 23 (2017), p. 4101505. DOI: 10.1109/TASC.2013.2240151. URL: http://10.1109/TASC.2013.2240151.

[34] Lake Shore Cryotronic. *Phosphor bronze wire*. 2022. URL: https://www.lakeshore.com/products/categories/specification/temperature-products/cryogenic-accessories/cryogenic-wire.

[35] Lake Shore Cryotronic. *DT-670 Silicon Diodes Sensor*. URL: https://www.lakeshore.com/products/categories/overview/temperature-products/cryogenic-temperature-sensors/dt-670-silicon-diodes.

[36] Lake Shore Cryotronic. *Platinum Sensor*. URL: https://www.lakeshore.com/products/categories/overview/temperature-products/cryogenic-temperature-sensors/platinum.

[37] V. A. Rodriguez et al. “Construction and First Magnetic Field Test of a Superconducting Transversal Gradient Undulator for the Laser Wakefield Accelerator in Jena.” In: *5th International Particle Accelerator Conference*. July 2014, WEPRO036. DOI: 10.18429/JACoW-IPAC2014-WEPRO036.

[38] K.-H. Mess, P.Schmüser, and S. Wolff. *Superconducting Accelerator Magnets*. World Scientific Publishing Co. Pte. Ltd., 1996, pp. 2–3. ISBN: 981-02-2790-6.

[39] K. Damminsek et al. “Operational Experience and Characterization of a Superconducting Transverse Gradient Undulator for Compact Laser Wakefield Accelerator-Driven FEL”. In: *Proceedings of the 12th International Particle Accelerator Conference*. Campinas, Brazil, 2021, pp. 4009–4012.

[40] *Density of liquid nitrogen*. URL: https://www.aqua-calc.com/page/density-table/substance/liquid-blank-nitrogen.

[41] *Liquids - Latent Heat of Evaporation*. URL: https://www.engineeringtoolbox.com/fluids-evaporation-latent-heat-d_147.html.

[42] A. W. Chao and M. Tigner. "Handbook of Accelerator Physics and Engineering". In: World Scientific Publishing Co. Pte. Ltd., 2002. Chap. Thermodynamic and Hydrodynamic Properties of Coolant and Cryogens, pp. 338–339. ISBN: 981-02-3858-4.

[43] P. Deb, G. Biswas, and N. K. Mitra. "Heat transfer and flow structure in laminar and turbulent flows in a rectangular channel with longitudinal vortices". In: *International Journal of Heat and Mass Transfer* 38.13 (Sept. 1995), pp. 2427–2444. DOI: 10.1016/0017-9310(94)00357-2. URL: https://doi.org/10.1016/0017-9310(94)00357-2.

[44] R. B. Scott. *Cryogenic Engineering*. D. Van Nostrand Company, 1959. ISBN: 978-0442074715.

[45] M. N. Wilson. "Superconducting Magnets". In: Oxford University Press Inc., 2002. Chap. Quenching and Protection, p. 200. ISBN: 0-19-854810-9.

[46] A. W. Chao and M. Tigner. "Handbook of Accelerator Physics and Engineering". In: World Scientific Publishing Co. Pte. Ltd., 2002. Chap. Confinement and Focusing, pp. 492–493. ISBN: 981-02-3858-4.

[47] M. N. Wilson. "Superconducting Magnets". In: Oxford University Press Inc., 2002. Chap. Magnetic Force and Stresses, p. 61. ISBN: 0-19-854810-9.

[48] R.S. Popovic. *Hall Effect Devices*. CRC Press, 2003. ISBN: 9781420034226.

[49] S. Sanfilippo. "Hall probes: physics and application to magnetometry". In: (2010). Comments: 40 pages, presented at the CERN Accelerator School CAS 2009: Specialised Course on Magnets, Bruges, 16-25 June 2009. DOI: 10.5170/CERN-2010-004.423. arXiv: 1103.1271. URL: http://cds.cern.ch/record/1334470.

[50] K. Damminsek et al. "Magnetic Characterization of a Superconducting Transverse Gradient Undulator for Compact Laser Wakefield Accelerator-Driven FELs". In: *Proceedings of the 13rd International Particle Accelerator Conference*. Bangkok, Thailand, 2022, pp. 1772–1775.

[51] *AREPOC s.r.o. high linearity Hall probes for room and cryogenic temperatures*. AREPOC s.r.o. 2008.

[52] Precision Ceramics. *MACOR - A unique machinable glass ceramic, engineered to perfection*. 2021. URL: https://www.precision-ceramics.co.uk/wp-content/uploads/2021/06/Macor-Machinable-Glass-Ceramic-9-06-2021.pdf.

[53] Lake Shore Cryotronic. *Varnish Specifications*. 2022. URL: https://www.lakeshore.com/products/categories/specification/temperature-products/cryogenic-accessories/varnish.

[54] KEITHLEY. *Model 7700 Multiplexer Module*. 2018. URL: https://download.tek.com/manual/077144300_7700_Apr_2018.pdf.

[55] KEITHLEY. *2700, 2701, 2750 Multimeter Data Acquisition*. 2015. URL: https://download.tek.com/datasheet/Series2700DAQSystemDataSheet.pdf.

[56] Neutrium. *Thermal Conductivity of Metals and Alloys*. 2020. URL: https://neutrium.net/heat-transfer/thermal-conductivity-of-metals-and-alloys/.

[57] Wilhelm Herm. Müller GmbH. *Material data sheet PEEK natural*. 2019. URL: https://whm.net/wp-content/uploads/2021/04/peek-natural.pdf.

[58] A. Bernhard et al. "Radiation emitted by transverse-gradient undulators". In: *Phys. Rev. Accel. Beams* 19.13 (9 Sept. 2016), p. 090704. DOI: 10.1103/PhysRevAccelBeams.19.090704. URL: https://link.aps.org/doi/10.1103/PhysRevAccelBeams.19.090704.

[59] A. Will. "Design eines kryogenen Messaufbaus und dreidimensionale Magnetfeldmessung eines zylindrischen Undulatormodells". Bachelor Thesis. Karlsruhe Institute of Technology, 2013.

[60] M. Scheer. *WAVE by Examples*. 4.00/06. Helmholtz-Zentrum Berlin. June 2020.

A. Appendix

A.1. Evaluation of the TGU radiation

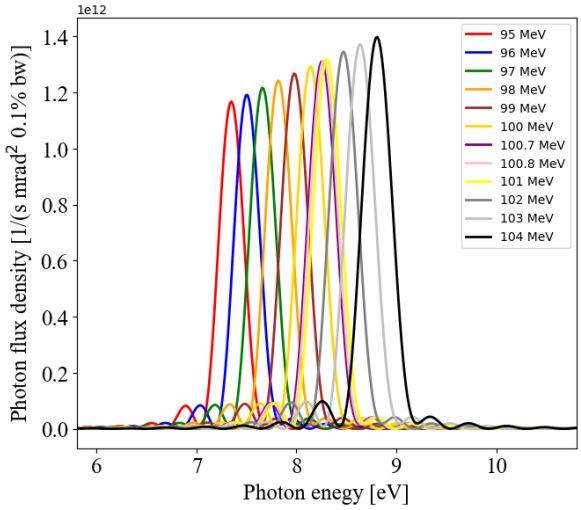


Figure A.1.: Photon flux density vs. photon energy at the field amplitude of 0.497 T.

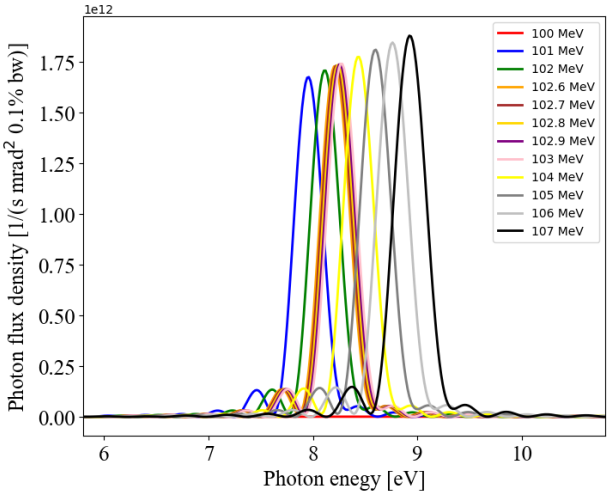


Figure A.2.: Photon flux density vs. photon energy at the field amplitude of 0.596 T.

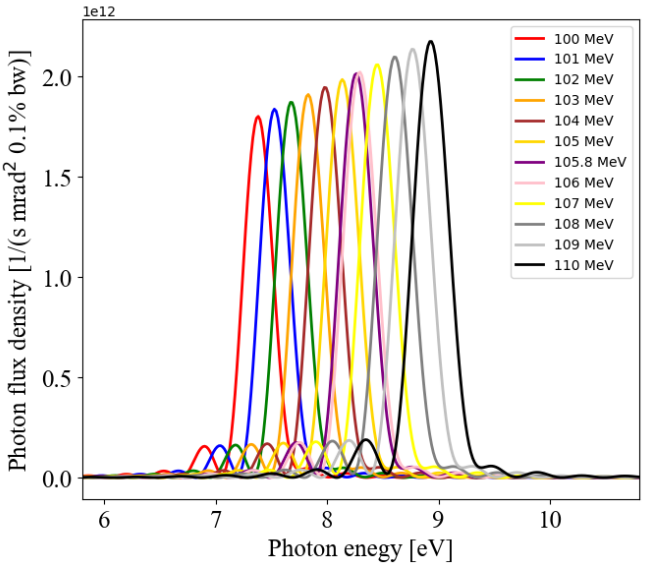


Figure A.3.: Photon flux density vs. photon energy at the field amplitude of 0.708 T.

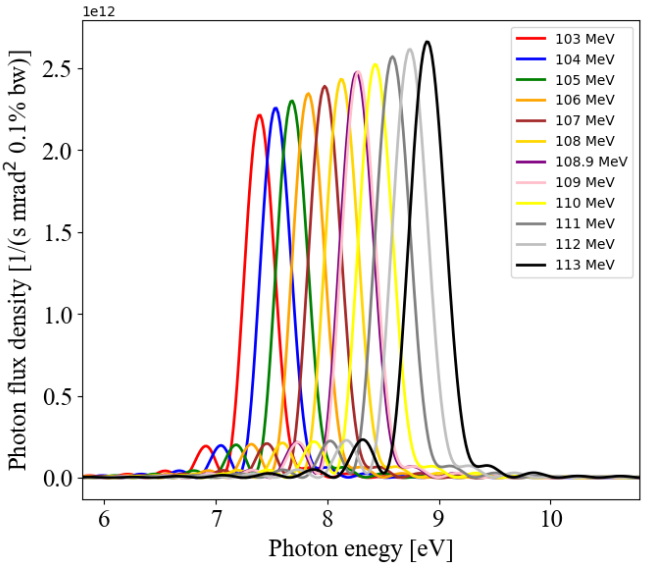


Figure A.4.: Photon flux density vs. photon energy at the field amplitude of 0.823 T.

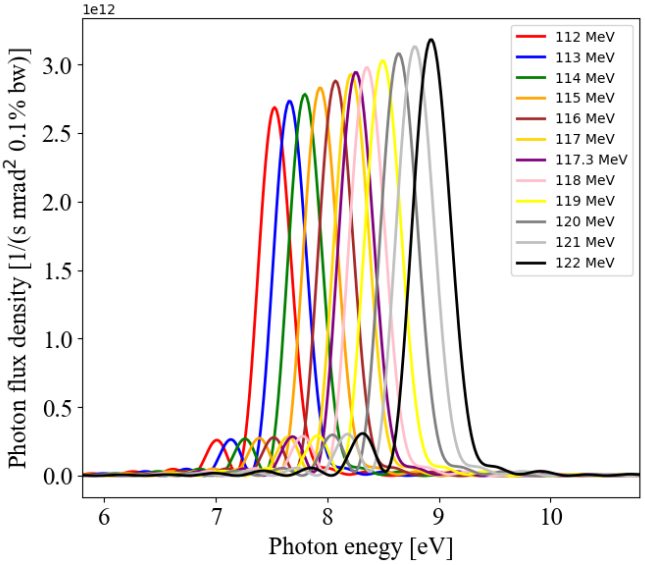


Figure A.5.: Photon flux density vs. photon energy at the field amplitude of 1.085 T.

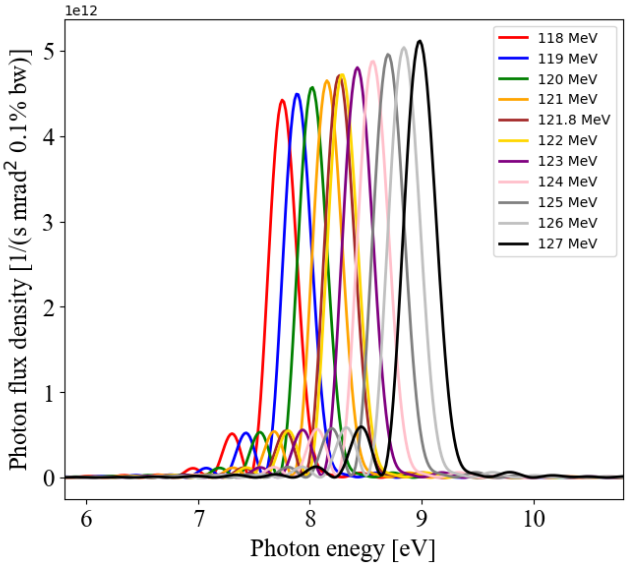


Figure A.6.: Photon flux density vs. photon energy at the field amplitude of 1.218 T.